An observational study of central engines in Active Galactic Nuclei

Rhaana Leigh Catherine Starling

Mullard Space Science Laboratory
Department of Space and Climate Physics
University College London

February 2004

A thesis submitted to the University of London
for the degree of Doctor of Philosophy

for Liz

Abstract

This thesis studies the central engines of Active Galactic Nuclei. I investigate the role of accretion discs in AGN by analysis of their multiwavelength observational properties, both in individual sources and in a sample of objects. Particular attention is paid to the interpretation of the big blue bump as thermal emission from an accretion disc. The X-ray properties of contrasting individual galaxies are studied from spectral and temporal data obtained with the *XMM-Newton* satellite. Observational constraints on accretion disc viscosity values are obtained for a subset of the Palomar Green quasar sample. Limits on the viscosity parameter, α, assuming a standard Shakura-Sunyaev viscosity prescription, are derived for the sample using the variability in their optical lightcurves. The role of an accretion disc in an unusual Seyfert 1 galaxy, RE J2248-511, is investigated taking a multiwavelength approach. I combine X-ray data from *XMM-Newton* with optical and ultraviolet spectrophotometry and infrared photometry to obtain the spectral energy distribution of an AGN which exhibits both broad optical emission lines (FWHM $\sim$ 3000 km s^{-1}) and a soft X-ray excess. I model the observed big blue bump as emission from an accretion disc to explore the physics of a disc within this system and determine the corresponding black hole mass. The results are discussed within the context of normal and narrow-line Seyfert 1 galaxies. *XMM-Newton* data is also used to gain a deeper insight into the X-ray properties of the Seyfert 1 galaxy with LINER (low-ionisation nuclear emission-line region) characteristics, NGC 7213. The broad-band spectral energy distribution of this source gives an insight into accretion in the central regions of LINER galaxies.

Contents

List of Figures

List of Tables

Chapter 1

Introduction

In this thesis I investigate the properties of Active Galactic Nuclei through multi-wavelength observations. Active Galactic Nuclei (AGN) are the nuclei of galaxies harbouring a supermassive black hole. The very first optical spectrum of an AGN was taken back in 1908 by E. A. Fath, when he observed NGC 1068 at Lick Observatory and noted the presence of strong emission lines. However, the study of AGN began in the 1940's, when Carl Seyfert observed a sample of galaxies with 'star-like' nuclear cores. These galaxies are now known as the Seyfert galaxies. The most powerful active galaxies were discovered with radio telescopes in the 1960's and named 'Quasi-Stellar Objects' or 'Quasi-Stellar Sources'; later shortened to QSO's or quasars. Their huge luminosities ($\sim 10^{42-46}$ erg s^{-1}) could not be attributed to starlight alone, and the rapid variability observed (from months down to days) implied that the radiation was emitted from very small volumes with characteristic linear size of order light days. At the time, it was proving difficult to reconcile these two properties. As more detailed observations were performed it became clear that AGN are most likely powered by accretion of matter onto a supermassive ($> 1 \times 10^5\,\mathrm{M}_\odot$) compact object. The central compact object is 'dark' - no surface having been detected, and the masses implied are much greater than the maximum for a white dwarf or neutron star, therefore the compact object is assumed to be a black hole. The central regions of an AGN are likely not static but very dynamic.

Matter orbiting the black hole has specific angular momentum. This matter will naturally form a disc to redistribute the angular momentum such that a substantial part of the matter may fall into the compact object, while the remainder carries the excess angular momentum outward. This disc is termed an accretion disc. Accretion can be an extremely efficient way of converting gravitational energy into thermal kinetic energy and radiation. Accreting systems are common and can be found everywhere in the present and in the early epochs of the Universe. Matter in an accretion disc can have very high temperatures and velocities, and the radiative power of accretion discs in AGN is enormous, making them fascinating laboratories for the study of the behaviour of matter in extreme conditions.

1.1 The physics of accretion discs

The infall of matter converts its gravitational energy to bulk kinetic energy. Viscous dissipation in the accretion disc facilitates the conversion of the bulk kinetic energy of the matter into random kinetic energy, i.e. heat. As a consequence the accreting matter is heated up, giving rise to radiation. For a central mass M with radius R, the Newtonian gravitational potential energy $E_{\rm acc}$ released by the accretion of a mass m is

$$E_{\rm acc} = \frac{GMm}{R}, \tag{1.1}$$

where G is the gravitational constant. The more compact the central object, the greater the efficiency of the accretion process.

The disc flow can be assumed to be concentrated in the orbital plane, and disc material moves in circular orbits at the Keplerian angular velocity, $\Omega_{\rm K}$,

$$\Omega_{\rm K} = \sqrt{\frac{GM}{R^3}}, \tag{1.2}$$

where M is the black hole mass, R is the radius of the orbit and G is the gravitational constant. This is the thin disc approximation, in which the radial disc size is much larger than the disc height. This approximation is still widely used, decades after

its introduction by Shakura & Sunyaev (1973, hereafter SS73), though it is by no means the only model. The thin disc is described by a set of steady disc equations. AGN accretion discs have radially decreasing temperatures from the inside out, emitting in the X-ray band at small radii, through ultraviolet (UV) to optical at large radii. The size of the disc is not well known. However, the last stable orbit outside the event horizon of a non-rotating black hole occurs at 3 Schwarzschild radii ($3R_{\rm s} = 6GM/c^2$), which is usually assumed to correspond to the inner radius of the accretion disc. In a Kerr geometry the black hole is rotating and the last stable orbit is closer to the event horizon.

The main uncertainty in modelling the accretion disc is in the viscosity. This is the mechanism that governs the transfer of angular momentum outwards allowing matter to be accreted onto the compact object. Viscosity must act within the disc, but it is not known what causes it: turbulence of the gas or magnetic fields are the most likely candidates. SS73 used a parametrisation of the viscosity, combining all the unknowns into a single variable named α, where α is the proportionality constant relating viscosity to the total local pressure. Other prescriptions exist in which the viscosity is related only to the local gas pressure. Spectrally, the viscosity is difficult to probe since the spectrum of an AGN is not strongly dependent upon the magnitude nor the origin of disc viscosity. However, the time dependence of flow of matter through the disc is controlled by α, so variations in the lightcurves, which are often large in AGN, can provide us with information on the viscosity. I will describe this further in Chapter 2.

The accretion process is important not only in AGN, but also in close binaries. In stellar mass black hole binary systems, where the black hole accretes matter from the companion star, the disc is hotter and extends down much closer to the black hole. The timescales observed in these Galactic black hole binaries can be extremely short, down to a fraction of a second, making it easier to study their accretion processes. It is not known whether the well studied accretion process in stellar mass black hole binaries can be applied to AGN with simple scaling according

to black hole mass, since the longer timescales and large distances of AGN have led to slower progress in our understanding of them.

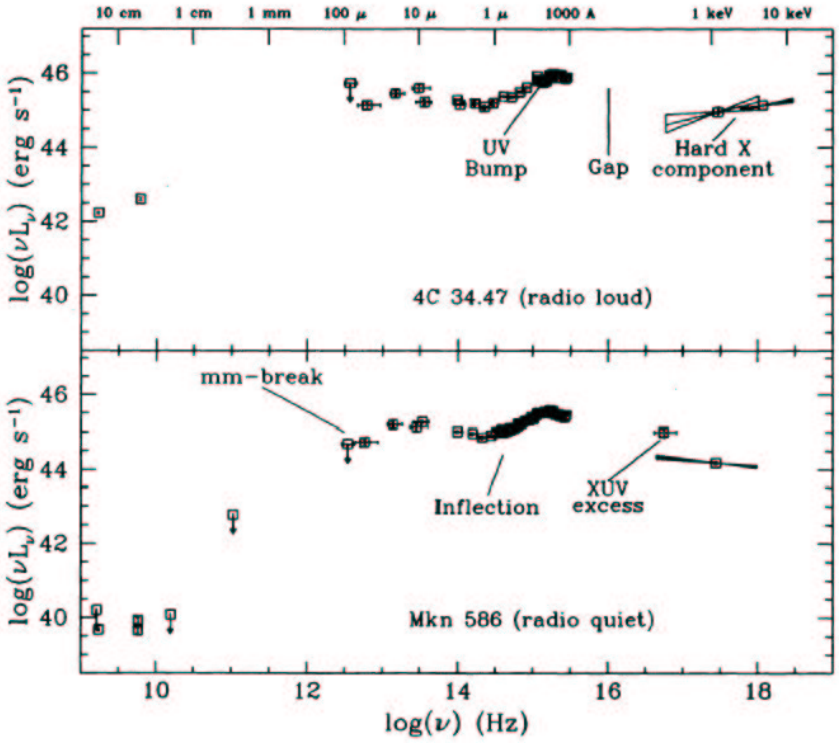

Figure 1.1: Radio to X-ray spectral energy distribution of typical radio-loud (upper) and radio-quiet (lower) AGN (Elvis et al., 1994).

1.2 Observational properties of AGN

Various types of AGN exist, but there are many properties which are shared by all or most AGN. In this section I will summarise the observational characteristics of AGN in general and the various methods by which AGN are observed, concentrating on those which are utilised in this thesis.

1.2.1 Spectra

The energy output of an AGN spans a huge wavelength range, covering much of the electromagnetic spectrum. The power output in the continuum is best examined in a plot of the spectral energy distribution (SED); this is a plot of frequency multiplied by flux (νF_ν) against frequency (ν). A typical AGN SED peaks in the infrared (the 'IR bump') and the optical/UV (the 'UV bump'), though it should be remembered that SEDs can vary substantially from one AGN to another. The UV bump displays a blackbody-like spectral shape thought to be thermal emission from an accretion disc, while the IR bump is generally attributed to thermal emission from dust. The relative strengths of these two energy peaks varies between AGN types. At higher energies (X-ray) the continuum takes the general form of a power law with a typical power law slope of photon index $\Gamma = 1.7$ (Mushotzky, 1984). In more than half of all AGN a soft X-ray excess - an excess of flux above the power law - is present (Turner & Pounds, 1989; Mushotzky, Done & Pounds, 1993). The exact shape and origin of this excess emission is currently unknown, and I will look at this feature in depth in Chapter 3 for the case of one particular AGN. The radio power appears to clearly divide AGN into two groups: radio loud (RL) and radio quiet (RQ). A typical spectral energy distribution for both a RL and a RQ AGN is shown in Fig. 1.1. Most of the AGN examined in this work are radio quiet, and their radio properties will not be discussed at all here.

Besides the continuum spectrum, a multitude of emission and absorption features are present in most wavebands. Identifications of the first AGN were made using their optical emission-line spectra, which differ significantly from the typical absorption spectrum (absorption due to stars) of a 'normal' galaxy (Fig. 1.2). The high velocities indicated by the broad optical emission lines also distinguish AGN from their non-active neighbours. The optical emission line velocity measurement is one of the most often used methods for determining the black hole mass of an AGN and I will use this technique in Chapter 3 alongside spectral modelling of the SED,

for the Seyfert 1 galaxy RE J2248-511. In the soft X-ray regime emitting and absorbing plasmas are observed in Seyfert galaxies, e.g. IRAS 13349 (Sako et al., 2000), NGC 1068 (Kinkhabwala et al., 2002) and NGC 3783 (Kaspi et al., 2002). These systems are often only resolved with the high resolution spectrographs on-board the latest X-ray observatories *XMM-Newton* and *Chandra*. Many of these outflowing 'warm absorbers' have complex multiple velocity components. The details of warm absorbers and emitters can give an insight into the structure and workings of the central engine but will not be discussed further in this work.

1.2.2 Variability

One property which led to the discovery of AGN are the rapid changes in observed luminosity. These clearly distinguish active galaxies from normal galaxies. Variability has been detected in every waveband for AGN (though not all AGN vary in all wavebands) in both continuum and line features, and variability is neither periodic nor predictable. Since AGN are multiwavelength emitters, correlating temporal flux changes in different wavebands can reveal the sizes, locations and interactions of the various emitting regions and their dependence on each other.

The relatively new technique of reverberation mapping of the inner regions of AGN appears to be a reliable method for estimating black hole mass (Peterson & Wandel, 2000). By measuring the time delay between the continuum fluctuations and the emission line response, we can measure the light-travel time from the black hole to the region of clouds known as the broad-line region (BLR) where the broad optical emission lines are produced. This gives the size of the BLR and the black hole mass. The drawback of this method is that it requires systematic long-term monitoring, which has only been carried out for a small number of objects to date.

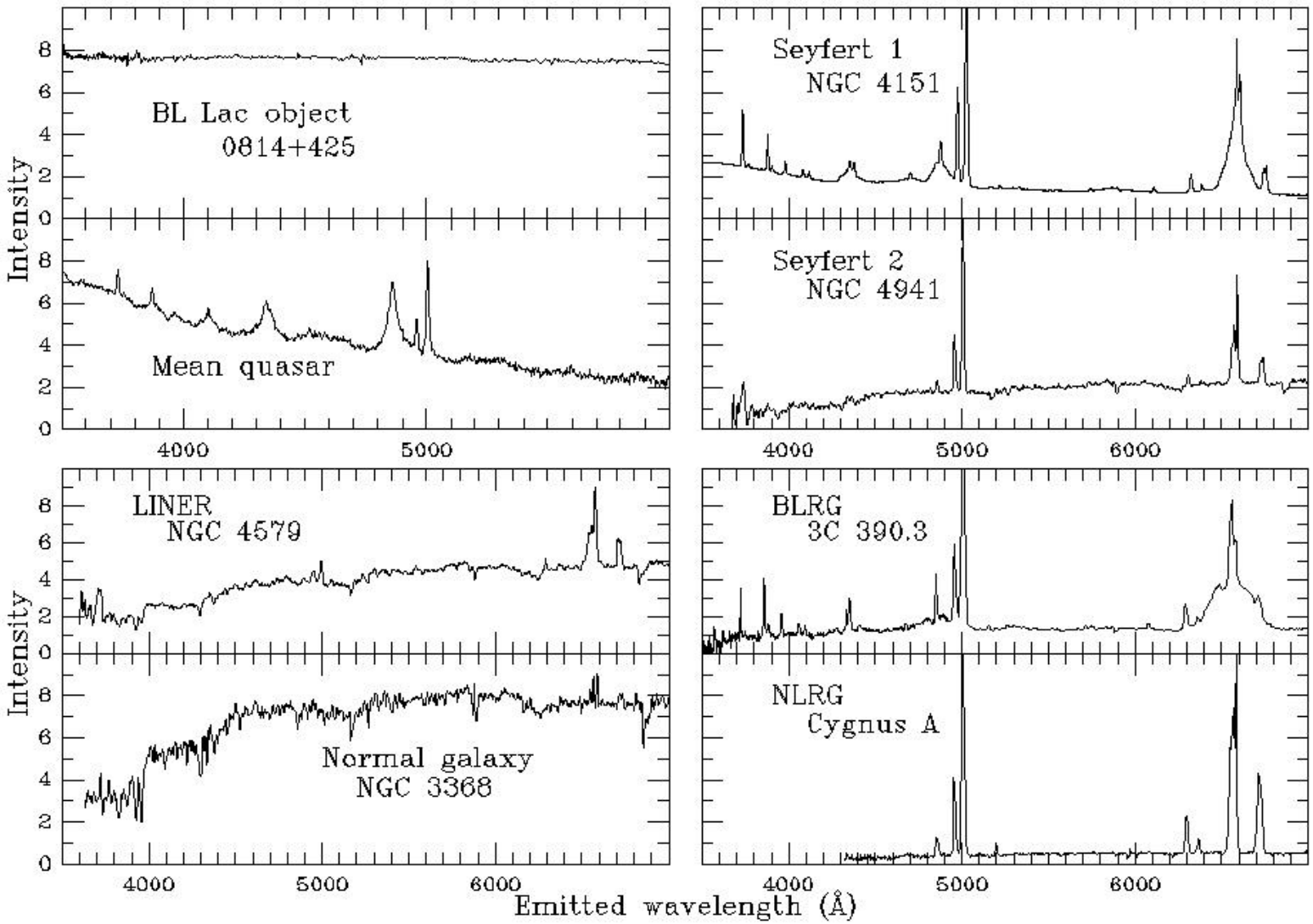

Figure 1.2: Comparison of the typical optical spectra of different classes of AGN. BLRG and NLRG's are broad and narrow-line radio galaxies respectively. Taken from the website of B. Keel, University of Alabama: `ww.astr.ua.edu/keel/agn/`.

1.2.3 Imaging

Although not the subject of this thesis, imaging across the electromagnetic spectrum is used to study various aspects of AGN. Imaging has revealed powerful jets in radio, optical and X-ray observations for some AGN (e.g. M87, Biretta, Stern & Harris, 1991), emanating from the central black hole and aligned along its rotation axis. Jets are clearly strongly dependent on the black hole properties, and as such are an important area of study.

Polarisation studies are another method of probing an AGN that deserves to be mentioned here. Polarisation studies are potentially able to look into the centres of type 2 AGN (see Section 1.3 for explanation of AGN types) where obscuration by dust limits the view at optical wavelengths. However, the low levels of polarisation in AGN have proven difficult to detect. The flux from some radio-loud AGN (blazars) is polarised by up to a few per cent, but typical polarisation levels are only 1% in the majority of AGN.

1.3 Types of AGN

The classification of AGN has been and remains a difficult task. That AGN are powered by accretion onto an extremely compact object is no longer disputed. A general structure for the nucleus as depicted in Figs. 1.3 and 1.4 is also widely accepted. However, the great variety of characteristics observed among AGN coupled with often large observed ranges of a given property mean that a single model has not yet unified AGN. Nor can they be clearly divided since boundaries between AGN classes are at best fuzzy. However, several categories of AGN have been identified and a brief description of each now follows. The current picture of the general structure of active nuclei is depicted in the artists' impressions of Figs. 1.3 and 1.4.

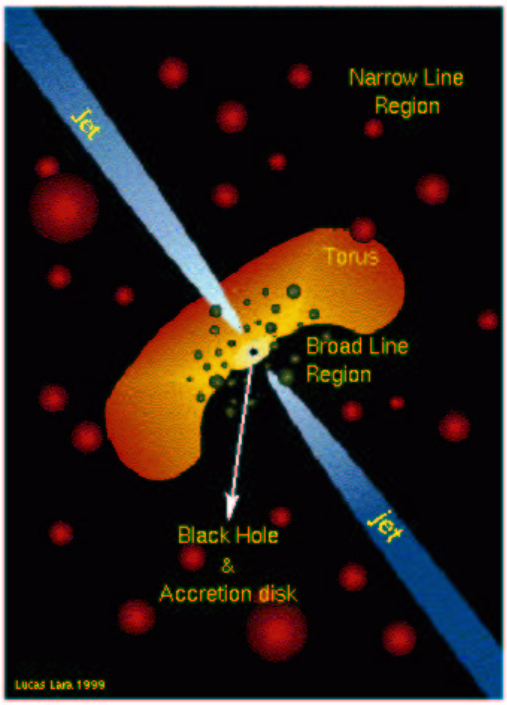

Figure 1.3: An illustration of the standard model of an AGN (Credit: L. Lara 1999).

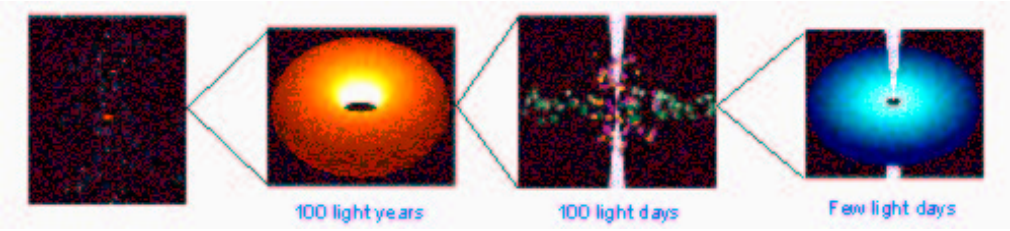

Figure 1.4: An illustration of the size scales of a typical AGN assuming the unified model structure. The NLR is shown on the far left, moving inwards to the torus (centre left), the BLR (centre right) and the accretion disc with outflowing jets (far right) (Credit: E. M. Puchnarewicz).

1.3.1 Quasars

Where the nucleus outshines its host galaxy the AGN is known as a quasar. In all other AGN types the host galaxy is more clearly visible since the nucleus is less bright. The first quasars were identified in radio surveys in the 1950's and 1960's, described as star-like objects identified with radio sources, and were not immediately associated with galaxies. The SED of a quasar is primarily a power law. Quasars can, of course, be found out to higher redshifts than lower luminosity AGN, and can therefore probe the early Universe and its subsequent evolution.

1.3.2 The Seyfert galaxies

The majority of AGN with visible host galaxies fall into the class named Seyfert galaxies. Carl Seyfert discovered these objects on photographic plates in the 1940's (Seyfert, 1943). He noticed that some spiral galaxies had 'point-like' appearances and were extraordinarily bright. The Seyferts were then subdivided into types 1 and 2, distinguished using the width of their optical emission lines; usually Hα and/or Hβ. Full width at half maxima (FWHM) greater than 1000 km s^{-1}, originating in a region known as the broad-line region (BLR), are seen in Seyfert 1's superposed on narrower lines with FWHM of a few hundred kilometres per second. Only the narrower component is observed in Seyfert 2's, and is thought to come from a region of clouds located at the outermost edge of the active nucleus which is illuminated by the central ionising source. This is known as the narrow-line region (NLR). The BLR, observed only in Seyfert 1's, must, assuming Keplerian orbits, lie closer to the black hole. A band of opaque material is thought to lie at a radius greater than that of the BLR and in the orbital plane of the nucleus. This is often referred to as the molecular torus and depicted as a doughnut shape. In unified models the torus is invoked to distinguish type 1 and 2 Seyferts (see Section 1.4).

1.3.3 Narrow-line Seyfert 1's

The narrow-line Seyfert 1 galaxies (NLS1), a subset of the Seyfert galaxies, are now seen as a class in their own right (Osterbrock & Pogge, 1985). These objects are essentially Seyfert 1's in which the optical emission lines have FWHM $\leq 2000\,\mathrm{km\,s^{-1}}$. Further characteristics of this class include an extremely strong soft X-ray excess and large temporal variability. A possible reconciliation of these characteristics is that the soft X-ray excess is the high energy tail of a hot accretion disc (Turner & Pounds, 1989; Pounds, Done & Osborne, 1995). The disc temperature is inversely proportional to the black hole mass, through the relation $T \propto (\dot{M}/M)^{0.25}$ (e.g. Laor & Netzer, 1989; Ross, Fabian & Mineshige, 1992), so soft X-ray emitting discs would require masses of order $10^6\,\mathrm{M_\odot}$. The X-ray spectrum becomes steep when this system accretes at rates close to its Eddington limit. The BLR orbits at a slower speed, either as a consequence of a lower black hole mass, or because it lies further away through formation at larger radii (Puchnarewicz et al., 1992) or because it is larger in size (Wandel, 1997; Wandel & Boller, 1998). The link between stellar mass and supermassive accreting black holes, which still eludes astronomers, is most likely to be established using NLS1's, since among AGN the NLS1's show the most resemblance to black hole binary star systems.

1.3.4 LINER galaxies

Low ionisation nuclear emission line regions are found in 20 - 33% of all galaxies (Ho, Filippenko & Sargent, 1997) and these galaxies are then known as LINERs (Heckman, 1980). A galaxy may be classified as a LINER if its optical emission line ratios show low ionisation levels; typically LINERs show strong emission from [O I] and weak [O III] and [Ne V] (all visible in the optical band). Many LINERs also contain an AGN though it is much weaker than those seen in, for example, Seyfert galaxies. The relative strength of the emission from starlight within the galaxy makes the presence of any nuclear activity often difficult to detect in LINERs. One

of the key questions to address in LINERs is whether the low ionisation emission lines are a result of shock heating following massive bursts of star formation, or of photoionisation by the active nucleus. To answer this question the AGN must be detected and deconvolved from the stellar contribution to the LINERs' luminosity. In Chapter 4 I will use X-ray observations of the LINER galaxy NGC 7213, where the AGN is clearly visible, to look at the physical parameters of accretion in LINERs, comparing them to those of luminous AGN and the Galactic Centre.

1.3.5 Blazars

The radio-loud AGN with generally featureless continua, large amplitude rapid optical variability (on the order of days or shorter) and variable, high polarisation (a few per cent) are collectively known as blazars (e.g. Miller, 1989; Bregman, 1990). The most dramatically variable (specifically in the optical band) blazars are the optically violent variables (OVVs, Penston & Cannon, 1970), while those blazars classified by the lack of strong emission or absorption in their spectra are known as BL Lacs (Strittmatter et al., 1972). The BL Lacs are named after the first of their kind to be discovered, BL Lacertae - initially misclassified as a variable star. Blazars probably have a strong relativistically beamed component (a jet-like structure) in our line-of-sight, and thus appear to be radio-loud.

1.4 Unified models

Unified models are a reasonably successful attempt to explain the different properties of type 1 (broad-line) and 2 (narrow-line) AGN with a single nuclear structure (Figs. 1.3 and 1.4, fully reviewed in Antonucci, 1993). In these models the orientation of the AGN as viewed by us determines which parts of the AGN are observed and which are obscured. The dominant source of obscuration is the molecular torus; a doughnut shaped ring of optically thick gas and dust located outside the broad line region in the orbital plane. Seyfert 1 galaxies are those viewed approximately face-on,

while Seyfert 2's are edge-on so their innermost regions are hidden behind the torus. Some unification schemes, known as 'strong' models, include all AGN by making a distinction between radio-loud and radio-quiet objects, i.e. the current classification of AGN is based upon both orientation and luminosity. In this scheme the blazars can be thought of as face-on radio galaxies where we are looking straight down the radio jet. That the current classification of most AGN is purely an orientation effect as viewed from our position is largely accepted. The exact structure of the nucleus remains, however, an area in need of further study.

1.4.1 Multiwavelength observations

A multiwavelength approach to the study of AGN is imperative. Surveys of AGN in the IR, for example, give a complementary picture of the AGN population to X-ray surveys since the radiation is dominated by entirely different processes. Reprocessing of the ionising continuum at different locations in the AGN produces different signatures. Radio observations usually show non-thermal synchrotron processes, which may originate in a jet. Dust (in the torus for example) re-radiates at IR wavelengths. The optical and UV bands are most likely dominated by continuum emission from an accretion disc and line emission from the BLR and/or NLR in all AGN other than the blazars. The X-ray band is particularly interesting, and will be described in the next section since much of this thesis is devoted to understanding this emission in AGN.

1.4.2 The importance of X-ray observations of AGN

The X-ray band is the best tool with which to learn about the inner accretion disc and the environment very close to the black hole. Hot gas radiating in X-rays is also found at other locations within active nuclei, for example the hot plasma which is observed in the soft X-rays ($\sim$ 0.1 - 2 keV) in many LINER galaxies. The hard X-ray ($\geq$ 2 keV) emission takes the form of a power law; its origins are still unknown

though many favour a hot corona enveloping the black hole or the accretion disc. The X-ray region was only really opened up in 1978 with the grazing incidence X-ray telescope on-board the *Einstein* satellite. Since then there have been many important discoveries. X-ray spectroscopy has revealed that the Fe Kα emission line, thought to be caused by fluorescence of neutral iron, is a common feature in AGN. This line can be used as a diagnostic for reflection off an accretion disc (e.g. George & Fabian, 1991). Several AGN have broad Fe Kα lines, which must emerge from close to the black hole event horizon. These are interpreted by some as evidence for spinning black holes (e.g. MCG–6-30-15, Wilms et al., 2001), and/or used as probes of strong gravity and relativistic astrophysics. The X-ray continuum is particularly important to study in sources such as the narrow-line Seyfert 1's and other EUV-bright AGN. The soft X-ray flux is high in these sources: if this emission is the high energy tail of an accretion disc (Pounds, Done & Osborne, 1995) then we again have a rare view of the gas immediately surrounding the black hole from X-ray observations.

All AGN emit in the X-ray band and are an important class of object with which to probe the high-energy Universe at cosmological distances. Active galaxies are also now known to make up the majority of the X-ray background radiation. Among accreting objects AGN are the most powerful known, and with around 10% of their total output emitted as X-rays, this makes X-ray observations of AGN one of the most exciting areas of astrophysics today.

1.5 XMM-Newton

The *XMM-Newton* X-ray observatory was launched in December 1999. The major advance achieved in *XMM-Newton* lies in the effective collecting area of each nest of 58 coaxial confocal mirrors (Aschenbach, Citterio & Ellwood, 1987), which is far larger than any previous mission. Fig. 1.7 compares the effective areas of *XMM-Newton* with those of the previous X-ray satellites *ROSAT*, *ASCA* and *Chan-*

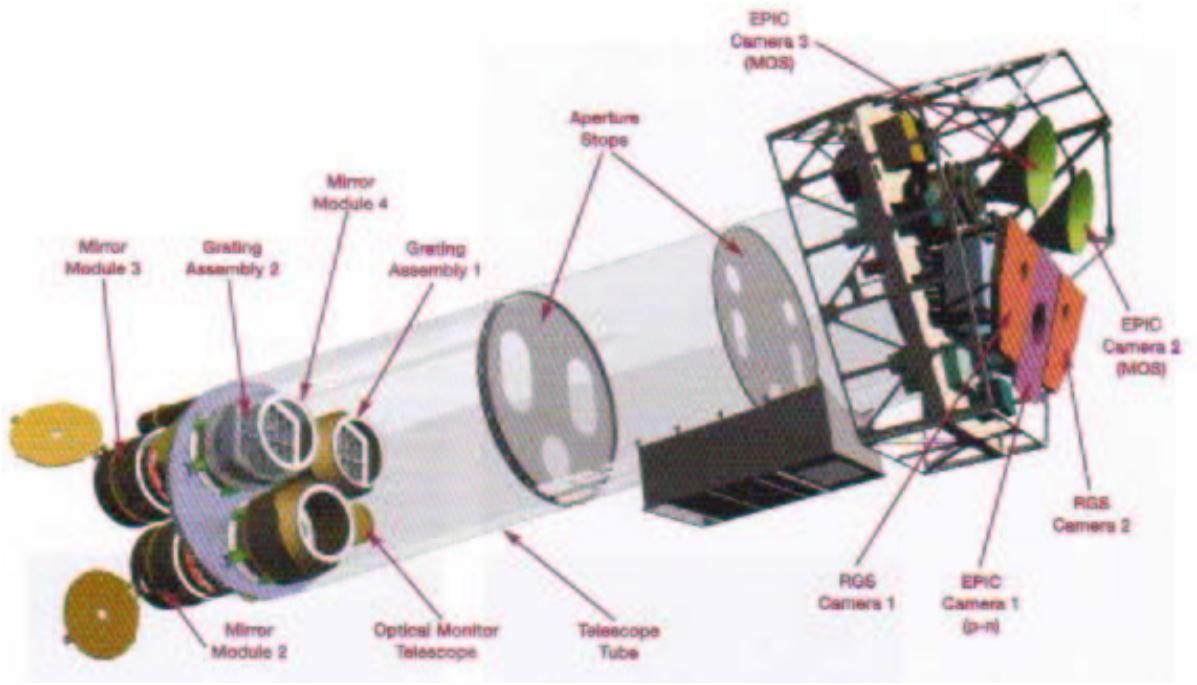

Figure 1.5: Configuration of the *XMM-Newton* satellite. Figure taken from Ehle et al. (2003), courtesy of Dornier Satellitensysteme GmbH.

dra. The second distinct advantage *XMM-Newton* has over other X-ray missions is that it provides simultaneous broad-band and high resolution X-ray spectra and optical/UV coverage. *XMM-Newton* carries three X-ray telescopes and an optical monitor (Fig. 1.5). The European Photon Imaging Camera (EPIC, Strüder et al., 2001; Turner et al., 2001) is the telescope from which most of the X-ray data have been taken for this thesis; consisting of three CCD cameras (1 pn camera and 2 MOS cameras) covering an energy range of 0.1 - 12 keV for X-ray imaging and moderate resolution spectroscopy. The second X-ray telescope is the Reflection Grating Spectrometer (RGS, Den Herder et al., 2001) comprising two spectrometers covering the energy range 0.35 - 2.5 keV (3 - 35 Å) for high resolution X-ray spectroscopy. In addition *XMM-Newton* carries the Optical Monitor (OM) telescope, with 8 filters and 2 grisms, for simultaneous multiwavelength coverage of the 1700 - 5500 Å optical-UV region. The six instruments can be operated independently and in different modes of data acquisition.

1.5.1 The European Photon Imaging Camera

The European Photon Imaging Camera on-board *XMM-Newton*, (EPIC, Strüder et al., 2001; Turner et al., 2001), consists of the pn camera and two MOS cameras at the prime focus. The EPIC cameras were built by the EPIC consortium led by Leicester University in the UK. The three EPIC cameras can perform extremely sensitive imaging observations over a field of view of 30 arcmin and an energy range $0.1 - 12.0$ keV, with moderate spectral and angular resolution ($E/\Delta E \sim 20 - 50$; FWHM ~ 6 arcsec, HEW ~ 15 arcsec). Fig. 1.6 shows the focal plane organisation of the MOS and pn cameras. The dead space between the MOS chips are unusable areas due to detector edges.

Each MOS camera comprises 7 front-illuminated Metal Oxide Semiconductor CCD chips, 600 × 600 pixels per chip. The CCDs can achieve high quantum efficiency, $\sim$ 30% for low-energy X-rays, made possible by the use of the recently

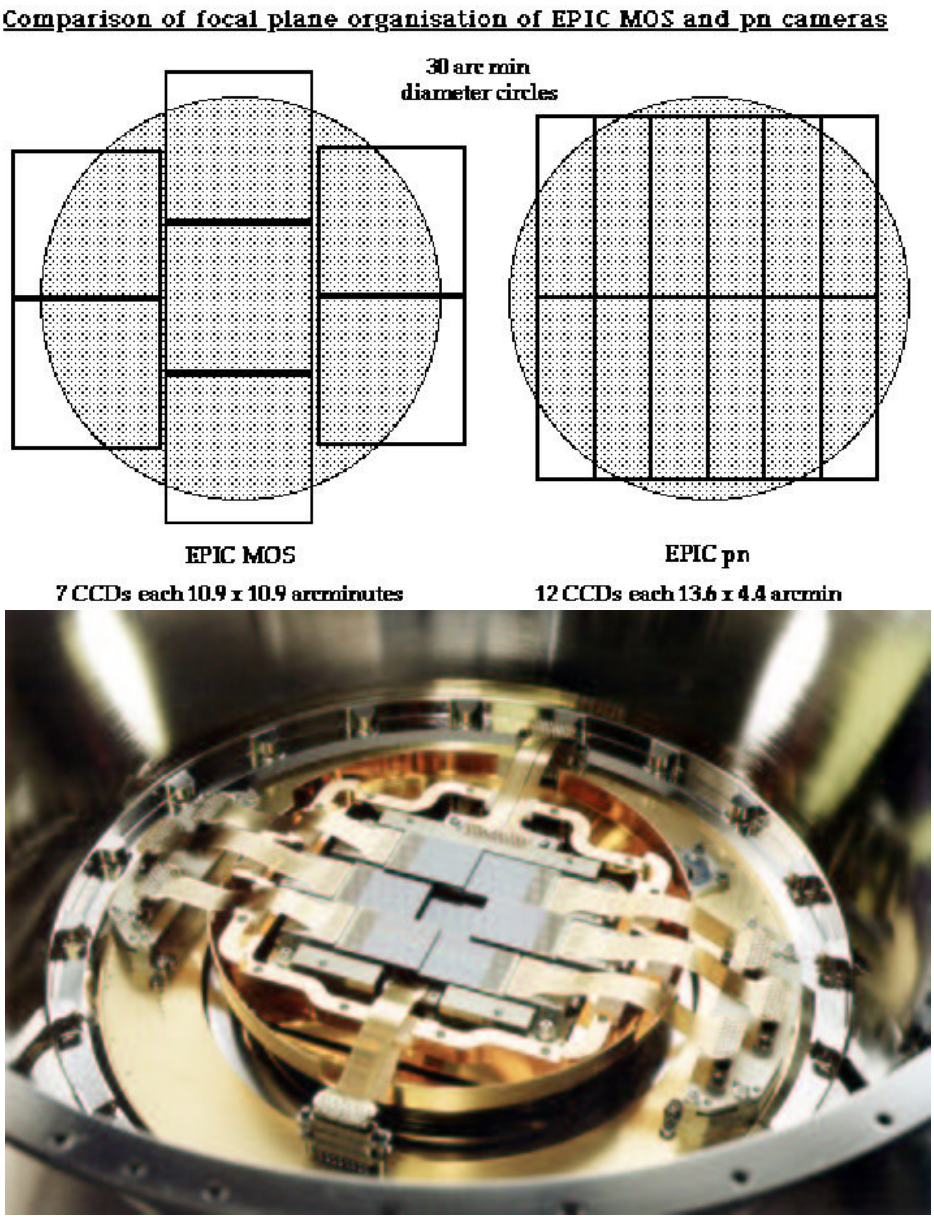

Figure 1.6: Upper image: The layout of the EPIC pn and MOS CCDs. Left: EPIC MOS comprises 7 CCDs each sized 10.9×10.9 arcmin. Right: EPIC pn has 12 CCDs of 13.6×4.4 arcmin each. The shaded circle illustrates the 30 arcmin diameter field of view. (Ehle et al., 2003).

Lower image: photo of the MOS array on its mounting (EPIC consortium).

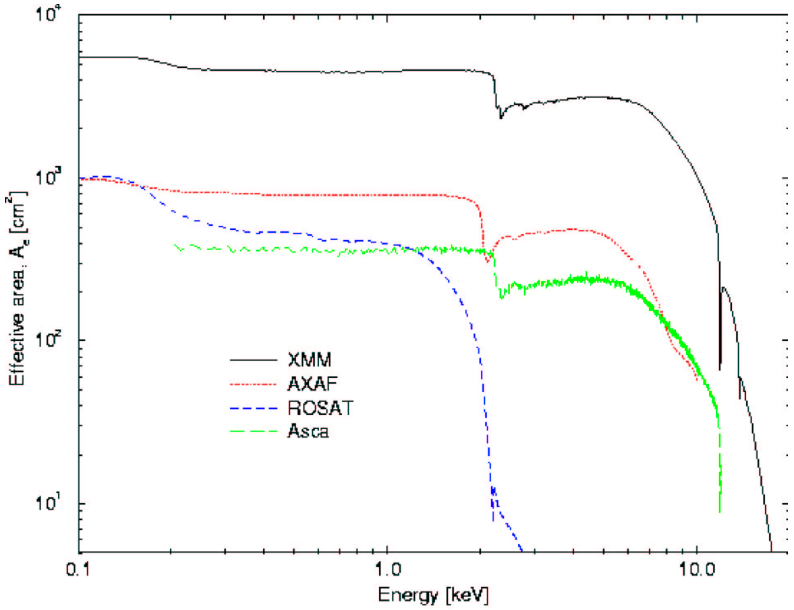

Figure 1.7: A comparison of the effective area of the *XMM-Newton* (black line), *Chandra* (formerly *AXAF*, red), *ROSAT* (blue) and *ASCA* (green) X-ray satellites. (Ehle et al., 2003).

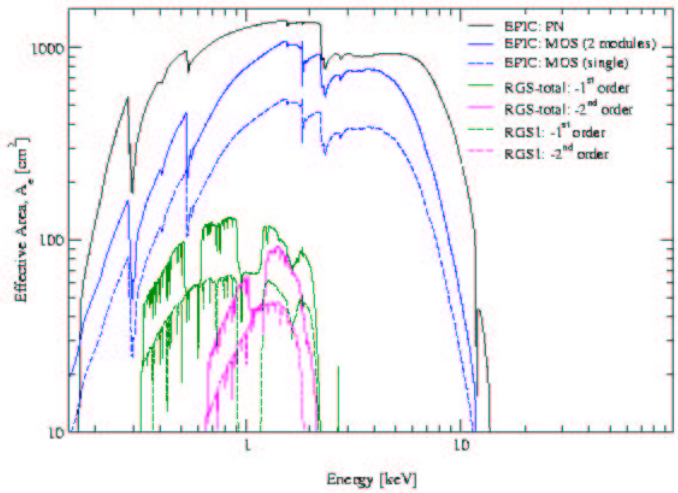

Figure 1.8: Comparison of the net on-axis effective area of the individual *XMM-Newton* X-ray instruments. (Ehle et al., 2003).

developed open-electrode structure in the cameras.

The pn camera CCDs are back-illuminated X-ray CCDs consisting of an array of 12 chips with 64×200 pixels per chip. The 12 chips are produced on a single wafer, and not assembled later as is the case for each MOS camera. The pn chip array is slightly offset with respect to the axis of its X-ray telescope so that the nominal on-axis observing position does not fall on the central chip boundary. This ensures that an on-axis point is observed on one pn chip only.

The main differences between the MOS and pn cameras are the readout time and illumination of the chips. Each pixel column in the pn camera has its own readout mode, enabling time resolution of 73.3 ms in full window mode, whereas the readout speed of a MOS CCD is 2.6 s in the same mode. The illumination of the CCDs affects the detector quantum efficiencies (QE). The QE of the MOS drops off around $5 - 6$ keV, where the back-illuminated pn detects photons with high efficiency up to 12 keV. Fig. 1.8 shows that the pn has the greater effective area of the two types of camera.

1.5.2 XMM-Newton data reduction: the Science Analysis System

The Science Analysis System (SAS) is the software package used to reduce and analyse *XMM-Newton* science data (Gondoin, 2000). The SAS contains reduction pipelines and a set of file manipulation tools. The pipelines produce calibrated event lists for the X-ray cameras, and flat-fielded sky images for the OM. The SAS tools allow the observer to generate appropriate instrument response matrices, and extract spectra, light curves, images and source lists from the X-ray event lists. The SAS is continually being updated and new versions are released periodically.

1.6 Aims and scope of this thesis

This thesis provides an observational study of central engines in AGN, concentrating on continuum emission at optical and X-ray wavelengths. The main aim throughout is to look at the role of accretion discs and their parameters in a wide range of AGN types. I address this by taking a multiwavelength approach and using several methods to estimate accretion disc parameters. X-ray data reveal the hot central regions close to the black hole, reflection off the accretion disc and emission from highly ionised ions. By studying optical and UV observations I can model thermal continuum emission which may arise in the disc, and determine black hole mass both from disc modelling and from the optical emission line widths. Temporal variability is also a method which I use to provide information on disc parameters. In the optical case the viscosity can be estimated for a sample of AGN and the size of the X-ray emitting region is obtained from X-ray lightcurves.

Each chapter contains an introduction to the specific topic covered and a discussion of the results. In Chapter 2 I make accretion disc viscosity estimates by comparing the temporal optical variability of a sample of AGN with accretion disc models. Chapter 3 is a study of the Seyfert 1 galaxy RE J2248-511. I investigate the *XMM-Newton* X-ray data in detail and combine this with optical and UV data to model the spectral energy distribution as an accretion disc. Chapter 4 uses *XMM-Newton* data to look at the X-ray properties of the LINER galaxy NGC 7213. To investigate accretion in this object, radio, optical and UV data are also examined and the relationship between LINER galaxies, Seyferts and the Galactic Centre is discussed. Finally, Chapter 5 brings all the individual results together to conclude, and ideas for future work are set out.

Chapter 2

Constraints on AGN accretion disc viscosity

2.1 Introduction

The transport of angular momentum remains the main problem of accretion disc theory. Shakura & Sunyaev (1973) suggested that magnetic fields and turbulent motions are likely candidates for the angular momentum transport. They argued that turbulence is a dominant factor and postulated that the stress is proportional to the local pressure. The proportionality parameter α, which is independent of the underlying transport process, describes the efficiency of the turbulent transport. The α parameterization provided a base for developing the accretion disc theory and linked the theory with the observations.

More recent work has shown that in weakly magnetized discs magnetohydrodynamic (MHD) turbulence can provide the majority of the outward transport of angular momentum (Balbus & Hawley, 1991). Balbus & Papaloizou (1999) reviewed the α-disc models and find that MHD turbulence follows the α prescription very closely. They show that the vertically averaged disc with viscosity due to magnetorotational instabilities is described by a similar set of radial equations to the α-discs. In par-

ticular the local energy dissipation rate is determined by the global disc parameters as it is in the α-discs. However, global 3-D numerical simulations of accretion discs are extremely complex (Matsumoto & Shibata, 1997) and so most work to date has been done using local 2-D shearing box, cylindrical and axisymmetric limit models. All these methods have provided predictions of the α-parameter ranging from $\sim$ 0.005 (Brandenburg et al., 1995) to $\sim$ 0.6 (Hawley, Gammie & Balbus, 1995).

In order to determine the magnitude of the viscosity better estimates from larger samples of all categories of accreting objects are needed with independent methods for estimating α. Since the spectrum of a disc at any particular instant is not strongly dependent on its viscosity the most effective way to estimate the viscosity is through the disc variability. A number of studies of this kind have been done for accreting binary systems since the timescales of variability are optimal for observation, generally ranging from days down to a fraction of a second. Viscosity estimates for these objects have found that very generally $0.001 < \alpha < 0.1$ (Menou et al., 2000; Dubus, Hameury & Lasota, 2001). For the case of GRS 1915+105, for example, Belloni et al. (1997) predict values of α of 0.004 and 0.05 for the Schwarzschild and extreme Kerr cases respectively.

In the case of AGN astronomers observe typical optical fluctuation timescales of weeks to years although there have been only a few long-term monitoring programs to provide such data (for example Pica et al., 1988; Giveon et al., 1999, hereafter G99). At optical and ultraviolet frequencies the majority of the continuum luminosity seen in AGN is held to be emission from the accretion disc (Malkan & Sargent, 1982) and large variability has been observed in these wavebands for many such objects (Webb & Malkan, 2000). The physical origin of optical flux variations has not been pinned down, but if disc emission dominates the spectrum at optical wavelengths the variability is expected to be related to the disc instabilities.

In this study I use a subset of the Palomar Green sample of AGN (G99), spanning approximately seven years of data, to derive limits on the viscosity parameter for the sample as a whole via the method described in Siemiginowska & Czerny

(1989, hereafter SC89). I assume any fluctuations in the lightcurves are due to an instability arising in the innermost disc regions and can be associated with the thermal timescale. I do not identify the exact physical process responsible for this instability. It can be related to the Lightman-Eardley instabilities in the radiation pressure dominated region of the disc (Lightman & Eardley, 1974), but this method does not require modelling of the instability and therefore could be applied to any type of instability which may be present in the inner disc. Using a set of multi-temperature blackbody disc models, based on the standard α-disc as prescribed by SS73, I calculate the contribution to the optical spectrum from the outer, stable disc and assume that there is no contribution from the innermost parts of the disc where the instability has developed. Comparing the variability timescales of the sources with the thermal timescales of the models allows the α-parameter for the sample to be constrained. The results of this chapter have appeared in Starling et al. (2004).

2.2 Data sample

The data are taken from the optically selected Palomar-Green (PG; Schmidt & Green, 1983) sample. A subset of 42 bright ($-28 < M_B < -22$) and nearby AGN ($0.06 < z < 0.37$) in the northern hemisphere were observed at the Wise Observatory, Israel (G99) in 1991 - 1998. Observations were made with a CCD camera mounted on the 1m optical telescope and span 7 years with a typical sampling interval of 39 days - a higher, more even sampling interval than that of previous programs (for example Pica et al., 1988). The wavelength range covers the Johnson B band, 3600 - 5600 Å ($\lambda_{\rm central} = 4400$ Å), which is a region of the spectrum believed to be dominated by the disc emission. The PG sample is statistically complete with good photometric accuracy over this wavelength range (~ 0.02 mag. at 4400 Å). G99 assume a Hubble constant $H_0 = 70$ kms^{-1}Mpc^{-1} and a deceleration parameter of $q_0 = 0.2$. This is a flux-limited sample so one expects to see selection effects as discussed in Schmidt & Green (1983). This sample has also been studied at a number

of other wavelengths including R band (G99), radio (Kellermann et al., 1989), IR (Neugebauer et al., 1987) and X-ray (Laor et al., 1997) and its optical polarisation properties were studied by Berriman et al. (1990). Measurements of the masses of 17 of the PG sources have been made by reverberation mapping (Kaspi et al., 2000).

From the lightcurves I derived a two-folding timescale as a characteristic timescale for each source. The two-folding (or doubling) timescale, τ_2, gives the time for an objects' luminosity to change by a factor of two (either an increase or a decrease) which can be used as a measure of variability in both the data and the models (O'Brien, Gondhalekar & Wilson, 1988 and references therein; SC89). The two-folding timescale is given by

$$\tau_2 = \tau_{\rm s} \frac{f_{\rm min}}{(f_{\rm max} - f_{\rm min})}, \tag{2.1}$$

where $f_{\rm max}$ and $f_{\rm min}$ are the maximum and minimum observed flux levels respectively, $\tau_{\rm s} = \tau_{\rm max} - \tau_{\rm min}$ is the time between maximum and minimum flux levels. The lightcurves for this data set do not show flux variations of a factor of two, in fact $\sigma_B/B \leq 34\%$, in which case τ_2 is the time over which a linearly extrapolated flux variation would increase or decrease the observed flux by a factor of two. These timescales were then corrected for the effects of cosmological time dilation.

In order to calculate $f_{\rm min}/(f_{\rm max} - f_{\rm min})$ I used the standard transformation from magnitude to flux,

$$m_{\rm min} - m_{\rm max} = -2.5 \log \left(\frac{f_{\rm min}}{f_{\rm max}} \right) \tag{2.2}$$

The luminosity is calculated using the following three equations relating apparent magnitude, flux and luminosity at 4400 Å (e.g. Weedman, 1998),

$$\log \frac{F_{\lambda,4400\,\text{Å}}}{\text{erg cm}^{-2}\ \text{s}^{-1}\ \ \text{Å}^{-1}} = -0.4(m_B + 20.42) \tag{2.3}$$

$$L_{\lambda,4400\,\text{Å}} = 4\pi d^2 (1+z)^2 F_{\lambda,4400\,\text{Å}} \tag{2.4}$$

$$d = \frac{c[q_0 z + (q_0 - 1)(\sqrt{1 + 2q_0 z} - 1)]}{q_0^2 H_0 (1+z)} \tag{2.5}$$

Here, $F_{\lambda,4400\,\text{Å}}$ and $L_{\lambda,4400\,\text{Å}}$ are the median flux and luminosity at 4400 Å, c is the speed of light in a vacuum, z is the redshift and d is the luminosity distance of the source. The apparent magnitudes, m_B, are taken from G99 and corrected for the line-of-sight extinction, with B band extinction values taken from Schlegel, Finkbeiner & Davis (1988). Here I use $H_0 = 70$ km s^{-1} Mpc^{-1} and $q_0 = 0.2$ for consistency with the G99 preparation of the lightcurves.

The corresponding errors in luminosity, disregarding the uncertainty in H_0, are typically $\pm 1.6 \times 10^{41}$ erg s^{-1} and are derived from the G99 estimate of a photometric accuracy for this band. The latest determination of the Hubble constant is 71^{+4}_{-3} km s^{-1} Mpc^{-1} (measured with *WMAP*, Spergel et al., 2003).

The K-correction to the integrated B band luminosities is approximately zero since, assuming the data behaves like the disc models presented in the following section, the slope of the emission follows a power law with energy index $\alpha \sim -1$. This can be seen in Fig. 2.1, where the models with $R_{\rm cut} < 200\ R_{\rm s}$ which contribute most to the B band luminosity (see Fig. 2.2) have approximately flat slopes.

2.2.1 Sample refinement

PG1226+023, better known as 3C 273, is the most optically luminous object in this sub-sample of the PG quasars, i.e. an order of magnitude or greater in luminosity than all the other sources. This AGN is known to have optical, X-ray and radio jets. It is the only source in the optically selected sample which shows definite jets, though 7 of the 42 objects are radio-loud. The jet emission is thought to be synchrotron radiation and variable itself. Since the disc emission cannot be separated from that of the jet, PG1226+023 will not be included in this analysis.

2.3 The model

I assume that the optical emission observed in the PG sample originates from an accretion disc. Adopting the approach of SC89, the disc may be divided into two

distinct regions: the optically thick outer region emitting blackbody contributions into the B band, and the inner region of the disc, which does not significantly contribute to the B band emission.

I assume that the optical variability is caused by an instability on the thermal timescale, which varies the position of the inner radius of the optical emission region. I assume that the two-folding timescales measured in the B band lightcurves of the PG sample correspond to the thermal timescale at the radius $R_{\rm cut}$ where the luminosity in the B band has decreased by 50% from its maximum value. The value of the radius $R_{\rm cut}$ for a given luminosity depends upon the chosen disc model, accretion rate and black hole mass.

Comparing $R_{\rm cut}$ for each model with the thermal timescale, $\tau_{\rm th}$, gives a value of α from the following equation

$$\tau_{\rm th} = \frac{1}{\alpha\omega_{\rm k}} \tag{2.6}$$

where $\omega_{\rm k} = \sqrt{\frac{GM}{R^3}}$ is the Keplerian angular velocity.

To describe the outer optical flux emitting disc I use a standard multi-temperature blackbody α-disc code developed by Czerny & Elvis (1987) and used in SC89. The model assumes a geometrically thin, optically thick Keplerian disc accreting steadily onto a Schwarzschild black hole.

I assume that the disc radiates locally as a blackbody with an emitted flux of

$$\sigma T_{\rm eff}^4 \;=\; \frac{3GM\dot{M}}{8\pi R^3}\left(1-\sqrt{\frac{R_{\rm inner}}{R}}\right) \tag{2.7}$$

where R is the radial distance from the central object, σ is the Stefan-Boltzmann constant, $T_{\rm eff}$ is the effective temperature of the disc at radius R, G is the gravitational constant, M is the black hole mass, $\dot{M}$ is the steady accretion rate and $R_{\rm inner}$ is the inner radius of the disc (e.g. Frank, King & Raine, 1992). I assume $R_{\rm inner} = 3R_{\rm s}$, where $R_{\rm s} = 2GM/c^2$ is the Schwarzschild radius. Inside the radius $R_{\rm cut}$ I do not make any further assumptions about the nature and spectral properties of the disc. I only assume that the optical flux from that region is negligible. Fig. 2.1 shows different spectra depending on the choice of

$R_{\rm cut}$. Note that the maximum contribution to the flux at a given frequency ν comes from the disc region with the temperature $kT_{\rm eff} = 1.65h\nu$, which is located at the distance $R_\nu = 0.77 \times 10^{24}\nu^{-4/3}(M/\,{\rm M}_\odot)^{-1/3}(L/L_{\rm Edd})^{1/3}R_{\rm g}$ (SC89), where $L_{\rm Edd} \sim 1.3 \times 10^{38}(M/\,{\rm M}_\odot)$ erg s^{-1} is the Eddington luminosity. Hence for a source with a black hole mass of $10^8\,{\rm M}_\odot$ emitting at the Eddington luminosity the location of the B band is $R_\nu \sim 21 - 38\ R_{\rm g}$, within the chosen range.

The shape of the spectrum depends upon

1) M, the black hole mass

2) $\dot{M}$, the accretion rate

3) the extent of the outer disc contributing to the optical flux, which depends on the variable $R_{\rm cut}$ since $R_{\rm outer}$ is fixed at $10^3\ R_{\rm s}$

4) i, the disc inclination. I assume an inclination angle of $\cos i = 0.75$ (41°) since optical spectroscopy has shown that all the sample have broad emission lines.

I also consider the effects of opacity in a modified blackbody model in which electron scattering in the disc is taken into account (Czerny & Elvis, 1987; Haardt & Maraschi, 1993). Electron scattering becomes important at high temperatures, so one would expect the effects of opacity to be visible at ultraviolet energies and above, and should not significantly modify the continuum emission at optical wavelengths. The contribution from the B band to the total disc luminosity as a function of the cut-off radius $R_{\rm cut}$ is shown in Fig. 2.2, for a broad range of black hole masses. It can be seen that for masses $> 10^8\,{\rm M}_\odot$, only values of $R_{\rm cut} < 500\ R_{\rm s}$ are realistic.

To enable comparison with the data, the luminosities of the model spectra were convolved with the B filter which had been applied during observation of the PG sample. Two-folding timescales for the models are easily obtained from the log L *vs.* $\log\tau_{\rm th}$ plots by measuring the time taken for the luminosity to drop from its maximum to half that value (Fig. 2.3). Each value of α for a set of models has a characteristic timescale (Equation 2.6). Finding sets of models which encompass the data sample allows the determination of the range of the viscosity parameter for that data set.

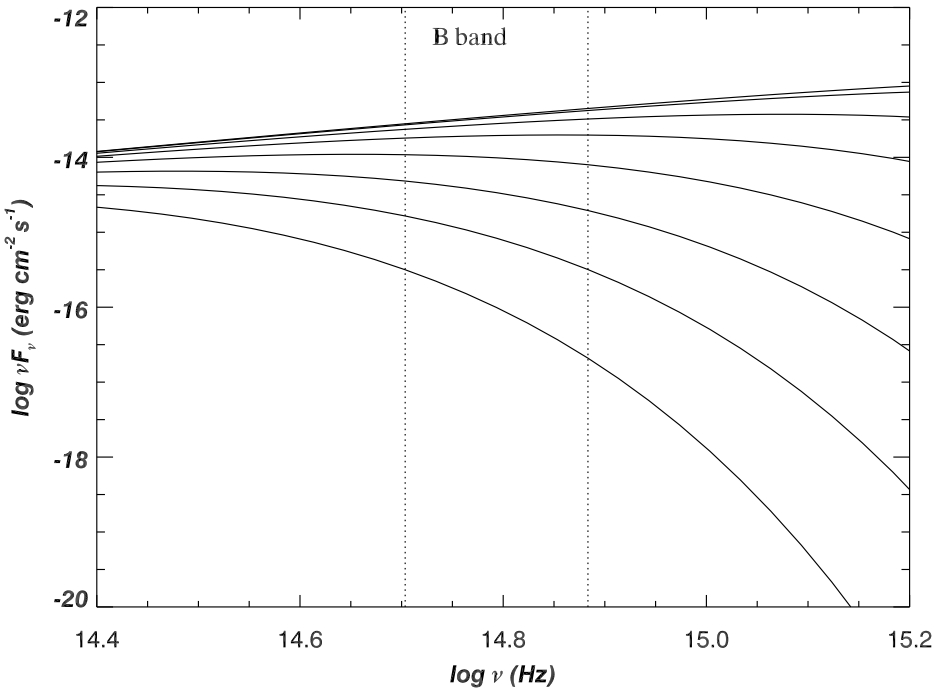

Figure 2.1: The model blackbody spectrum for a $M = 10^8\,\mathrm{M}_\odot$ black hole, accreting at one tenth of the Eddington rate, with increasing radial disc size $R_{\rm cut} = 3$ (upper curve), 10, 29, 64, 127, 218, 345, 514 (lower curve) $R_{\rm s}$. The outer disc radius is always fixed at $R_{\rm outer} = 10^3 R_{\rm s}$.

The vertical dotted lines mark the region covered by the B band in the observers' frame ($3600 - 5600\,\text{Å}$).

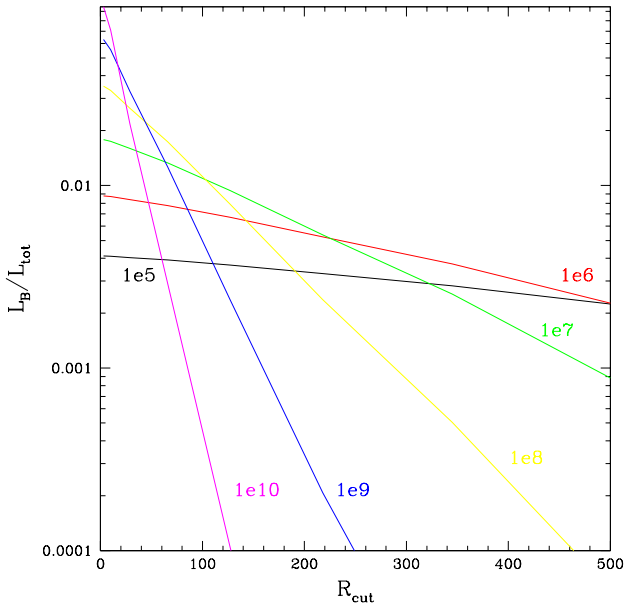

Figure 2.2: The fraction of total disc luminosity emitted in the Johnson B band with the position of the cut off radius $R_{\rm cut}$, given in units of Schwarzschild radii, for five different masses as indicated on the plot in units of $M_\odot$. Courtesy A. Siemiginowska.

2.4 Results

2.4.1 Variability

The lightcurves for this dataset show a typical intrinsic variability amplitude of $\sigma_B = 0.14$ mag with intrinsic rms amplitudes of $5\% < \sigma_B/B < 34\%$ over the seven year period (G99). The variability timescales lie approximately between 300 and 4500 days. The distribution of two-folding timescales is shown in Figs. 2.4 and 2.5 and the individual timescales and luminosities for each AGN are given in Table 2.1. However, for the reasons which I will outline in the following section the viscosity parameter cannot be accurately determined for any individual object. The mean two-folding timescale for the sample is 1566.4 days and the corresponding standard

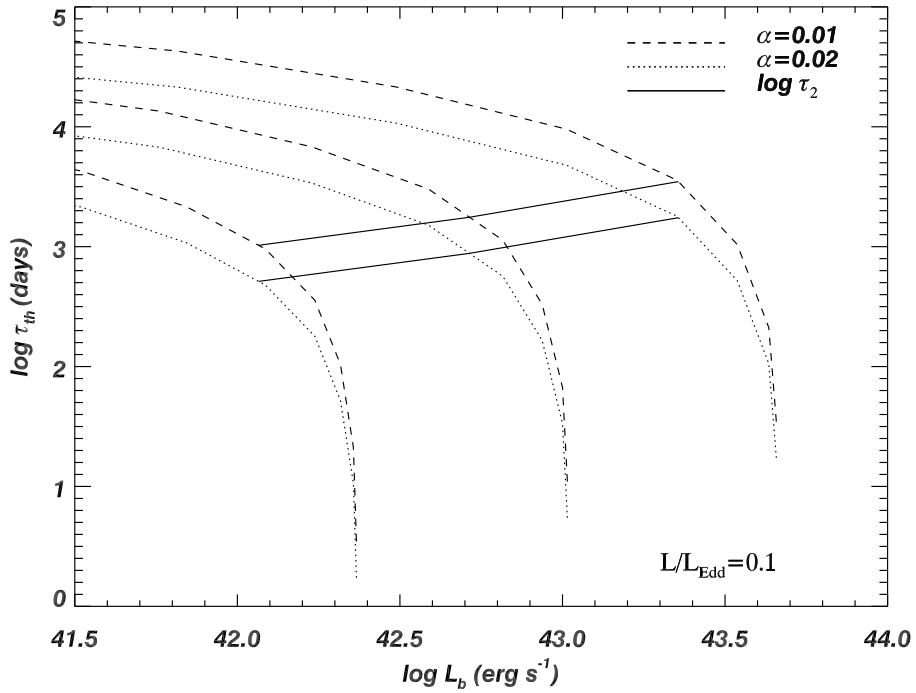

Figure 2.3: The blackbody disc models' B band luminosity *vs.* thermal timescale. This is the case of $L/L_{\rm Edd} = 0.1$ and black hole masses $10^7, 10^{7.5}$ and $10^8\,{\rm M}_\odot$, with the smallest mass producing the lowest luminosity.

For each mass the model is calculated for 8 steps in $R_{\rm cut}$ from the last stable orbit ($3R_{\rm s}$) out to $512R_{\rm s}$. This has been done for two values of the viscosity parameter; α = 0.01 (dashed lines) and $\alpha = 0.02$ (dotted lines). The solid lines join the points at which the luminosity has decreased by 50% from its maximum value in each model (τ_2).

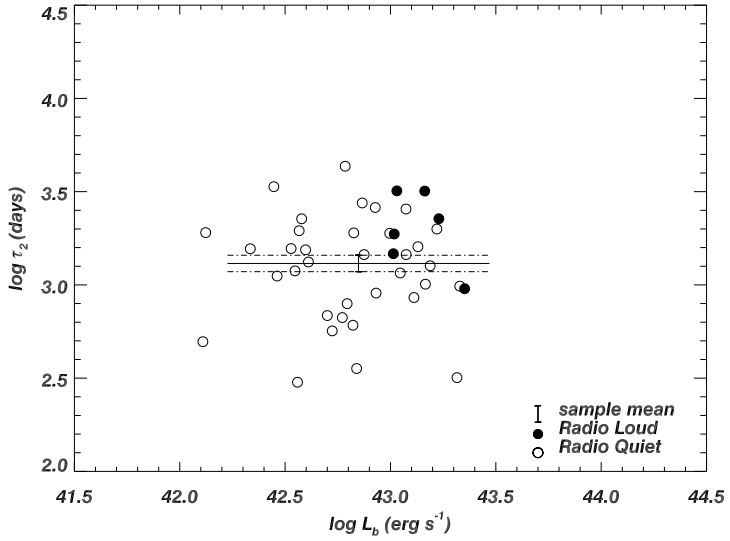

Figure 2.4: The B band two-folding timescales versus luminosity for each source (log scale). The mean and standard deviation of the mean are represented by the solid line and dot-dashed lines respectively, with the vertical error bar at the point of the mean luminosity. The uncertainty in the value of H_0 introduces uncertainties in the luminosities, so I have not calculated the error on the mean luminosity here. The length of the luminosity error bar includes 95% of the data (2σ).

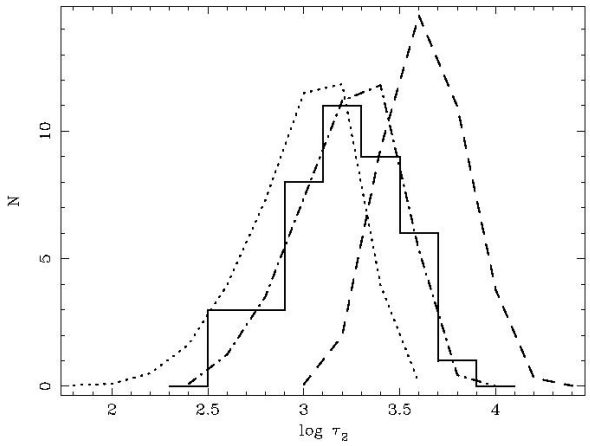

Figure 2.5: Comparison of the observed distribution of two-folding timescales for 41 PG sample AGN (binsize $\Delta \log \tau_2 = 0.2$, N counts per bin) with distributions predicted from random realisations of the broken power law power spectrum (with break frequency $\nu_{\rm bk}$) which probably describes the red-noise optical variability in AGN (10000 lightcurves simulated, N rescaled to 41 counts over whole distribution). Solid histogram: observed distribution, dotted line: $\nu_{\rm bk} = 10^{-7}$ Hz, dot-dashed line: $\nu_{\rm bk} = 2 \times 10^{-8}$ Hz, dashed line: $\nu_{\rm bk} = 4 \times 10^{-9}$ Hz. Courtesy P. Uttley.

deviation of the mean is 143.6 days (in log space, $< \log \tau_2 >= 3.115 \pm 0.044$).

2.4.2 Distribution of two-folding timescales

To establish whether or not the observed variability is accurately measured using the two-folding timescale P. Uttley has carried out the following simulations. The optical variability of AGN is consistent with a red-noise process, so that each lightcurve is a realisation of an underlying process described by a power law power spectrum with a slope and amplitude determined by the mechanism which causes the variability. In principle, it is possible to derive the power-spectral parameters from the model for variability, and compare these with observations. We consider here only the simple case of variability described by the two-folding timescale, which is a property of the power-spectral shape. Due to the stochastic nature of red-noise processes, lightcurves obtained at different times will look different, and show different observed two-folding timescales. The 'true' average two-folding timescale should be obtained when averaging the two-folding timescale over many 7-year lightcurves from the same source. As this is clearly not possible, we must take account of the fact that the two-folding timescale measured for a given source is not the same as the average two-folding timescale, and considerable scatter is introduced into the distribution of observed two-folding timescales for sources which have identical variability properties (i.e. identical power-spectral shapes).

To test whether the observed distribution of two-folding timescales is consistent with a single power-spectral shape and amplitude (and a corresponding single average two-folding timescale), the observed distribution can be compared with that determined from simulated red-noise lightcurves generated from plausible power-spectral parameters. P. Uttley has simulated random realisations of red-noise lightcurves using the method of Timmer & König (1995). To date, only the X-ray power-spectral shapes of AGN have been well constrained (Uttley, M$^{\rm c}$Hardy & Papadakis, 2002), showing steep ($1/\nu^2$) power-law slopes at high frequencies and breaking to flatter $1/\nu$

Table 2.1: Individual minimum two-folding timescales and luminosities for each PG quasar. The luminosity quoted is the median B band luminosity in the rest-frame of the source. Errors in the luminosities stem from errors in the observed magnitudes and hence the flux. Errors due to uncertainty in H_0 are not included here.

Quasar	other names	z	RL	$L_B/10^{42}$ (erg s^{-1})	τ_2 (days)
PG0026+129		0.142		11.9±0.22	1454
PG0052+251		0.155		20.7±0.38	318
PG0804+762		0.100		14.7±0.27	1009
PG0838+770		0.131		1.33±0.02	1907
PG0844+349	Ton 951	0.064		5.29±0.10	567
PG0923+201	Ton 1057	0.190		11.1±0.20	1158
PG0953+415	K 348-7	0.239		15.4±0.29	1266
PG1001+054		0.161		3.62±0.07	301
PG1012+008		0.185		16.6±0.31	1994
PG1048+342		0.167		1.29±0.02	496
PG1100+772	3C 249.1	0.313	Y	14.5±0.27	3186
PG1114+445		0.144		6.70±0.12	1901
PG1115+407		0.154		3.80±0.07	2262
PG1121+423		0.234		6.23±0.11	793
PG1151+117		0.176		6.64±0.12	608
PG1202+281	GQ Com	0.165		5.02±0.09	685
PG1211+143		0.085		13.5±0.25	1602
PG1229+204	Ton 1542	0.064		3.52±0.06	1189
PG1307+086		0.155		8.54±0.16	904
PG1309+355	Ton 1565	0.184	Y	10.4±0.19	1874
PG1322+659		0.168		6.10±0.11	4329
PG1351+640		0.087		9.92±0.18	1891
PG1354+213		0.300		3.69±0.07	1953
PG1402+261	Ton 182	0.164		8.47±0.16	2600
PG1404+226		0.098		2.16±0.04	1562
PG1411+442	PB 1732	0.089		7.35±0.14	2750
PG1415+451		0.114		2.90±0.54	1116
PG1426+015	Mkn 1383	0.086		4.08±0.07	1327
PG1427+480		0.221		3.95±0.07	1542
PG1444+407		0.267		2.80±0.05	3362
PG1512+370	4C 37.43	0.371	Y	10.7±0.20	3194
PG1519+226		0.137		3.38±0.06	1566

Table 2.1 Continued...

PG1545+210	3C 323.1	0.266	Y	10.3±0.19	1470
PG1613+658	Mkn 876	0.129		12.9±0.24	856
PG1617+175	Mkn 877	0.114		6.91±0.13	356
PG1626+554		0.133		5.91±0.11	668
PG1700+518		0.292		21.3±0.40	985
PG1704+608	3C 351	0.371	Y	22.5±0.41	954
PG2130+099	II Zw 136	0.061		7.50±0.14	1454
PG2233+134		0.325		11.8±0.22	2551
PG2251+113	PKS 2251+11	0.323	Y	17.00±0.31	2264

slopes below some break frequency. The optical power-spectral shape of the AGN in the PG sample is not well constrained, but correlated long-timescale optical/X-ray variations in the luminous Seyfert galaxy NGC 5548 suggest that although the optical power spectrum of luminous AGN is steeper than the X-ray power spectrum at high frequencies, the shapes are similar at low frequencies (Uttley et al., 2002). Therefore the model assumed here consists of a high-frequency power-spectral slope of $1/\nu^{2.5}$, breaking to $1/\nu$ below some break frequency, $\nu_{\rm bk}$, assumed to be common to both X-ray and optical power spectra. Uttley, Papadakis & M$^{\rm c}$Hardy (2002) show evidence that the power spectral breaks in X-ray power spectra of AGN may scale linearly with black hole mass. Following this result a break frequency of 2×10^{-8} Hz was chosen, corresponding to a black hole mass of a few $\times10^8$ M$_\odot$; a power-spectral normalisation which corresponds to the typical observed $\sim 10\%$ variability amplitude in the sample was adopted.

P. Uttley simulated 10000 lightcurves of 7 year duration, and measured the resulting distribution of two-folding timescale τ_2, which is plotted for comparison with the observed distribution of τ_2 in Fig. 2.5. This figure also shows the distributions corresponding to break frequencies of 10^{-7} Hz and 4×10^{-9} Hz, i.e. a possible factor ~ 25 range in black hole mass. The observed distribution of τ_2 is consistent with that expected from random realisations of a single power spectral shape expected from few $\times10^8$ M$_\odot$ black holes. So the distribution of black hole masses is likely to be narrow (< decade) and the variability in the lightcurves of all the AGN can be

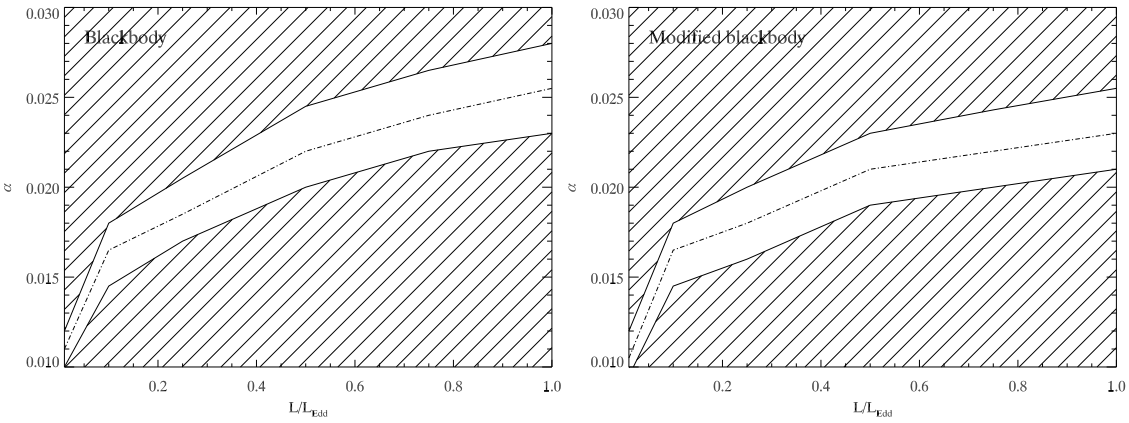

Figure 2.6: The allowed range of α values for both blackbody models (left) and modified blackbody models (right). The permitted values of α lie within the solid lines, the best fitting values lying along the dot-dashed line. The shaded areas are regions in which a given viscosity parameter, α, and Eddington ratio, $L/L_{\rm Edd}$, cannot occur simultaneously in the model.

characterised by a single identical two-folding timescale, as expected from a homogeneous sample of AGN such as that presented here. This result is not sensitive to the slope above the break. From Equation 2.6 the sample must also be consistent with a single value of the quantity $R_{\rm cut}^{3/2}/\alpha$. Keeping the Eddington ratio $L/L_{\rm Edd}$ fixed, there is a single value of the viscosity parameter α determined by the average τ_2 of the sample.

For $0.01 \leq L/L_{\rm Edd} \leq 1.0$ the data are best fitted by the set of models outlined in Table 2.2. Fig. 2.6 shows the allowed values of α over a range of the Eddington ratio for both the disc models I apply. Note that the difference in viscosity between blackbody and modified blackbody models is small over this wavelength range.

Table 2.2: Model parameters best-fitting the PG data, with corresponding mass and accretion rate ranges of $10^7 < M < 10^{8.5}$ ($M_\odot$) and $0.02 < \dot{M} < 0.70$ ($M_\odot$ year^{-1}).

Model	$L/L_{\rm Edd}$	$\alpha_{\rm min}$	$\alpha_{\rm mean}$	$\alpha_{\rm max}$
disc blackbody	0.01	0.010	0.011	0.012
disc blackbody	0.1	0.015	0.017	0.018
disc blackbody	0.25	0.017	0.019	0.021
disc blackbody	0.5	0.020	0.022	0.025
disc blackbody	0.75	0.022	0.024	0.027
disc blackbody	1.0	0.023	0.026	0.028
modified blackbody	0.01	0.010	0.011	0.012
modified blackbody	0.1	0.015	0.017	0.018
modified blackbody	0.25	0.016	0.018	0.020
modified blackbody	0.5	0.019	0.021	0.023
modified blackbody	0.75	0.020	0.022	0.024
modified blackbody	1.0	0.021	0.023	0.026

2.5 Discussion

2.5.1 Comparison with numerical simulations

Since direct observations cannot yet resolve the inner accretion disc in AGN, numerical simulations of accretion flows have existed for several decades and are moving in the direction of global 3-D models. The results fall within the range $0.005 \leq \alpha \leq 0.6$ predicted by a variety of recent numerical simulations of MHD turbulent discs. However, I obtain much tighter constraints towards the lower end of this broad range which could eliminate some models. For example, Armitage (1998) writes that $\alpha \sim 0.1$ in global and local cylindrical disc simulations with net vertical field, whereas $\alpha \sim 0.01$ when the net vertical field is zero. MHD simulations have also shown that an alternative α-prescription in which stress is proportional only to the magnetic pressure may be a better diagnostic of the viscosity mechanism, since using the SS73 α-prescription a range of α values can be obtained for the same gas pressure (Hawley & Balbus, 1995).

2.5.2 Observational estimates of α

The only previous observational viscosity estimates for AGN discs were those calculated by SC89 for 8 AGN and 4 blazars at 1060 Å , 3 AGN at 1395 Å and 12 AGN at 1740 Å , with the prediction that $\alpha_{\rm min} = 0.001$ and $\alpha_{\rm max} \sim 0.1$. These results allow a much tighter estimate of the viscosity range and I find a value around 0.01. Both estimates have used the same disc model, but at different wavelengths; I chose an optical sample rather than the UV data used by SC89 since the optical bands lie further from the peak in the power law region of the disc spectrum. SC89 assume an inclination angle of 0° and include blazars in their sample. They discuss the likelihood that the interpretation of blazar variability as thermal changes in the accretion disc may not be valid since synchrotron radiation is known to dominate in many of these objects. They also note that the sampling of 5 of their sample objects was not designed for detecting the timescales of interest when estimating disc viscosities. O'Brien et al. (1998) examined IUE data of several AGN and found that most had UV two-folding timescales of weeks to years with no shorter timescale variability. The sampling rate for this data set was poor. Consequently, it would not be possible to estimate α for their sample.

2.5.3 Variability and black hole mass

Simulations of red-noise lightcurves generated from plausible power-spectral parameters (P. Uttley) show that this sample of 41 AGN all have similar (< decade) masses and therefore can all be represented by a single two-folding timescale. This implies a very narrow range of α and/or $L/L_{\rm Edd}$. This seems to suggest that we are observing all these AGN in a single 'state'. If this is true, it may be that all observed AGN are in the outburst state and those in the quiescent state are either too faint to have yet been detected or appear as normal galaxies (Siemiginowska & Elvis, 1997; Burderi, King & Szuszkiewicz, 1998; Hatziminaoglou, Siemiginowska & Elvis, 2001). If the former is true, this would then imply that the total number of AGN in existence

is far higher than current estimates based on the number of sources seen. However, a single value of α throughout the thermal limit cycle has been predicted in some numerical simulations of MHD turbulence in AGN accretion discs (Menou & Quataert, 2001), though the thermal ionisation instability is unlikely to be a source of large amplitude variability in AGN. Reverberation mapping measurements exist for 16 of these sources (Kaspi et al., 2000) ranging from 2.16×10^7 to $4.7 \times 10^8\,\mathrm{M}_\odot$ ($M_{\mathrm{average}} = 1.51 \times 10^8\,\mathrm{M}_\odot$) with typical errors of $^{+37.8}_{-36.1}\%$. Black hole masses found through the disc modelling method are dependent upon the ratio of AGN luminosity to the Eddington limit, L/L_{Edd}. For $L/L_{\mathrm{Edd}} = 0.01$, $M = 10^8 - 10^{8.5}\,\mathrm{M}_\odot$ as suggested by comparing the observed distribution of two-folding timescales with distributions predicted from random realisations of the broken power law power spectra. The reverberation mapping results are compatible with all the Eddington ratios used here.

2.5.4 Assumptions and caveats

I will now summarise the main assumptions and note some caveats on the determination of α. The accretion disc models I use here are simple multi-temperature blackbody spectra (Czerny & Elvis, 1987), and I assume that the disc is the source of the B band luminosity. It is also assumed that long term variability in this band occurs on the thermal timescale at a radius corresponding to a 50% change in B band luminosity. The limits on α are derived only for the sample as a whole since the variability timescale and mass of each individual object is not precisely known. The results are dependent on the validity of the assumptions stated above and require a single viscosity value throughout the outer disc. In practice, viscosity is likely to be both radially and time dependent and variations in luminosity may occur on various timescales and radii. For example, the α value derived here would be a lower limit on the true value if the observed variability timescales are not equal to but are longer than the thermal timescale.

Blackbody, modified blackbody and modified blackbody plus Comptonization models gave very similar (and, in the case of the latter two, the same) values of α. The small difference between the blackbody models and the addition of opacity effects to these models shows that in the optical B band, away from the peak of the emitted flux, electron scattering has only a small effect on the spectrum as expected. The models are sensitive to the value of H_0 in the calculation of the luminosities of the data points; $L \propto 1/H_0^2$. Here I use $H_0 = 70$ km s^{-1} Mpc^{-1} for consistency with the G99 preparation of the lightcurves. The latest *WMAP* determination of H_0 is uncertain by $\sim 5\%$.

The disc models do not include warps, clumpiness or flares. Contributions to the variability from occurrences of flares is likely to be on timescales shorter even than the sampling interval of the lightcurves. G99 estimate pollution by the host galaxies to be approximately 5% based on observations with HST (Bahcall et al., 1997). The emission line contribution to the optical flux is estimated in the same paper at 5 - 10%. The models applied here are for AGN continuum flux only and I have not reduced the observed flux to account for these since a 10% luminosity increase will not greatly affect the viscosity estimates. These models do not incorporate a corona, transition region, self-gravitation or irradiation of the disc material. Coronae are thought to be the source of hard X-rays but could alter the shape of the optical spectrum as we may see reprocessing and/or scattering, and this may be important in some AGN. The role of the corona in forming the continuum emission is discussed in Kurpiewski, Kuraszkiewicz & Czerny (1997) and a corona could be incorporated in future determinations of the α-parameter.

There are currently no conclusive observational or theoretical bounds on the α parameter. I have carried out this study in the hope of taking another step towards determining the nature of viscosity in AGN.

2.6 Conclusions

I assume that optical variability of AGN observed on timescales of months to years is caused by local instabilities occurring on the thermal timescale in the inner accretion disc. The disc is modelled using multi-temperature blackbody models. In this case I constrain the viscosity to

$$0.01 < \alpha < 0.03 \text{ for } 0.01 \leq L/L_{\rm Edd} \leq 1.0.$$

Lightcurve simulations carried out by P. Uttley show this sample is consistent with a single α value at a given Eddington ratio, determined by the average characteristic timescale of all 41 AGN. The range of α values found lies within the range predicted by current numerical simulations of MHD turbulent discs. The mass range I obtain for this sample is consistent with the reverberation mapping measurements made for 16 of these PG quasars. However, I stress that this is a simplified model of an accretion disc, and merely a first step in observational viscosity estimates for AGN.

Chapter 3

RE J2248-511: an ultrasoft broad-line AGN

RE J2248-511 is a radio-quiet EUV-selected AGN discovered by the *ROSAT* Wide Field Camera (Pounds et al., 1993), and classified as a Seyfert 1 galaxy from optical follow-up observations revealing broad emission lines with FWHM $\sim$ 2900 km s^{-1} (Mason et al., 1995). It lies at a redshift of $z = 0.101$, and is a bright source with $L_{\rm X} = 3 \times 10^{44}$ erg s^{-1} and $m_V = 15.0$. It is termed an 'ultrasoft' Seyfert galaxy owing to the large excess of flux at very soft X-ray energies (< 0.25 keV) above a power law fit to the *ROSAT* PSPC observation (Puchnarewicz et al., 1995, hereafter P95). The spectrum was best fit with a broken power law with steep spectral slopes ($\Gamma_{0.1-0.25\ \rm keV} = 4.13$, $\Gamma_{0.25-2\ \rm keV} = 2.62$; P95). Steep soft X-ray slopes are a characteristic of narrow-line Seyfert 1 (NLS1) galaxies, which have BLR velocities ≤ 2000 km s^{-1}. The soft X-ray spectrum of RE J2248-511 resembles those typical of NLS1's, but this AGN has high velocity broad-line clouds. Studies of *ROSAT* PSPC slopes in AGN have concluded that sources with both steep soft X-ray continuum slopes and broad optical emission lines (Hβ FWHM $\geq$ 3000 km s^{-1}) are simply not found in nature (Boller, Brandt & Fink, 1996; Wandel & Boller, 1998; Grupe et al., 1999). The combination of steep soft X-ray slope and low velocity broad-line

region found in NLS1's has been explained by invoking a low mass black hole and a high accretion rate (e.g. Pounds, Done & Osborne, 1995, hereafter PDO95). The steep soft X-ray slope is then interpreted as the high energy tail of an accretion disc. Alternatively the BLR may be large in size (Wandel, 1997; Wandel & Boller, 1998), may form at a relatively large distance from the central black hole or is viewed approximately face-on (Puchnarewicz et al., 1992).

P95 considered the possibility that the observed EUV to soft X-ray brightness of RE J2248-511 was due to a 'hole' in the Galactic column in that direction. This was prompted by power law fits to the PSPC spectrum which inferred columns equal to or lower than the Galactic value for that direction. Extreme ultraviolet emission from AGN is usually difficult to observe because these wavelengths are heavily absorbed by gas in our own galaxy and also from within the AGN itself, which makes EUV-bright AGN unusual. P95 measured the local 100 μm IR cirrus using data from the *IRAS* satellite and compared this to the Galactic N_H value in the Stark et al. (1987) maps ($N_H = 1.4 \times 10^{20}$ cm^{-2}). These two columns were in agreement, therefore the ultrasoft X-ray excess is a genuine feature. An ultrasoft excess has also been observed in the broad-line Seyfert galaxies 1H 0419-577 ($\Gamma_{0.1-0.5keV} = 3.9^{+3.4}_{-3.9}$, Guainazzi et al., 1998) and RX J0437.4-4711 (Wang et al., 1998).

RE J2248-511 was then observed with *ASCA* in 1997 by Breeveld, Puchnarewicz & Otani (2001, hereafter BPO2001), who found that the soft X-ray output of this AGN is variable. The *ASCA* observations showed that the soft excess had completely disappeared and the entire 0.5 - 10 keV spectrum could be represented by a single absorbed power law. At optical wavelengths three spectra taken in 1991 (Mason et al., 1995; P95) showed no variability over a 3 month period, whilst a spectrum taken in 1992 (Grupe et al., 1999) is inconsistent with the 1991 results. Large amplitude variability in the soft X-ray excess has also been observed in the similar Seyfert 1 galaxies 1H 0419-577 with *ROSAT*, *ASCA*, *Beppo-SAX* and *XMM-Newton* (Guainazzi et al., 1998; Turner et al., 1999; Page et al., 2001; Pounds et al., 2004) and RX J0437.4-4711 with *ROSAT* and *ASCA* (Halpern & Marshall, 1996; Wang

et al., 1998). AGN with ultrasoft X-ray spectra have been compared to the high-soft state of Galactic black hole binary systems, first noted for the NLS1 galaxy RE 1034+39 (PDO95). Variability of the ultrasoft X-ray component is observed as the Galactic black hole binary system makes a transition from one state to another. The three EUV-bright AGN, RE J2248-511, 1H 0419-577 and RX J0437.4-4711, appear to form a sub-category all of their own characterised by both a variable ultrasoft X-ray excess and broad optical emission lines, the co-existence of which cannot readily be explained by the standard unified models described in Chapter 1.

This chapter describes the results of a multiwavelength monitoring campaign of RE J2248-511, consisting of X-ray observations from the *XMM-Newton* satellite with supporting optical and IR observations made at the South African Astronomical Observatory and archival multiwavelength data. I will use these data to examine the relationship between the X-ray and optical emitting components, specifically the interpretation of the big blue bump (BBB) as thermal emission from an accretion disc, and evaluation of the long-term spectral variability. I will also compare the properties of RE J2248-511 with those of 'normal' and narrow-line Seyfert 1 galaxies. A preliminary analysis of the *XMM-Newton* data is given in Starling et al. (2002).

3.1 XMM-Newton observations

RE J2248-511 was observed by the EPIC (Strüder et al., 2001, Turner et al., 2001) and RGS (Den Herder et al., 2001) instruments on-board *XMM-Newton* (Jansen et al., 2001) on 26 October 2000, 21 April 2001 and 31 October 2001. The Optical Monitor was switched off during these observations because a nearby bright star saturates the field. All EPIC instruments were in small window mode with the medium filter applied, excepting the MOS cameras during the October 2000 observation which were then in small window free running mode. Since small window free running mode is not yet fully calibrated, I consider only data from the pn, which has, in fact, the higher net count rate of the EPIC instruments (Fig. 1.8). During

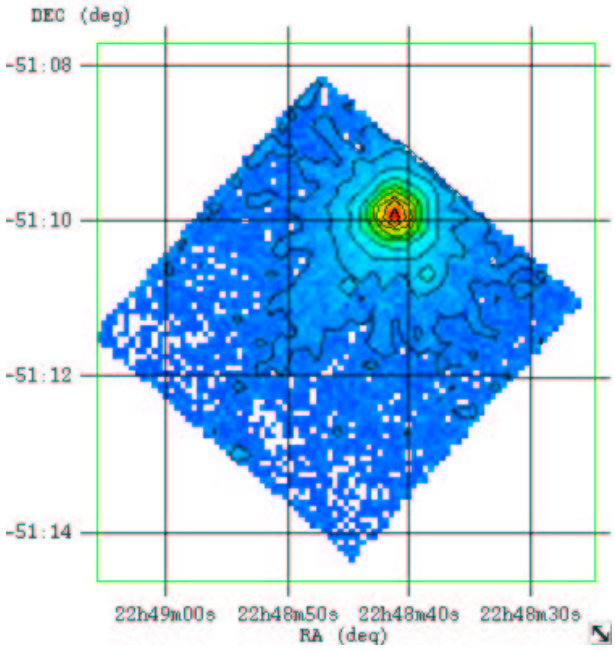

Figure 3.1: X-ray image and intensity contours for the pn small window observation of 26/10/2000. The grid overlaid shows the sky coordinates.

the April 2001 observation an extremely high background flare occurred, and these data cannot be used. The resulting exposure times for the pn are 17.6 ks in October 2000 and 15.4 ks in October 2001. The raw data from both observations were processed with the *XMM-Newton* SAS version 5.3 (public release). Source counts were taken from a circular region of radius 43 arcsec and a background spectrum was obtained from a nearby source-free region, 3.2 times larger in area than the source extraction region, for each pn observation. These spectra were extracted with 5 eV bins, and the EPIC pn small window response file of August 2001 for small window medium filter single events has been used with each.

3.2 X-ray variability

This 6-monthly X-ray monitoring campaign of RE J2248-511 was prompted by spectral variability observed between two previous X-ray missions. Overplotting the 2

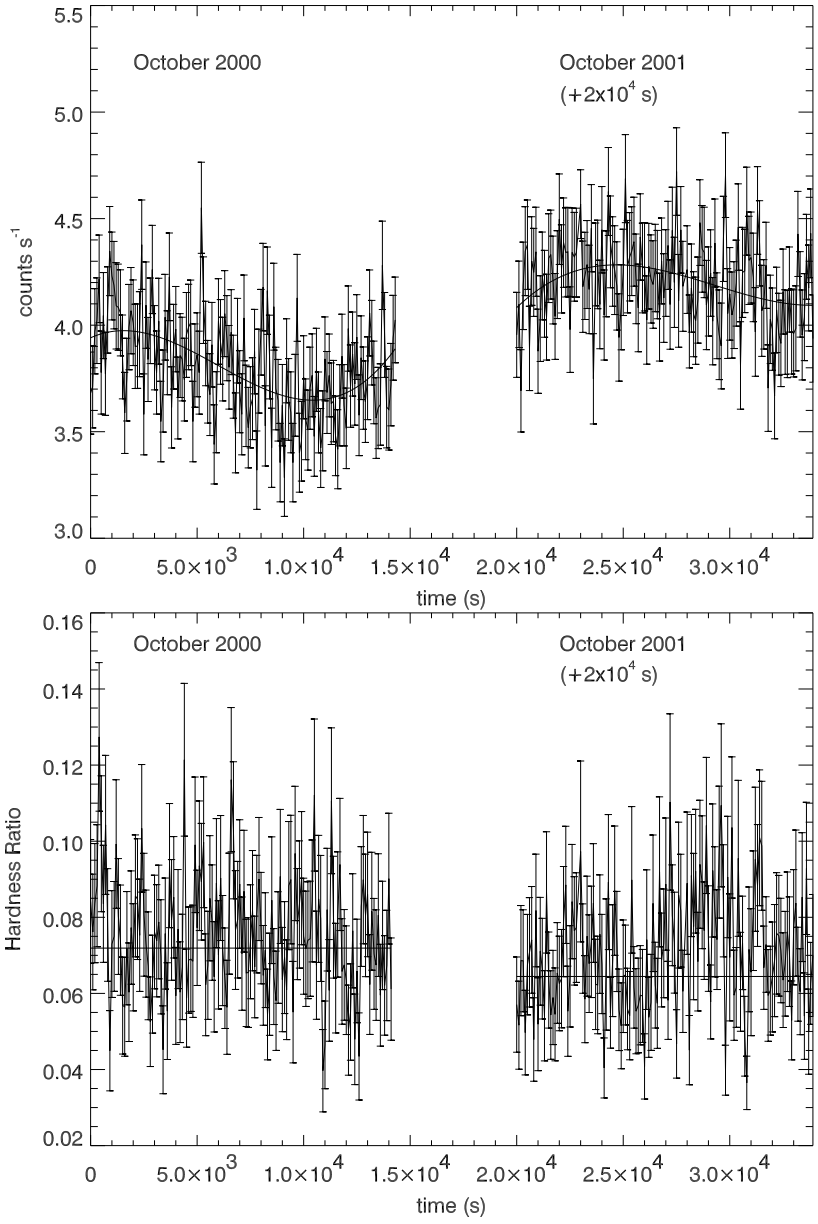

Figure 3.2: Upper plot: background subtracted pn lightcurves for the October 200 and October 2001 observations, binned into 100 s bins. The best polynomial fit is also shown. Lower plot: hardness ratios with the best polynomial fits. In both plots the x axis is time since the start of the observation, with the October 2001 displaced by 20 ks for easier comparison of the count rates.

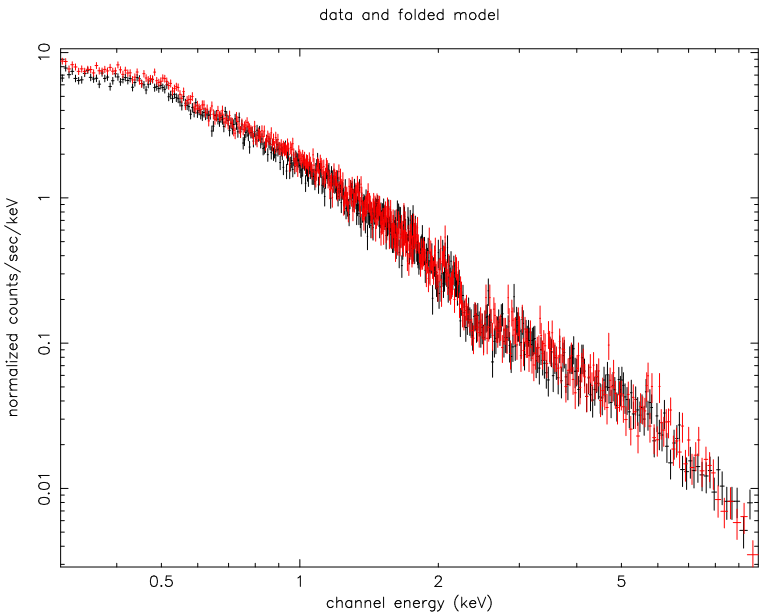

Figure 3.3: The pn spectra for the October 2000 (black) and October 2001 (red) observations.

EPIC pn observations shows that the approximate spectral form is the same in each (Fig. 3.3). Simultaneous fits of the spectra with simple models over the 0.3 - 10 keV range, and fits to the hard (2 - 10 keV) and soft (0.3 - 2 keV) bands separately, confirm that no significant spectral changes have occurred between the observations. The temporal variability during this monitoring campaign is shown in the upper plot of Fig. 3.2. The observations have mean count rates of 3.8±0.2 and 4.2±0.2 count s^{-1}, but are not constant. A third order polynomial is a good fit at the 95% and 90% confidence levels according to the F-test to both the 10/2000 (χ^2/dof = 158/140) and the 10/2001 (χ^2/dof = 122/134) lightcurves, ruling out fits with a constant count rate (χ^2/dof = 211/143 and 147/137). Maximum flux variations within an observation reached 8% in 8700 s. I then extracted the lightcurves for the hard and soft bands separately. The flux over the EPIC energy range is dominated by the soft X-rays, hence hardness ratios of < 1, where the hardness ratio is defined as $HR =$ hard counts/soft counts. The hardness ratios also show deviations from a constant level of $\sim 14\%$ per observation, but the mean hardness ratios are consistent between

the first and second epochs ($< HR > = 0.08 \pm 0.02$ and 0.07 ± 0.02 respectively), and a constant value fit to each is acceptable, with $\chi^2/\mathrm{dof} = 151/141$ and $184/137$. First order polynomials are only slightly better fits to the hardness ratio of the first and second observations respectively however, with χ^2 decreased by 4 and 2, for 1 and 2 extra degrees of freedom in each case. According to the F-test these fits can be rejected with 41% and 50% confidence. The best-fitting polynomials are shown with the data in the lower plot of Fig. 3.2. In one year, this source has shown low level flux variability, of order 10%, and the hardness ratios are consistent with a constant value. Extrapolating this linearly, the flux two-folding or doubling timescale, τ_2, would be 217.5 ks, leading to a constraint on the size of the X-ray emitting region, l, of $l \leq c\tau_2 = 6.5 \times 10^{15}$ cm or 2.52 light days. This locates the emission to at least within the expected radius of the accretion disc (see Fig. 1.4). If this emission comes from the inner radius of the accretion disc, I derive only a poor estimate of the maximum black hole mass of 3×10^{10} $\mathrm{M}_{\odot}$.

3.3 Spectral analysis

I combined the 2 pn observations into a single spectrum to increase signal to noise because no significant spectral or temporal variability occured either during or between them. The coadded spectrum is grouped such that a minimum of 20 counts fall in each channel and χ^2 statistics apply, and bad channels have been ignored. The mean net count rate of the coadded pn spectrum is 5.71 ± 0.02 counts s^{-1}. Spectral analysis was done using the X-ray spectral fitting package XSPEC v11.2, using the χ^2 minimisation technique. I have restricted the considered energy range to 0.3 - 10 keV as the instrument calibration is well understood witin this range. The Galactic column density was included in all models and fixed at 1.4×10^{20} cm^{-2} (Puchnarewicz et al., 1995). All model fits are given in Table 3.1.

I began by fitting the data with the simplest model, a single power law, which provided a good fit to the *ASCA* spectrum of this source (BPO2001). However,

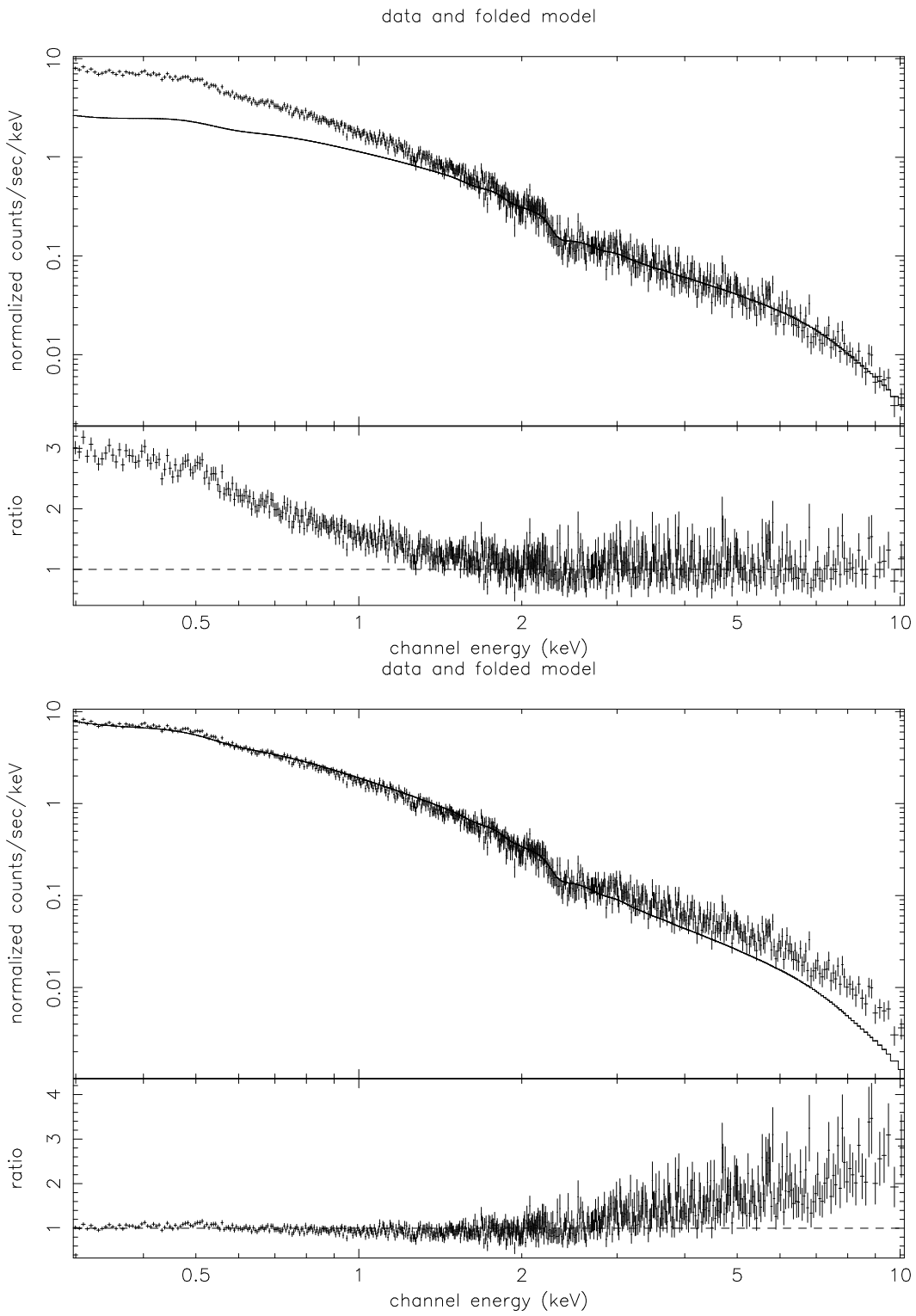

Figure 3.4: The coadded EPIC pn spectrum fitted with a power-law model, fit over the ranges 2 - 10 keV (upper plot) and 0.3 - 10 keV (lower plot). The lower panels of each plot show the ratio of the data to the model fit.

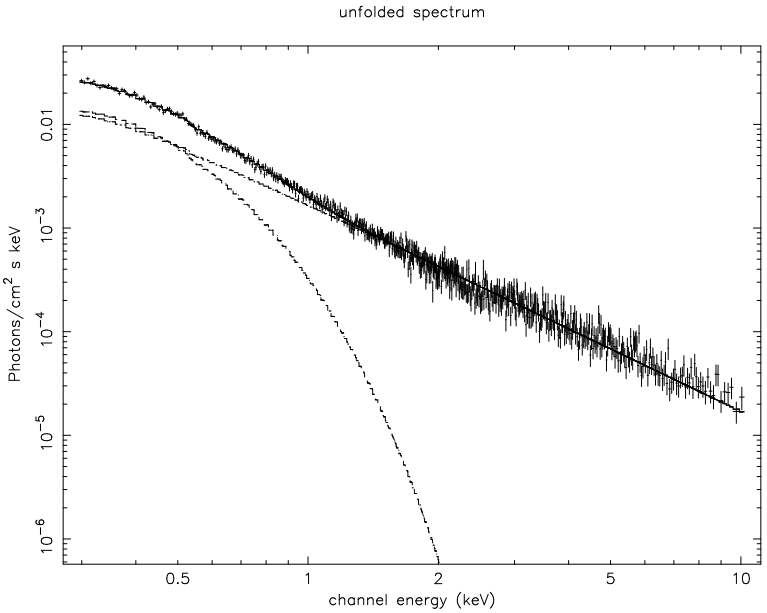

Figure 3.5: The unfolded pn spectrum with the disc blackbody plus power law model.

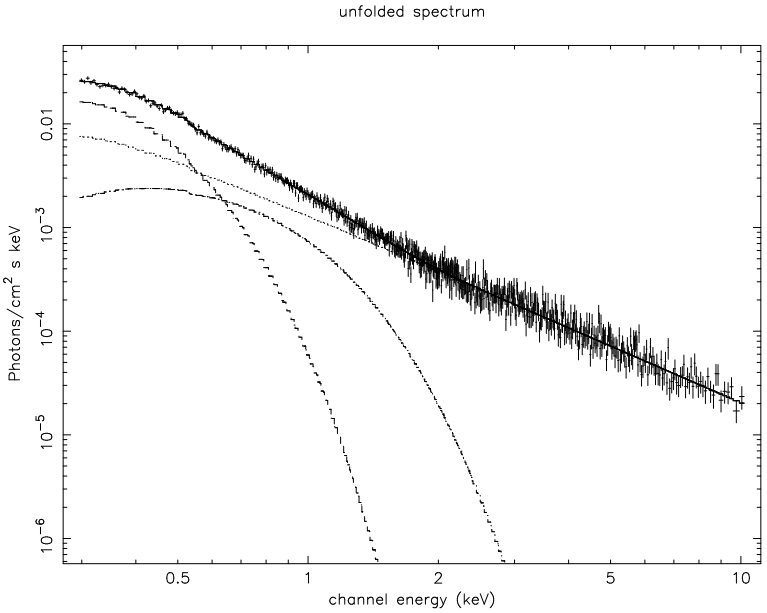

Figure 3.6: The unfolded pn spectrum with the model of 2 blackbodies and a power law.

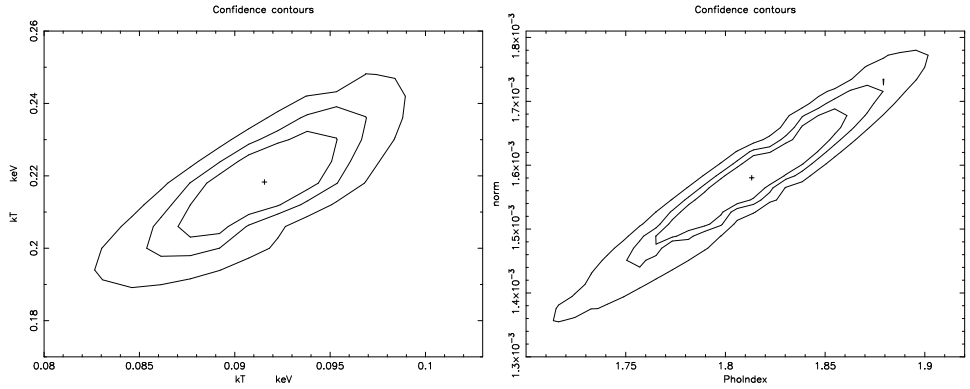

Figure 3.7: Contour plots for the parameters of the 2-blackbodies-plus-power-law model shown in Fig. 3.6: temperatures (kT in keV) of the two blackbodies (left) and the power law photon index and its normalisation (photons cm^{-2} s^{-1}, right) with 68, 90 and 99% confidence contours for two interesting parameters.

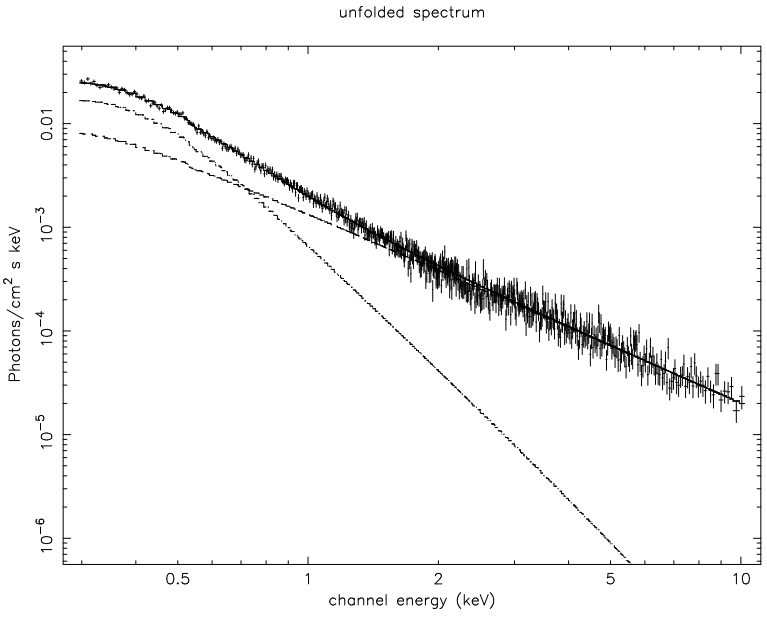

Figure 3.8: The unfolded pn spectrum with the power law plus Comptonisation model.

Table 3.1: Model fits to the pn spectrum in the range 0.3 - 10 keV (unless otherwise stated), with the Galactic column density fixed at $N_{\rm H} = 1.4 \times 10^{20}$ cm^{-2}, redshift fixed at $z = 0.101$ and all errors quoted at the 90% confidence level for 1 interesting parameter. All energies are given in keV, all normalisations are given in photons cm^{-2} s^{-1}. $kT_{\rm plasma}$ and $\tau_{\rm plasma}$ are the temperature and optical depth of the comptonising material respectively. R is the reflection fraction. In the reflection models the power law fold energy was fixed at 100 keV.

Model	Γ	norm/10^{-3}	R	kT_1;kT_2	$kT_{\rm plasma}$	$\tau_{\rm plasma}$	norm$_1$/10^{-3};norm$_2$/10^{-3}	χ^2/dof
PL	2.44 ± 0.02	$2.90^{+0.03}_{-0.02}$	-	-	-	-	-	1408/662
PL 2 - 10 keV	$1.83^{+0.06}_{-0.04}$	$1.64^{+0.12}_{-0.11}$	-	-	-	-	-	306/318
PL+BB	2.07 ± 0.02	2.24 ± 0.07	-	0.113 ± 0.004	-	-	$0.052^{+0.002}_{-0.005}$	790/660
PL+DISKBB	2.00 ± 0.02	2.07 ± 0.02	-	0.15 ± 0.01	-	-	unconstrained	730/660
PL+2BB	$1.81^{+0.05}_{-0.06}$	1.58 ± 0.14	-	$0.092^{+0.002}_{-0.004}$;$0.218^{+0.011}_{-0.014}$	-	-	$0.073^{+0.004}_{-0.006}$;0.027 ± 0.004	647/658
PEXRAV	$2.57^{+0.01}_{-0.02}$	$2.11^{+0.03}_{-0.02}$	19 ± 2	-	-	-	-	721/661
PL+COMPTT	1.84 ± 0.05	$1.53^{+0.05}_{-0.04}$	-	0.079 ± 0.04	< 3[illegible]$^{+0.2}_{-3.1}$	$8.1^{+0.7}_{-8.0}$	680/659	

this is a poor fit to the pn spectrum (χ^2/dof = 1408/662) with large residuals at both the low and the high energy ends of the 0.3 - 10 keV region. These residuals indicate that a soft excess is present, and the high energy residuals may be due to a reflection component or they may indicate that the spectrum does not have a power law shape. However, a power law shaped X-ray component is a feature of almost all AGN, particularly at energies $\geq$ 2 keV where contamination from any soft excess emission and/or warm absorber features is minimal. To test for the latter possibility, I fit the power law model to the restricted range of 2 - 10 keV. A power law fits this range very well with χ^2/dof = 306/318, the hard X-ray slope being consistent with typical Seyfert spectral indices of $1.8 \leq \Gamma \leq 2$. To see whether reflection can account for the curvature in the spectrum, I fitted the pexrav neutral reflector and the pexriv ionised reflector models (Magdziarz & Zdziarski, 1995) to the 0.3 - 10 keV spectrum. In this model the soft X-ray region is fit with a power law, and an enormous reflection fraction of 19 ± 2 is required to obtain a good fit. The reflection fraction does not depend on the ionisation parameter. This is unphysical, so I continued the modelling assuming that reflection contributes negligibly to the pn flux. Since a single power law is a good fit to the 2 - 10 keV range, I combined an underlying power law with models which may represent the soft excess seen in the lower panel of Fig. 3.4. The flux in the soft excess then accounts for $\sim$25% of the total flux measured by the pn. This feature is not well described by a single blackbody component, or a multi-temperature disc blackbody (in this case the diskbb model within XSPEC). The pn spectrum is best fit with a model consisting of two blackbodies dominating at low energies with temperatures $kT_1 = 0.09 \pm 0.01$ keV and $kT_2 = 0.21 \pm 0.03$ keV, plus a power law with $\Gamma = 1.8 \pm 0.08$ (χ^2/dof = 458/468, Fig. 3.6). The X-ray flux in the 0.3 - 10 keV energy range is $1.16 \pm 0.11 \times 10^{-11}$ erg cm^{-2} s^{-1}, corresponding to a luminosity of $3.04^{+0.26}_{-0.29} \times 10^{44}$ erg s^{-1} (assuming H_0 = 70 km s^{-1} Mpc^{-1} and q_0 = 0.0). When adding an intrinsic absorption component I find it is consistent with zero.

In a number of AGN cold iron has been detected and, by adding a Gaussian

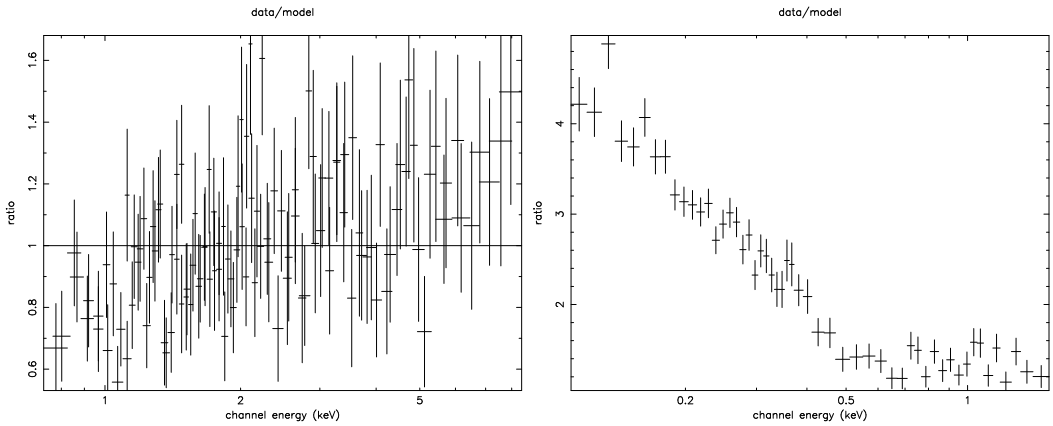

Figure 3.9: The data-model ratio for the *ASCA* GIS2 and GIS3 (left) and *ROSAT* PSPC (right) data and the best-fitting model to the pn spectrum.

emission line to the best-fitting model described above, I test for the presence of iron emission in RE J2248-511. In this case I obtain only upper limits (at 90% confidence) on the equivalent widths of a possible Fe Kα line at 6.4 keV (in the rest frame of the source) of 45 eV for a narrow line ($\sigma = 0.01$) and 105 eV for a broad line ($\sigma = 0.3$). The weakness of any Fe Kα emission suggests that there is no significant reflection in this spectrum.

Comptonisation as a contributor to the X-ray spectrum was discussed for RE J2248-511 in BPO2001 and has been proposed to explain the X-ray spectrum of a number of other AGN including 1H 0419-577 (Page et al., 2001). To investigate whether a Comptonised component can comprise the soft excess, I combined the comptt model within XSPEC (Titarchuk, 1994) with a hard power law (Fig 3.8). However, it is not as good a fit (χ^2/dof = 680/659) as the 2 blackbodies plus power law model, and the parameters of the Comptonised component are poorly constrained.

3.4 Comparison with *ASCA* and *ROSAT*

RE J2248-511 was observed in 1993 with *ROSAT* and over its energy range of 0.1-2 keV the spectrum was found to be very soft (P95). Four years later an *ASCA* observation found that the spectrum consisted of a power law and no soft excess flux was detected (BPO2001). I now fit these previous spectra with the best-fitting model to the *XMM-Newton* EPIC pn coadded spectrum (Fig. 3.9), and compare all three observations in the overlapping energy range, to examine the long-term variability.

ASCA: SIS and GIS data are available for this source, but because the gain calibration for SIS below 1 keV is known to be incorrect (see e.g. George et al., 1998) I fit only the GIS2 and GIS3 data (simultaneously) in this analysis. In the 2 - 10 keV range, the power law photon index and normalisation are consistent within the errors. Below 2 keV the flux observed with the pn is much higher than in the GIS spectrum: the blackbody components needed to fit the pn data must be removed to obtain a good fit to the GIS soft X-ray spectrum.

ROSAT: A soft X-ray excess is observed in both the pn and PSPC spectra, but the best-fitting model to the EPIC pn spectrum is not a good fit to the the PSPC spectrum. The 0.1-2 keV flux of the pn spectrum is one third smaller than measured by the PSPC; pn flux = 8.4051 $\times 10^{-12}$ erg cm^{-2} s^{-1}, PSPC flux = 1.186 $\times 10^{-11}$ erg cm^{-2} s^{-1}. After fixing the power law photon index and normalisation at the values best-fitting the pn data, the PSPC spectrum is adequately fit with this power law plus 2 blackbodies of lower temperatures than needed for the pn data (χ^2/dof = 59.8/49). The PSPC data are slightly better fit with a broken power law model (χ^2/dof = 53.3/49).

I am able to directly compare the data from all three missions if I fit only the overlapping energy range of 0.7 - 2 keV with a power law (Table 3.2). Over this small range the spectral slope of RE J2248-511 during the *XMM-Newton* and *ROSAT* observations may be consistent, and are both in a softer state than during

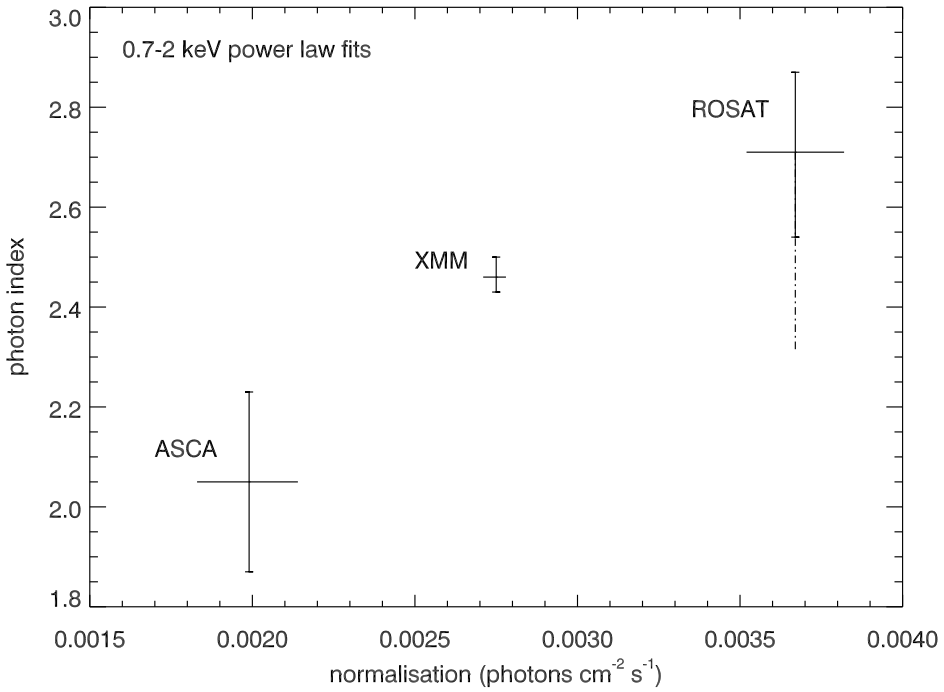

Figure 3.10: Comparison of the power law photon index and normalisation for the *ROSAT* PSPC, *ASCA* GIS and *XMM-Newton* EPIC pn spectra in the overlapping energy range 0.7 - 2 keV and with 90% error bars. The dot-dashed line on the *ROSAT* point shows the maximum apparent steepening which may be seen in PSPC slopes due to instrumental effects.

Table 3.2: Power law fits to the *ROSAT* PSPC, *ASCA* GIS 2 and 3 (fitted simultaneously) and EPIC pn data in the overlapping range of 0.7 - 2 keV, with redshift fixed at $z = 0.101$ and Galactic absorption fixed at 1.4×10^{20} cm^{-2}. All errors are quoted at the 90% confidence level for 1 interesting parameter.

Instrument	Γ	norm/10^{-3}	χ^2/dof
ROSAT PSPC (1993)	$2.71^{+0.16}_{-0.17}$	3.67 ± 0.15	25.3/17
ASCA GIS (1997)	2.05 ± 0.18	$1.99^{+0.15}_{-0.16}$	60.3/58
EPIC pn (2000-01)	$2.50^{+0.04}_{-0.03}$	$2.75^{+0.03}_{-0.04}$	253/263

the *ASCA* observation. I caution that *ROSAT* probably has some 'contamination' from lower energy emission due to the very limited spectral resolution of the PSPC, resulting in an observed slope which may be up to Γ+0.4 steeper than the true slope. It is also true that since the spectral energy coverage of *ASCA* is predominantly in the hard range these observations are likely to contain a bias towards harder spectra. The effective area of all 3 missions is compared in Fig. 1.7. The flux evolution argues against 'two-state' behaviour, and RE J2248-511 may be viewed as being in an intermediate brightness state in the epoch of the *XMM-Newton* observations.

3.5 Optical and IR observations

RE J2248-511 was observed in the same week as the first *XMM-Newton* observation on 19 - 24 October 2000 using the South African Astronomical Observatory's 1.9m Radcliffe telescope, by myself and E. Romero-Colmenero. On each of the nights of 19th, 21st and 23rd, spectra were taken using both a wide (4.2 arcsec) and a narrow slit (1.8 arcsec) with overlapping blue and red gratings ($\lambda_{\rm central}$ = 4600, 7800Å). Arc spectra were taken before and after every target and every standard spectrum using a CuAr lamp. The standard star LTT 9239 (J2000 position 22h52m41s,-20d35m33s) was observed for flux calibration of RE J2248-511 (J2000 position 22h48m41.2s,-51d09m54s). Measurements of the IR magnitudes in the *J,H,K* bands were made on a single night with the infrared photometer. 12 measurements in *J*, 6 in *H* and 3 in *K* were made on 17 October 2000. The *JHK* magnitudes are quoted in the SAAO photometric system (Carter, 1990), and were converted from the telescope measurements by E. Romero-Colmenero. These are given in Table 3.3.

3.5.1 Summary of optical data reduction

I extracted the spectra individually using routines within the Image Reduction and Analysis Facility (IRAF). Here I will briefly outline the data reduction and extraction steps.

Table 3.3: *JHK* magnitudes for RE J2248-511. The 2MASX results are taken from the 2 Micron All Sky Survey Extended objects - Final Release, 2003 catalogue.

J	*H*	*K*	date	ref.
14.423±0.102	13.639±0.084	12.657±0.064	17/10/00	this work
15.061±0.169	14.315±0.175	13.948±0.268	21/09/99	2MASX (total passband)
15.165±0.138	14.572±0.162	14.007±0.207	21/09/99	2MASX (14 arcsec)
15.326±0.118	14.673±0.131	14.177±0.178	21/09/99	2MASX (K20)

The images contain bias strips on either end. For each image the average of a cubic spline fit to these was used for debiasing and the bias strips cut from the images. Ten dome flats were taken at the beginning of each evening and combined into a single flat field. The images were then divided by the combined scaled flat field to correct for the spectral signature of the CCD. Cosmic rays were identified as pixels with fluxes 25x greater than the mean of their neighbouring pixels. The pixels affected by cosmic rays were replaced by the average of their four neighbours. Once I had identified the sky and spectrum regions in the object and standard images, the sky background level was fitted and then removed from the extracted spectrum. The arcs have been extracted in exactly the same way. The arc lines were identified using a CuAr line list and fitted with a chebyshev function. Identified arcs were assigned to object and standard spectra by time stamps to wavelength calibrate the RE J2248-511 spectra. The flux and spectral shape of the standard star LTT 9239 is well known over this waveband, and was compared to the observed flux for calibration.

3.6 Results from the optical spectrophotometry

The spectra show many emission lines typical of AGN spectra and the Balmer lines (Hα, Hβ, Hγ, Hδ and Hϵ) are broad. The spectral resolution is 4.6 Å and 6.2 Å in the red and blue grating narrow slit spectra respectively. Seeing, humidity and

cloud cover were variable during the observing period and consequently only one of the nights could be considered photometric. However, the continuum flux levels of the three observations do not show significant variability (Fig. 3.11). The spectra were not taken at the parallactic angle, but the airmasses at which RE J2248-511 and the standard star LTT 9239 were observed on each night were only 1.06 - 1.09. Therefore, the wide slit observations will not be greatly affected by atmospheric dispersion.

3.6.1 The broad-line region

Spectral fitting was done with the Starlink DIPSO v3.6 spectral fitting package. The continuum under each line was approximated by a first order polynomial in the immediate vicinity of the line blend, Gaussian profiles were assumed for the line profiles and a least squares procedure is used to minimise the residuals of the fit. The emission lines, like the continua, do not differ significantly between the three observations (Fig. 3.12). Both Hα and Hβ are best fit with three Gaussians as shown in Fig. 3.13: narrow, intermediate and broad components (Table 3.4). Towards the blue end of the spectrum the noise increases and the weaker broad lines of Hγ and Hδ are fit with only double and single Gaussian components respectively. The positions of the line centres indicate a redshift of $z = 0.1015$. The ratio of Hα to Hβ average line flux, excluding the narrow-line component, is Hα/Hβ = 4.2, which is comparable to the measured value of 4.4 in the 1992 spectrum (Grupe et al., 1999; the 1991 spectra (P95) does not cover the Hα waveband). I note that Grupe et al. did not fit the [N II] lines blended with Hα as I have done, but estimated their flux to comprise 35% of the total measured flux of [O III]λ5007 and subtracted this amount. They also included the narrow component of the Balmer lines in their Hα/Hβ ratio, though this does not differ appreciably from the ratio of the broad components alone.

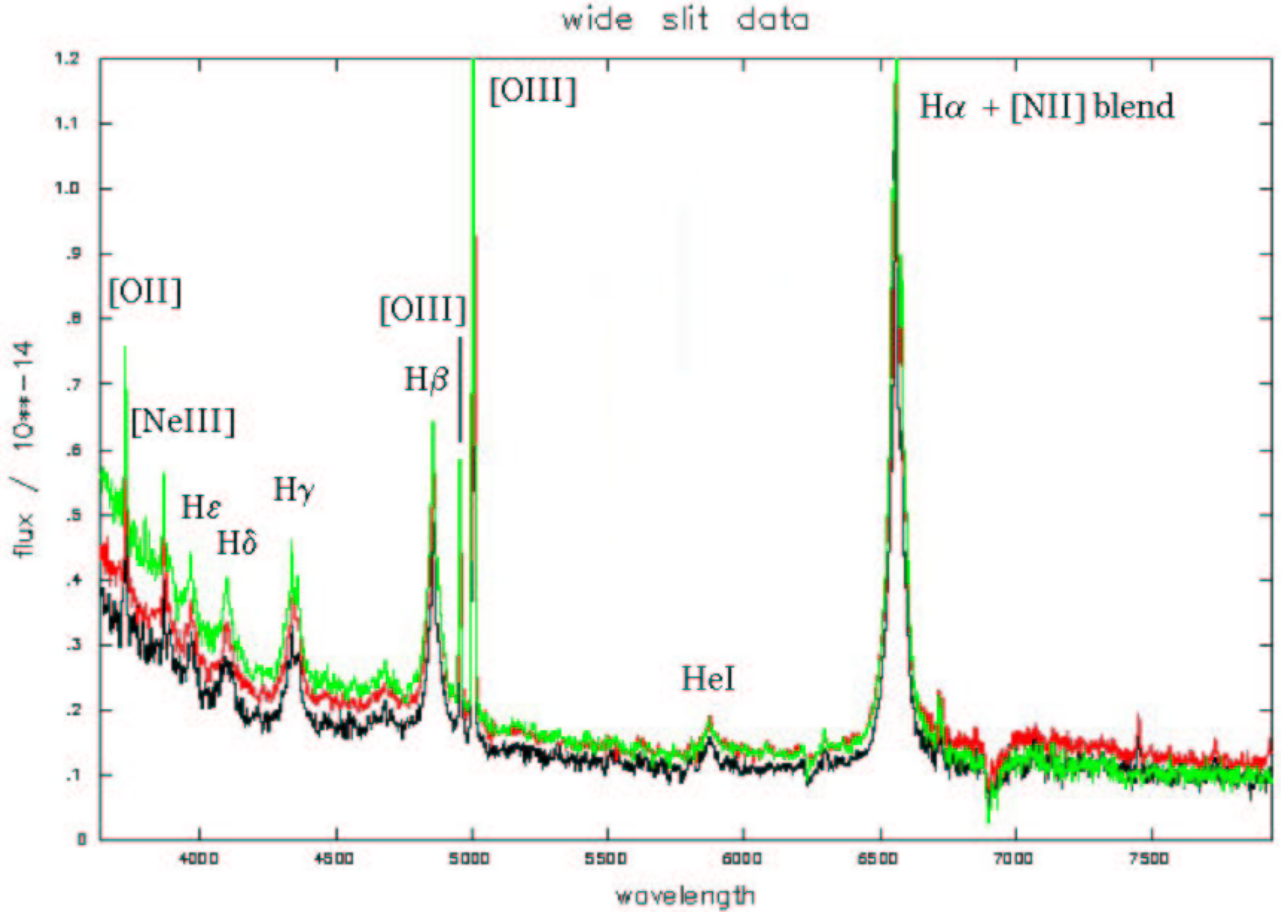

Figure 3.1: Merged wide slit data for all three observations, with wavelength in Å in the source rest-frame and flux in erg cm^{-2} s^{-1}. Black line = 19-20/10/00, red line = 21-22/10/00, green line = 23-24/10/0.

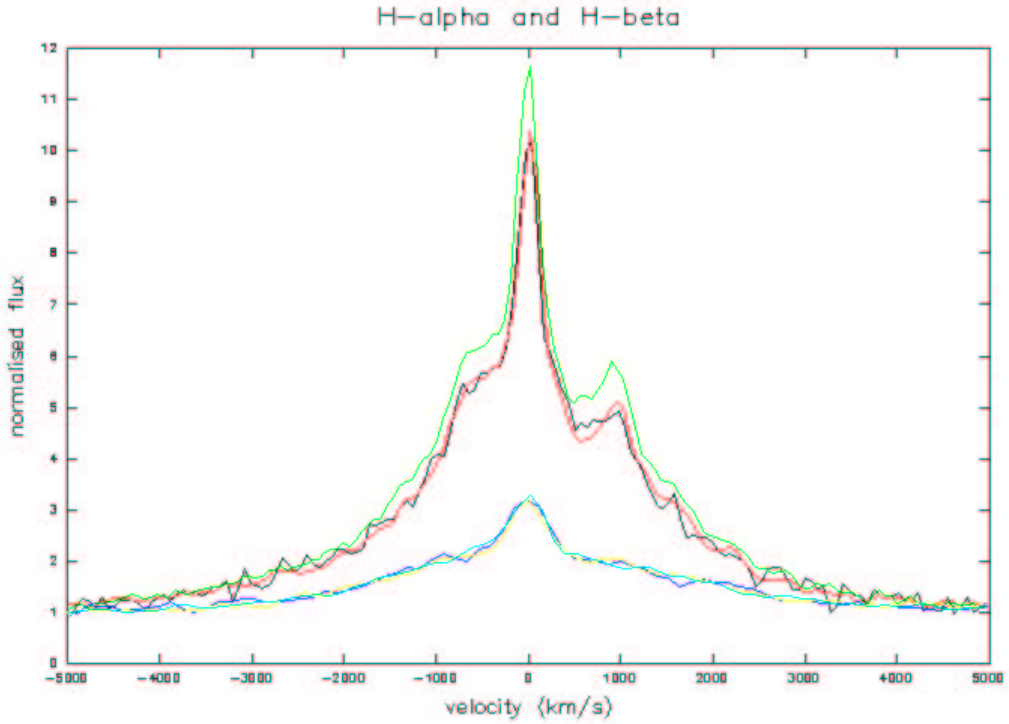

Figure 3.12: Comparison of the Hα (upper 3 curves) and Hβ (lower 3 curves) lines in velocity space for all three narrow slit observations. Black/dark blue lines = 19-20/10/00, red/yellow lines = 21-22/10/00, green/light blue lines = 23-24/10/00. A local continuum fit with a second order polynomial was used to obtain the normalised flux.

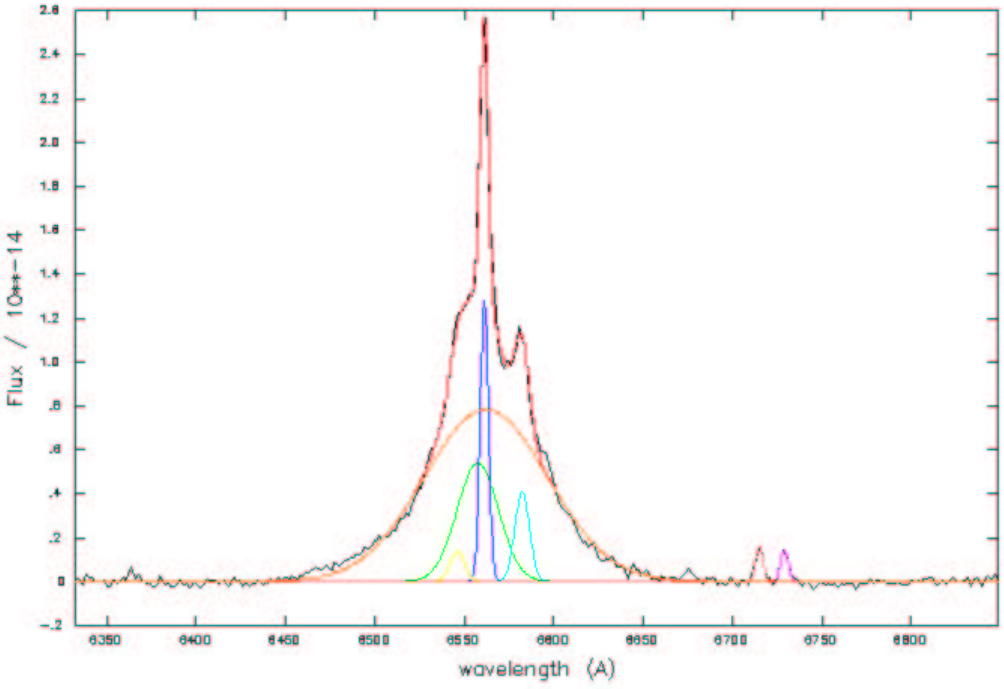

Figure 3.13: Continuum-subtracted data and best-fitting model for the Hα+[N II] line blend and [S II] doublet, of the narrow slit observation of 23-24/10/00, where Hα is fit with 3 Gaussian components. The [N II] doublet is fit with single Gaussians tied to have equal widths and an intensity ratio of 1:3 (yellow and light blue lines). The data are shown in black, best-fitting model line blend in red and individual model components in various other colours.

Table 3.4: Averages of the optical emission line measurements for prominent lines.

Line	restframe position (Å; $z = 0.1015$)	flux (10^{-13} erg cm^{-2} s^{-1})	FWHM (km s^{-1})	EW (Å)
[S II] doublet	6715;6730	0.05;0.04	202.1	3.14;2.10
Hα broad	6562	4.39	3804	247
Hα intermediate	6558	1.09	1218	80.8
Hα narrow	6561	0.46	235.4	22.9
[N II] doublet	6545;6583	0.09;0.27	442.6	4.74;14.2
Hβ broad	4864	1.21	3748	81.9
Hβ intermediate	4855	0.11	1266	7.2
Hβ narrow	4862	0.12	421.3	8.1
Hγ broad	4338	0.63	4764	38.2
Hγ narrow	4341	0.09	774.9	5.1
Hδ single Gaussian	4100	0.55	2930	31.5
[O III] λ5007	5008	1.12	497.9	84.5
[O III] λ4959	4960	0.35	481.9	24.3
[O II]	3728	0.25	691.1	8.0
[Ne III]	3874	0.09	499.4	3.8

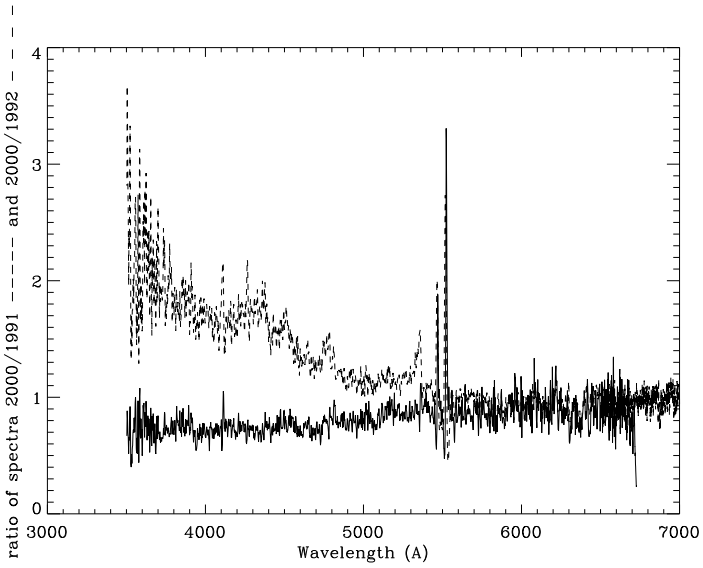

Figure 3.14: Ratio of the optical spectra from different epochs: 2000/1991 solid line, 2000/1992 dot-dashed line.

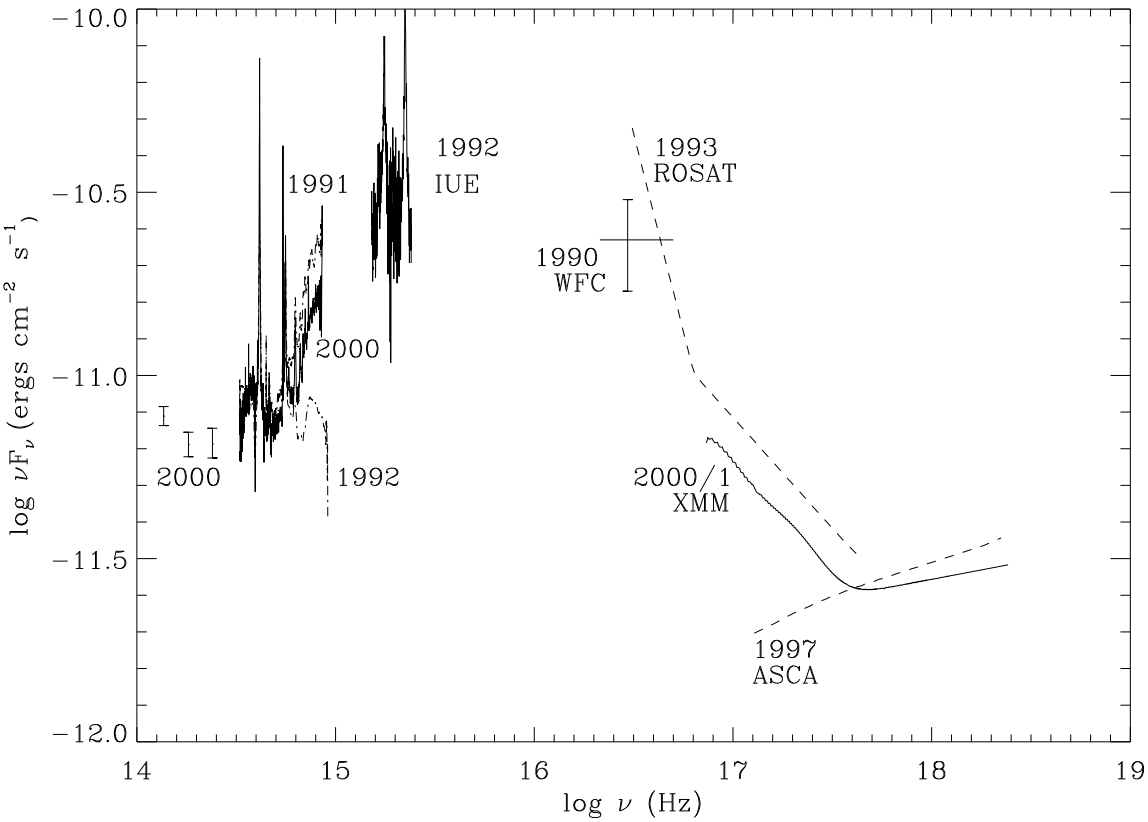

Figure 3.15: Spectral energy distribution from optical to X-ray for RE J2248-511 including all available optical and UV data and best-fitting X-ray models, spanning 1990 to 2001.

3.6.2 UV data

An ultraviolet observation was made with both the Short Wavelength Prime (SWP) and Long Wavelength Redundant (LWR) cameras on-board the International Ultraviolet Explorer (IUE) satellite in 1992. The SWP instrument covers the spectral region 1150 - 2000 Å with a resolution of $\sim$ 5 Å in low dispersion mode. The LWR covers 1900 - 3200 Å with an 8 Å resolution. These data are, to my knowledge, unpublished. The data were taken from the archive as pipeline processed, reduced spectra. I use only the continuum spectrum here, to determine the size of the UV bump in the spectral energy distribution of RE J2248-511.

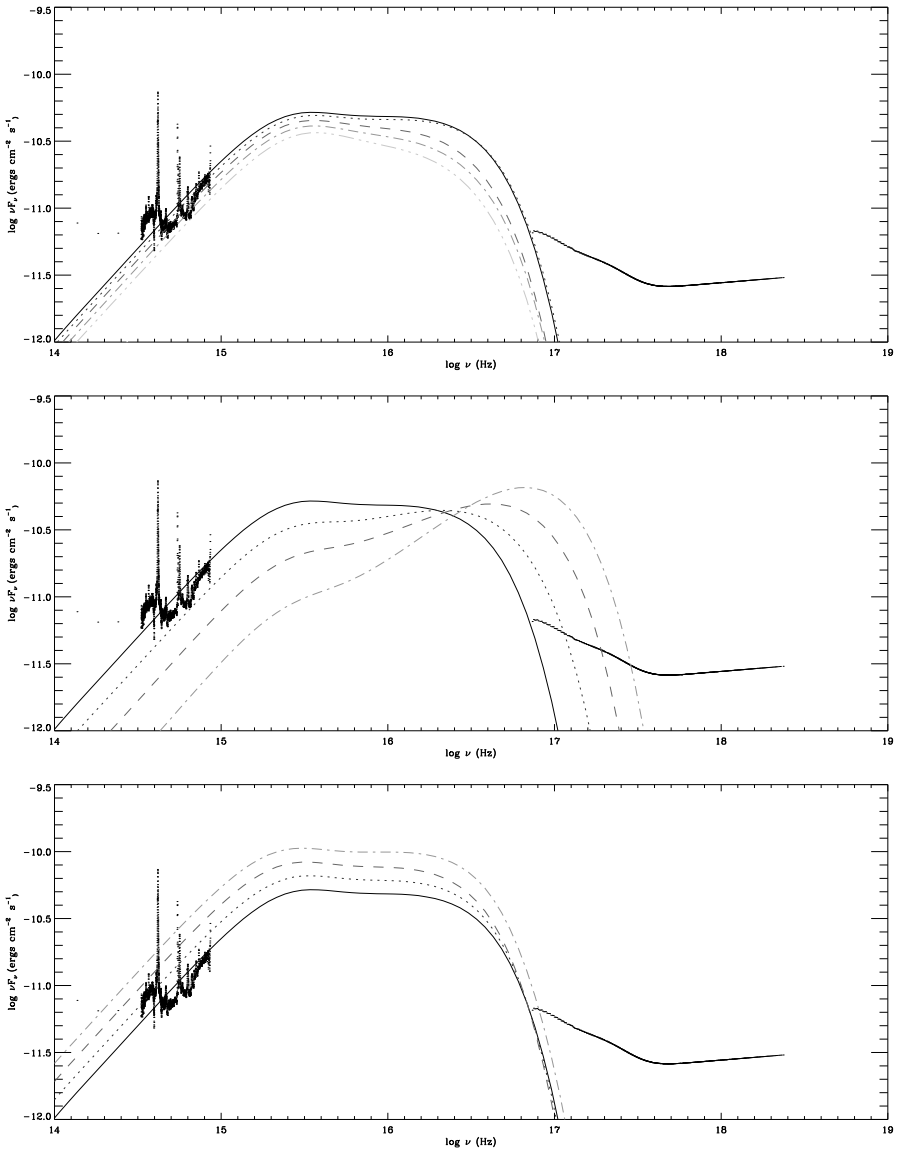

Figure 3.16: The SED for October 2000 and sets of Comptonised disc model fits.
Top panel - varying accretion rate: $M = 10^8\,\mathrm{M}_\odot$, $\cos(i) = 0.8$, $\dot{M}$ = (darkest to lightest) 0.8 (solid line), 0.7 (dotted line), 0.6 (dashed line), 0.5 (dot-dashed line), 0.4 (triple-dot-dashed line) $\dot{M}_{\mathrm{Edd}}$.
Middle panel - varying inclination: $M = 10^8\,\mathrm{M}_\odot$, $\dot{M} = 0.8\dot{M}_{\mathrm{Edd}}$, $\cos(i)$ = (darkest to lightest) 1.00 (solid line), 0.75 (dotted line), 0.50 (dashed line), 0.25 (dot-dashed line).
Lower panel - varying mass: $\cos(i) = 0.8$, $\dot{M} = 0.8\dot{M}_{\mathrm{Edd}}$, M = (darkest to lightest) $10^{8.0}$ (solid line), $10^{8.1}$ (dotted line), $10^{8.2}$ (dashed line), $10^{8.3}$ (dot-dashed line).

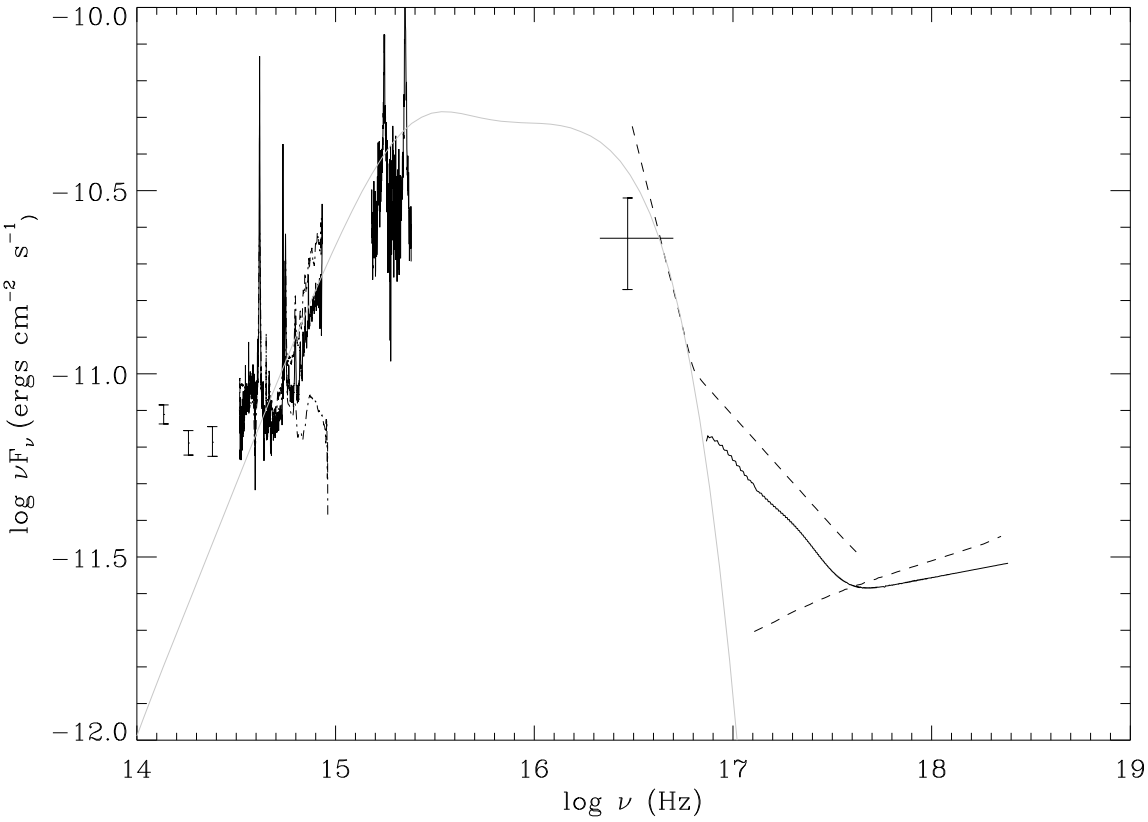

Figure 3.17: The best-fitting model shown in Figure 3.16 and data from all epochs is shown.

3.6.3 The big blue bump and accretion disc models

In Fig. 3.15 all available multiwavelength data for RE J2248-511 is plotted as an SED to show the various flux levels that have been observed. A strong big blue bump is present at most epochs, and the IR photometry indicates an infrared bump also. Comparison of our IR magnitudes with the 2MASS catalogue shows a minimum variability of 0.37 magnitudes in J, 0.42 magnitudes in H and 0.96 magnitudes in K. There is a large discrepancy, up to a factor of two at the blue end, between the optical spectral slope I observe and the slope measured in 1992 (Grupe et al., 1999). However when compared with the 1991 spectrum (Mason et al., 1995) the difference is at most 30% (Fig. 3.14). Since the soft X-ray data from 2000/01 rises towards the UV and is well fit with blackbody models, I investigate the possibility of the entire optical to soft X-ray flux originating in an accretion disc. I use Comptonised accretion disc models developed by Czerny & Elvis (1987, see Chapter 2) with a Kerr black hole, and in which electron scattering occurs in the disc at high temperatures, and fit these to the spectral energy distribution for October 2000. Several models are shown with the data in Fig. 3.16 to illustrate the effects of varying different parameters. The variable parameters of the model are black hole mass, accretion rate and disc inclination. It is clear from Fig. 3.16 that the inclination can be well constrained. Inclination angles of < 0.75 are ruled out since at low inclination angles (more edge-on discs) the ratio of optical to X-ray flux produced is too low. Black hole mass and accretion rate are more difficult to constrain since they are dependent upon each other. From this modelling the black hole mass range for these data is $10^{7.5} \leq M \leq 10^{8.5}\,\mathrm{M}_{\odot}$. High accretion rates $\geq 0.4\dot{M}_{\mathrm{Edd}}$ are favoured. Large black hole mass, high accretion rate face-on disc models follow the optical slope reasonably well and are not inconsistent with the soft X-ray data (Fig. 3.17). The soft X-ray excess cannot, however, be due entirely to thermal emission from an accretion disc.

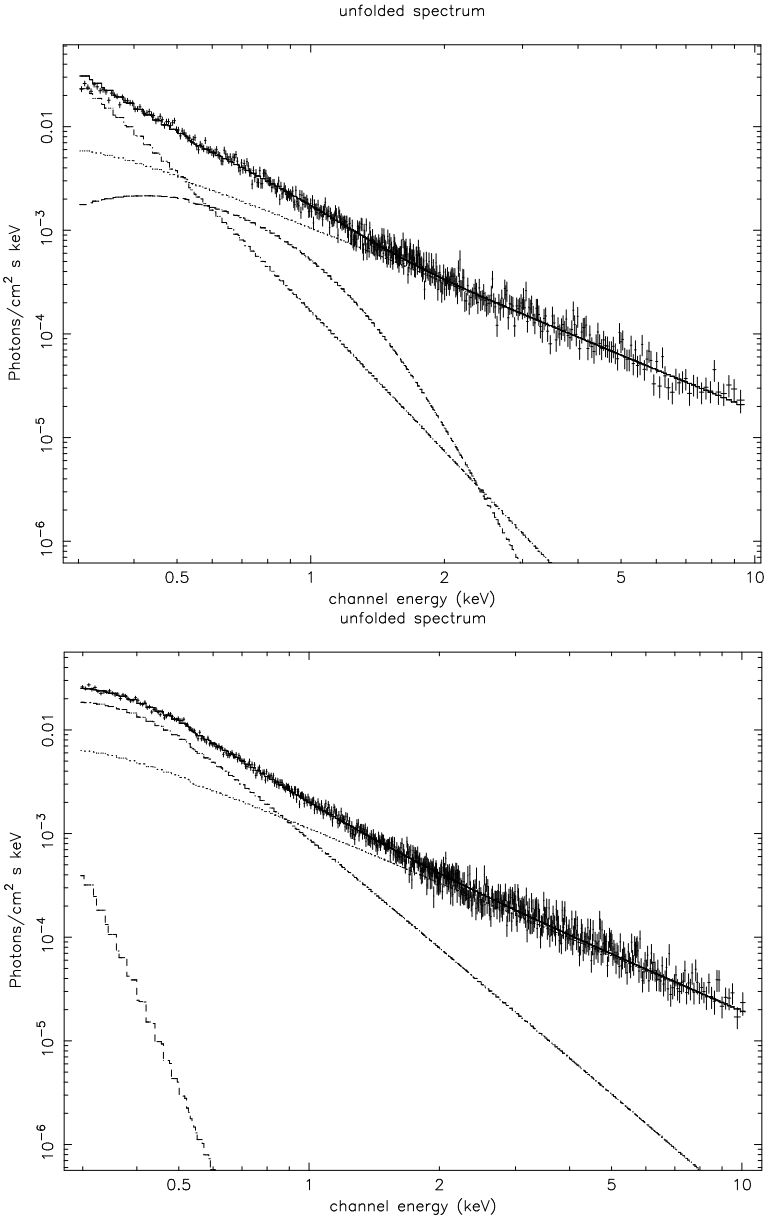

Figure 3.18: The unfolded spectrum and individual model components in the model consisting of a hard power law plus comptt plus a power law representing the tail of the disc blackbody. In the upper plot the soft X-ray power law is taken from the *ROSAT* fit. In the lower plot this power law is steeper with a lower normalisation in an attempt to allow for curvature in the blackbody tail.

3.7 Black hole mass estimates

A lower limit on the black hole mass can be determined by assuming that RE J2248-511 is not emitting at greater than the Eddington luminosity,

$$L_{\rm Edd} \cong 1.3 \times 10^{38} \frac{M}{\rm M_\odot} \text{ erg s}^{-1} \tag{3.1}$$

(e.g. Frank, King & Raine, 1992). The observed X-ray 0.1 - 10 keV luminosity is $L_{\rm X} = 3 \times 10^{44}$ erg s^{-1}, which if I assume is equal to 37% of the bolometric luminosity (Elvis et al., 1994), gives a lower limit for the black hole mass of $M \geq 6.22 \times 10^6$ M$_\odot$. This is not a strong constraint, but is consistent with the constraints obtained from the comparison of accretion disc models with the SED (Section 3.6.3) of $\sim 10^8$ M$_\odot$ $\pm$0.5 decades.

In order to test the validity of the accretion disc model I can also estimate the black hole mass from the optical emission line widths. This is possible using the empirical relationship between BLR size and monochromatic luminosity at 5100 Å (Kaspi et al., 2000)

$$R_{\rm BLR} = 3.29 \left(\frac{\lambda L_\lambda (5100 \text{ Å})}{10^{44} \text{ erg s}^{-1}} \right)^{0.7} \text{ lt day.} \tag{3.2}$$

By applying the Virial Theorem to the BLR the black hole mass can be estimated from the BLR radius and emission line widths using

$$M = R_{\rm BLR} V^2 G^{-1} \tag{3.3}$$

(Wang & Lu, 2001) where V = FWHM$\times\sqrt{3}/2$. For RE J2248-511 this gives a BLR size of 45 - 90 light days ($\sim$ 0.07 pc) and a black hole mass of 10^8 M$_\odot$. The uncertainty in the mass value is approximately 0.5 decades.

The mass and accretion rate I estimate from the latter two methods imply an inner disc effective temperature of kT = 90 eV, assuming an accretion efficiency of 0.08 and using a Kerr geometry with $R_{\rm inner} = GM/c^2$. This agrees with the temperature of the low-energy blackbody component fitted to the *XMM-Newton*

spectra in the 2-blackbodies-plus-power law model (Section 3.3; Table 3.1). However, the temperature measured by the X-ray blackbody models is the colour temperature, which may be much higher than the effective temperature if the spectrum is modified by electron scattering. For example, Borozdin et al., (1999) find a ratio of 2.6 for $T_{\rm colour}$:$T_{\rm eff}$ in Galactic soft X-ray transients. If I take this into account I would find an effective temperature as measured by the X-ray spectral modelling of $kT = 35$ eV for the disc inner radius. This is no longer in agreement with the effective temperature of $kT = 90$ eV derived from multiwavelength modelling.

3.8 The broad-band X-ray spectrum

Having found that an accretion disc with a high energy tail in the soft X-rays is a plausible explanation of the optical observations, I will now use this information in understanding the X-ray spectrum. The steeper slope of the broken power law fitted to the *ROSAT* data (P95) appears to follow the best-fitting accretion disc model closely (Fig. 3.17). I have, therefore, included this tail in a re-fit of the *XMM-Newton* EPIC data. The hard X-ray power law appears to be a constant feature and so I also include that. The remaining excess flux lies between 0.3 and 2 keV. I began by fitting this with a Comptonised component, but the temperature, optical depth and input photon temperature are unconstrained. A single blackbody of temperature $kT \sim 0.2$ keV is a better fit, though this cannot be emission from the accretion disc as the SED modelling has shown. In fact, the contribution from this lowest energy component appears overestimated by this method (c.f. Fig. 3.17), possibly because modelling it with a power law does not allow for curvature. To include this in some form I replaced the *ROSAT* power law with a very steep, low normalisation power law (Fig. 3.18). In this case the remaining soft excess emission can be fit with a blackbody of approximately $kT = 0.1$ keV and normalisation $= 5.1{\times}10^{-5}$ photons cm^{-2} s^{-1}. As found when fitting the data without a steep soft X-ray power law in Section 3.3, an adequate fit can also be achieved with Comptonisation of an

incoming photon distribution of temperature ~ 80 eV by an optically thick medium, where the parameters are poorly constrained.

3.9 Discussion

3.9.1 The X-ray emission

The pn spectrum, composed of 2 coadded observations, shows a hard power law and a large soft excess below 2 keV with a flux of 2.49×10^{-12} erg cm^{-2} s^{-1}. The best-fitting model is a power law ($\Gamma = 1.81^{+0.05}_{-0.06}$) plus 2 blackbodies ($kT_1 = 0.092^{+0.002}_{-0.004}$ and $kT_2 = 0.218^{+0.011}_{-0.014}$). I do not detect any line emission, suggesting that reflection is not significant in the pn energy range. The high luminosity of this source, $L_{\rm X}$ $= 3 \times 10^{44}$ erg s^{-1}, approaches values measured for quasars in which the disc may be irradiated too strongly to produce observable reflection signatures. The X-ray spectrum is curved below 2 keV, and over this range a better fit is obtained with multi-component models rather than with a single component. The accretion disc model fit to the optical to X-ray spectral energy distribution does not contribute significantly to the soft X-ray flux observed with *XMM-Newton*. An accretion disc certainly does not constitute the soft excess as observed with the pn, but it could be the origin of the 'ultrasoft' component below 0.25 keV observed with *ROSAT* (Fig. 3.17). The 0.3 - 2 keV soft component has a blackbody-like shape, but is too hot to be blackbody disc emission. A model including Comptonisation of soft photons in a hot plasma provides a good fit. The input photon distribution has a temperature of 79$\pm$4 eV, but I obtain poor constraints on the parameters of the Comptonising material. The hot plasma may be part of a corona over the accretion disc, intercepting some of the inner disc emission.

In the 1 year period between the first and last *XMM-Newton* observations, the X-ray flux showed variability of order 10%. Small amplitude variability is a characteristic of all AGN, and does not provide a good constraint on the black hole mass,

$M \leq 3 \times 10^{10}\,\mathrm{M}_{\odot}$, but this constraint is at least consistent with all other methods of black hole mass estimation used here. Between the *XMM-Newton* observations, the X-ray spectral shape of RE J2248-511 remained approximately constant. This demonstrates that the 'soft' state is a long-lived phase, and not, for example, a rapid flaring of the disc. Between the *ASCA* and *XMM-Newton* observations the 2 - 10 keV spectrum remained constant. The ultrasoft component has only been observed by *ROSAT*, since *ASCA* and *XMM-Newton* do not cover the very low X-ray energies, so its variability is unknown. The soft X-ray component observed with *ROSAT* (P95) subsequently disappeared in the *ASCA* observation (BPO2001), and now seems to have re-appeared with about one third less flux and remained constant during the *XMM-Newton* observations. If this is Comptonised emission, the transition between a flat spectrum and a soft spectrum could be explained by a change in optical depth of Comptonising material. This scenario has been suggested for the Seyfert 1 galaxy 1H 0419-577 (Page et al., 2001) and for this source in BPO2001. Alternatively, the Comptonising material could had moved out of our line-of-sight during the *ASCA* observation, though this is unphysical if the material is part of a disc corona unless this material has been ejected from the corona in an outburst or wind.

3.9.2 The big blue bump

In the quasi-simultaneous optical and X-ray observations made in 2000, RE J2248-511 has a soft X-ray spectral state and a steepening of the optical continuum towards the blue; both bands pointing to big blue bump emission. In addition, both components have shown spectral variability in the past, suggesting a link between them. I have shown that Comptonised accretion disc models, which treat the optical to soft X-ray emission as a single BBB, are able to comprise the majority of this flux. From these I derive constraints on the black hole mass which are fully consistent with the mass I obtain through the independent photoionisation technique. This implies that thermal disc emission is the likely origin of the optical, UV and some

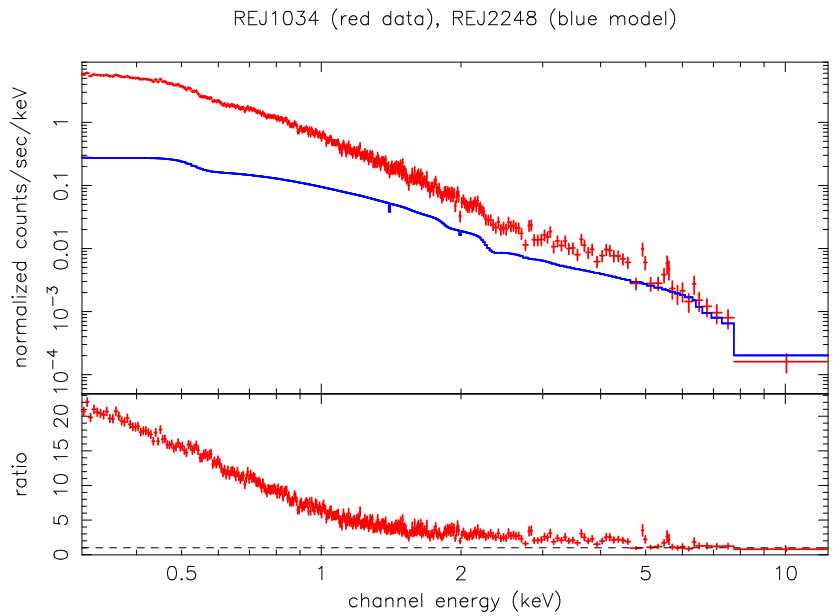

Figure 3.19: Comparison of the best-fitting model to the EPIC spectra of RE J2248-511 (blue line) with the *XMM-Newton* EPIC observation of the NLS1 RE 1034+396 (red data points). Courtesy of R. Soria.

of the soft X-ray continuum. Optical/UV and soft X-ray emissions are generally well correlated (Walter & Fink, 1993; Puchnarewicz et al., 1996; Laor et al., 1997), supporting the idea that they are part of a single component.

Contrary to the proposed NLS1 scenario (e.g. PDO95), the data are best fitted with high black hole masses ($10^{7.5} - 10^{8.5}$ $M_{\odot}$), whilst still favouring the high accretion rates suggested for NLS1 galaxies. Therefore, it is not necessary for a black hole to have a low mass for the formation of an ultrasoft X-ray excess. Comparison of Comptonised accretion discs to the SED show that the orientation of the disc is close to face-on, allowing us to see a greater surface area of the accretion disc. If most of the EUV emission arises in the accretion disc then this source would appear EUV-bright compared with similar Seyfert galaxies viewed at higher inclination angles.

3.9.3 The true nature of RE J2248-511

RE J2248-511 displays observational characteristics of both normal and narrow-line Seyfert 1 galaxies. Of the 3 EUV-excess AGN selected by the *ROSAT* WFC, RE J2248-511 was the only broad-line galaxy. But since then 2 other galaxies have been identified as having an ultrasoft excess in addition to a large BLR velocity: 1H 0419-577 (Guainazzi et al., 1998; Turner et al., 1999; Page et al., 2001; Pounds et al., 2004) and RXJ0437.4-4711 (Halpern & Marshall, 1996; Wang et al., 1998). Do these comprise an intermediate class of object linking the Seyfert 1's with the NLS1's, or are they true Seyfert 1 galaxies seen with a particular observational bias? In a survey of AGN with *ASCA*, Brandt, Mathur & Elvis (1997) found that, in addition to steeper soft X-ray slopes, NLS1's generally have steeper hard X-ray continua than Seyfert 1's ($< \Gamma_{\rm NLS1} >= 2.15 \pm 0.049$, $< \Gamma_{\rm Sy1} >= 1.87 \pm 0.036$). RE J2248-511 has a 2 - 10 keV power law slope of $\Gamma = 1.84^{+0.06}_{-0.04}$, so in the hard X-ray regime RE J2248-511 resembles a normal Seyfert 1 far more than it does a NLS1.

The strength of the soft X-ray excess measured with *XMM-Newton* is typical of a Seyfert 1 (e.g. Turner & Pounds, 1989). The soft X-ray slope between 0.3 and 2 keV is also similar to that found in the PG bright quasar sample (Laor et al., 1997). In fact, this source also follows the observed correlation between Balmer linewidth and soft X-ray slope (Puchnarewicz et al., 1992; Laor et al., 1997) if the 'ultrasoft' part of the X-ray spectrum (below 0.25 keV) is not included. A comparison of the *XMM-Newton* spectrum of RE J2248-511 with that of the NLS1 galaxy RE 1034+396 is shown in Fig. 3.19, where it is clear that the soft excess in RE J2248-511 is significantly weaker than in the NLS1.

Variability in the soft X-ray excess is a property which RE J2248-511 shares with the NLS1 galaxies. But again these changes are generally more dramatic in NLS1 than I observe for this AGN. For example, the NLS1 galaxy 1H 0419-577 shows spectral variability in the soft component of up to a factor of 10 (Pounds et al., 2004 and references therein). 1H 0419-577 also changes 'state' in a similar

way to Galactic black hole binaries such that the power law slope is correlated with the strength of the soft X-ray excess. The analogy made between NLS1's like 1H 0419-577 and Galactic black hole binary systems cannot be made for RE J2248-511 as there is no change in the 2 - 10 keV power law between the *ASCA* and *XMM-Newton* observations, almost 5 years apart.

From observations of the 0.3 - 10 keV X-ray emission and its variability, and the optical emission lines, RE J2248-511 appears to be a typical Seyfert 1 galaxy. One conclusion which can be drawn from this is that observations of AGN in the EUV band are vital in order to understand the nature of the BBB and the discrimination between normal and narrow-line Seyfert 1's. In this case of RE J2248-511, far more can be learned from an EUV mission than a broad-band X-ray mission. The only 'unusual' property seen in RE J2248-511 is the strength and broad wavelength span of the BBB, which I find can be explained by a Comptonised accretion disc accreting at a high rate onto a typical black hole mass, where we are observing the system almost face-on. The BLR need not be at as large a radius, and therefore low velocities, as observed in NLS1's because the black hole mass is not lower than $2.3 \times 10^7\,\mathrm{M}_\odot$. The optical broad-line widths ($3700 - 4700$ km s^{-1}) are larger than those found in narrow-line Seyfert 1's. A face-on disc should be accompanied by observed optical linewidths which are at the low end of the Seyfert 1 range, or else require that the BLR is closer in than is typical.

3.10 Conclusions

The *XMM-Newton* observations of RE J2248-511 have shown further long-term variability in the soft X-ray spectrum, whilst the hard X-ray power law remains constant. The 0.3 - 2 keV soft X-ray excess is best fitted with 2 blackbodies, but is also adequately fit with a Comptonised component. The optical to soft X-ray big blue bump, as observed in October 2000, is consistent with a face-on Comptonised accretion disc, likely to be accreting at a high accretion rate onto a $10^{7.5}$ - $10^{8.5}\,\mathrm{M}_\odot$ black

hole. This accretion disc can account for the observed ultrasoft excess component. I propose that this source is intrinsically a normal Seyfert 1, but appears to share the ultrasoft X-ray excess properties of the narrow-line Seyfert 1's because it is observed at a lower inclination angle than the majority of Seyfert 1 galaxies.

Chapter 4

NGC 7213 and the Seyfert-LINER connection

NGC 7213 is a nearby ($z = 0.006$) Sa galaxy with AGN and LINER (low ionisation nuclear emission-line region; Heckman, 1980) characteristics. The AGN in this source is a Seyfert 1, classified as such from its Hα line width (full width at zero intensity ~ 13000 km s^{-1} Phillips, 1979; FWHM ~ 2000 km s^{-1} Filippenko & Halpern, 1984, hereafter FH84). LINER galaxies are characterised by optical emission line ratios which indicate a low level of ionisation. The origin of these emission lines is still the subject of debate: the lines are attributed either to shock heating (Baldwin, Phillips & Terlevich, 1981) or to photoionisation by a central AGN (Ferland & Netzer, 1983; Halpern & Steiner, 1983). Dopita & Sutherland (1996) have shown that shock heating can produce the optical line ratios observed in LINER galaxies, with shock velocities of 150 - 500 km s^{-1}. Shocks are created in our local Universe by stellar processes, observed for example in star forming regions, planetary nebulae and supernovae. Possible origins of a shock in an AGN include outflows such as a jet or a wind, or turbulent motion of material in the central regions. In contradiction, FH84 argue that photoionisation of clouds spanning a range of densities and velocities by a non-stellar continuum is more likely to be the mechanism creating

the optical line emission in the case of NGC 7213. By invoking high density rather than high temperature clouds, FH84 eliminate the need for shock heating. When the optical line ratios of LINERs were compared to those measured in Seyfert galaxies (Ferland & Netzer, 1983), the same photoionising continuum shape, but with a systematic variation of ionisation parameter from low values in LINERs to high values in Seyferts, was able to explain the data.

The position of the X-ray source H2209-471 discovered with *HEAO A-2* (Marshall et al., 1978) was found to coincide within the errors with the host galaxy of NGC 7213. Though the X-ray error box was large (0.6 x 2.8 deg) subsequent optical spectroscopy showed that a broad Hα emission line was present in the galaxy giving weight to the association of the two (Phillips, 1979). Since then this low luminosity X-ray source ($L_{\rm x} \sim 3{\times}10^{42}$ erg s^{-1}) has been observed by several missions. The continuum has a power law shape with a photon index typical of Seyfert galaxies but it has proven difficult to obtain more details about the spectrum with the previous X-ray satellites. *XMM-Newton*, and particularly its RGS instruments, provides us with a more detailed spectrum from which to learn about this source.

The presence of a soft X-ray excess in NGC 7213 was implied by the results of an *EXOSAT* spectral survey of AGN (Turner & Pounds, 1989) when the measured absorbing column for a single power law fit was found to be significantly lower than the Galactic value. In addition, the UV flux measured by Wu, Boggess & Gull (1983) was higher than would be expected from an extrapolation of the optical flux indicating a small big blue bump. The BBB is often interpreted as thermal emission from an accretion disc; the presence or absence of accretion discs in LINERs is an important question to address if we are to understand their underlying emission mechanisms.

Turner & Pounds (1989) and Pounds et al. (1994) reported possible Fe Kα emission in the X-ray spectrum, but there was not sufficient resolution to unambiguously detect these features. Recently Bianchi et al. (2003) combined data from the pn camera on *XMM-Newton* with data from the PDS and MECS instruments on *BeppoSAX*

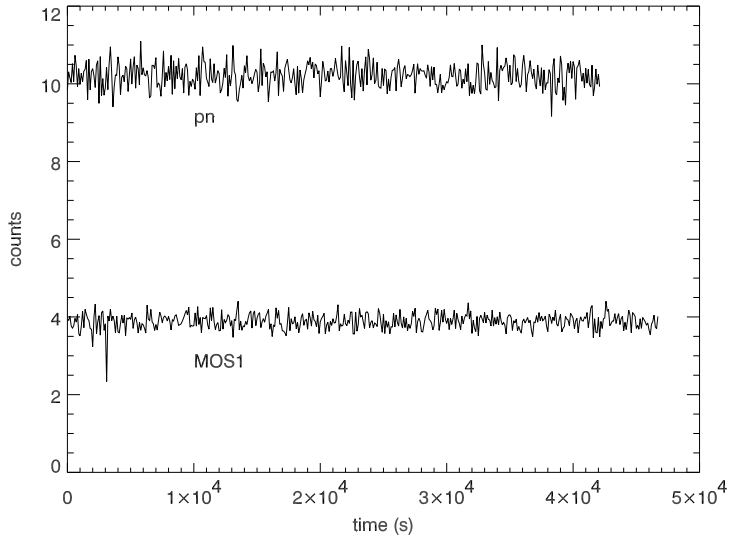

Figure 4.1: The lightcurves of the pn and MOS1 observations.

to investigate the iron line complex and reflection hump. They found that a neutral Fe Kα line is present, possibly with weaker emission lines from highly ionised iron. The reflection hump appears to be absent.

Here I present the *XMM-Newton* observation of NGC 7213 which includes broad-band and high-resolution X-ray spectra from the EPIC and RGS instruments and UV photometry from the Optical Monitor (OM). This work was done as part of a collaboration at MSSL led by myself. M. J. Page has reduced and modelled the RGS and OM data. All other data has been reduced and analysed by myself. Identifying the physical mechanisms producing the X-ray emission may provide some clues to the origin of the optical emission lines where at present neither shock heating nor photoionisation by the AGN can be ruled out. I discuss the contribution from the AGN to the nuclear emission and compare the X-ray spectral properties of NGC 7213 with those of the nearest LINER galaxy M 81 (Page et al., 2003; Page et al., 2004), which has also been studied in detail using *XMM-Newton*, and discuss the relationship between Seyfert galaxies and LINERs. This work is also presented in Starling et al. (2004).

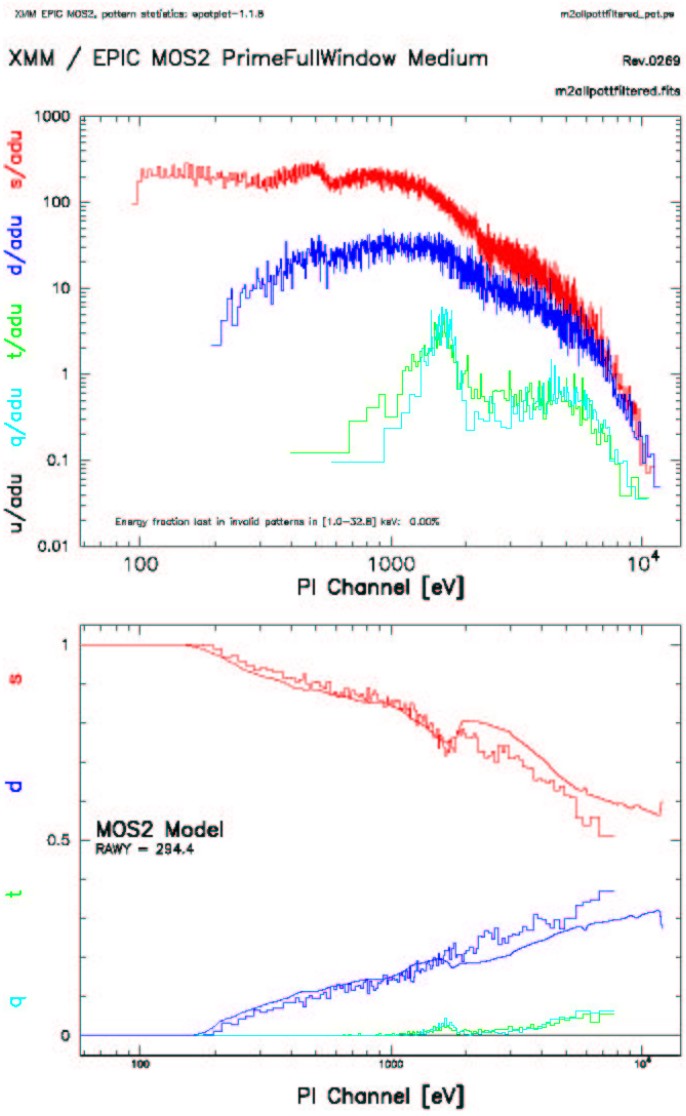

Figure 4.2: The upper panel shows the distribution of single, double, triple and quadruple events as a function of PI channel for the observation of NGC 7213 with the EPIC MOS2 camera in full frame mode. The lower panel shows the ratio of each event type to the sum of all events, together with the predicted ratio for a typical non-piled-up point source. The divergence of the single and double event curves in this panel signify pile-up. Plot produced using the SAS task epatplot.

4.1 XMM-Newton observations

NGC 7213 was observed on 2001 May 28/29 with *XMM-Newton* (Jansen et al., 2001) in the RGS Guaranteed Time Programme. The EPIC (Strüder et al., 2001; Turner et al., 2001) MOS1 and pn cameras were operated in small window mode with the medium filter. The EPIC MOS2 was in full frame mode (also medium filter) to image the entire galaxy. MOS2 is omitted from the analysis due to pile-up, since the count rate was over three times higher than the limit of 0.7 counts s^{-1} for point sources estimated in the *XMM-Newton* User Handbook (Ehle et al., 2003). This is demonstrated by divergence of the curves in the SAS epatplot routine and the output is shown in Fig. 4.2. The RGS instruments were in spectroscopy mode. The exposure times are 46448 s for MOS1, 42201 s for pn and 46716 s for each RGS instrument. No variability in flux was found during the observation, as is clear from the EPIC lightcurves shown in Fig. 4.1.

The raw EPIC data were processed with the *XMM-Newton* SAS version 5.4. Spectra were constructed using single and double events in the pn and all valid event patterns (0 - 12) in MOS1. Source counts were taken from a circular region of radius 45 arcsec. In MOS1 a background spectrum was obtained from a nearby source-free region, 7 times larger in radius than the source extraction region. For the pn the background spectrum was taken from 3 separate circular regions totalling 5.76 times the area of the source circle. The MOS1 and pn spectra were then combined into a single spectrum with 45 eV bins using the method of Page, Davis & Salvi (2003) to improve the signal to noise. The March 2003 EPIC response files for small window were used with the resulting spectra.

The RGS data were processed using the public release *XMM-Newton* SAS version 5.2 by M. J. Page. After background subtraction, the individual first and second order spectra from RGS1 and RGS2 were resampled and coadded to produce a single spectrum, and the response matrices were combined accordingly.

The OM (Mason et al., 2001) data were processed with *XMM-Newton* SAS ver-

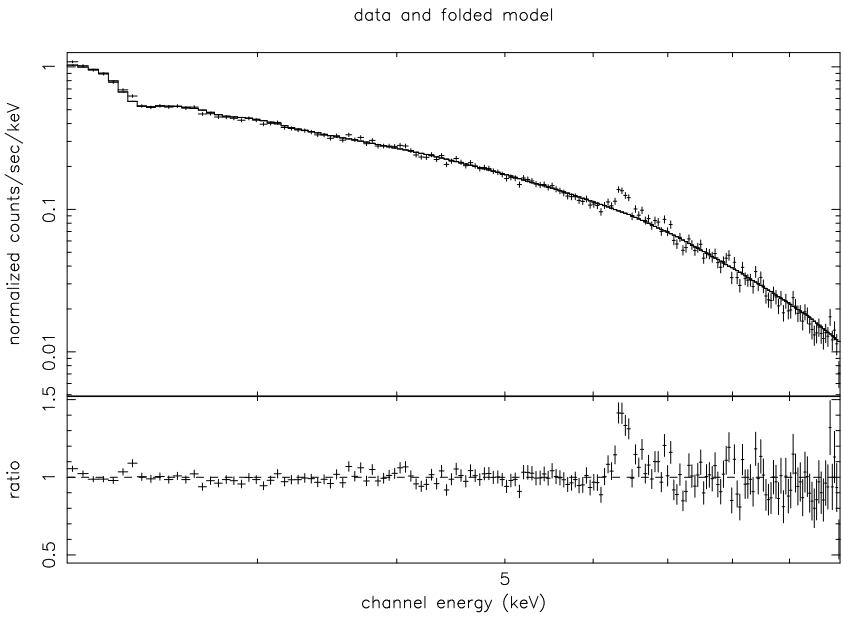

Figure 4.3: The top panel shows the 2 - 10 keV combined MOS1 and pn spectrum in the observers frame. The lower panel shows the data to model ratio with at least one clearly detected emission line.

sion 5.4 by M. J. Page. For each of the three UV filters the sub-exposures were coadded and corrected for modulo-8 noise. The total exposure times are 4000 s, 7200 s and 8000 s for the *UVW1*, *UVM2* and *UVW2* filters respectively. Photometry was performed on the nucleus using routines within IRAF, minimising the contribution of the host galaxy. The resultant magnitudes were then corrected for the fraction of the point-spread function falling outside the aperture, deadtime, coincidence loss, and Galactic reddening (Seaton, 1979).

4.2 Results

Spectral analysis of the data was done using the XSPEC v11.2 X-ray spectral fitting package, using the χ^2 minimization technique. The Galactic column value used throughout is $N_{\rm H} = 2.0 \times 10^{20}$ cm^{-2} (Dickey & Lockman, 1990), and all line energies are quoted in the rest frame of the source.

Table 4.1: Model fits to the 2 - 10 keV combined MOS1 and pn spectrum. The Galactic column is included in all fits. The source redshift is fixed at $z = 0.60$. R is the reflection fraction and ξ is the ionisation parameter. All errors are quoted at the 90% confidence level for 1 interesting parameter. All energies (E), line widths (σ) and equivalent widths (EW) are given in keV.

Model	Γ	R	ξ	norm/10^{-3}	E_1	σ_1	EW_1	E_2	EW_2	E_3	EW_3	χ^2/ν
PL	$1.70^{+0.20}_{-0.10}$	-	-	$5.61^{+0.11}_{-0.09}$	-	-	-	-	-	-	-	378/177
PL+gauss	1.72±0.01	-	-	$5.68^{+0.17}_{-0.08}$	$6.41^{+0.02}_{-0.03}$	$0.037^{+0.066}_{-0.037}$	92±15	-	-	-	-	237/172
PL+3 gaussians	1.73±0.01	-	-	$5.77^{+0.10}_{-0.11}$	$6.40^{+0.04}_{-0.01}$	$0^{+0.05}_{-0}$	85^{+14}_{-15}	$6.68^{+0.07}_{-0.05}$	23^{+10}_{-10}	$6.97^{+0.08}_{-0.08}$	25^{+12}_{-14}	219/170
pexrav+gauss	$1.76^{+0.05}_{-0.07}$	$1.18^{+0.69}_{-0.71}$		$5.88^{+0.34}_{-0.26}$	$6.40^{+0.04}_{-0.01}$	$0^{+0.05}_{-0}$	76^{+17}_{-15}	-	-	-	-	231/173
pexriv+gauss	$1.72^{+0.07}_{-0.08}$	$1.12^{+0.72}_{-0.78}$	$0^{+0.02}_{-0}$	$5.74^{+0.46}_{-0.34}$	$6.40^{+0.04}_{-0.01}$	$0^{+0.05}_{-0}$	75^{+20}_{-17}	-	-	-	-	228/169
pexrav+3 gauss	$1.72^{+0.03}_{-0.04}$	0.40±0.40	-	$5.68^{+0.22}_{-0.28}$	6.4 fixed	0 fixed	80^{+24}_{-32}	6.7 fixed	24^{+5}_{-19}	6.96 fixed	27^{+6}_{-24}	222/173

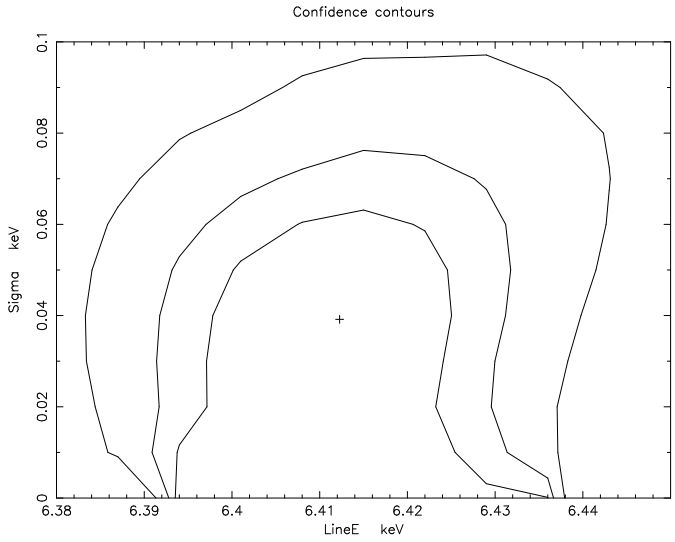

Figure 4.4: Contour plots of the 68%, 90% and 99% confidence contours for the centroid energy and width of the neutral Fe Kα emission line in the power law model.

4.2.1 The EPIC data

I consider first the 2 - 10 keV EPIC spectrum since the soft X-ray region is covered by the RGS instruments at much higher resolution. Initially I fitted a power law with Galactic absorption, typical of AGN medium energy X-ray spectra. The best fit has a power law photon index of $\Gamma = 1.70^{+0.20}_{-0.10}$, but again the single power law fit is very poor (χ^2/dof = 378/177, Fig. 4.3). The fitted parameters for this and all other models are listed in Table 4.1. Addition of a narrow ($\sigma < 0.066$) Gaussian line with best fitting energy $6.41^{+0.02}_{-0.03}$ keV (Fig. 4.4) improves the χ^2 statistic, but still does not provide a good fit to the data (the fit is rejected at $> 99.9\%$ confidence). The centroid energy of the line is consistent with iron fluorescence in matter in low ionisation states. The line has an equivalent width of 91.7 $\pm$ 15.3 eV and a flux of 2.16×10^{-13} erg cm^{-2} s^{-1}, $\sim$ 1% of the power law continuum flux over the 2 - 10 keV range. However, there remain residuals between 6.5 and 7 keV, so I test for the

presence either of further emission lines, reflection or a combination of both.

Firstly I assumed the excess emission is due to highly ionised iron lines. Adding narrow ($\sigma = 0$) Gaussians at energies $\sim$ 6.7 and $\sim$ 6.96 keV, corresponding to Fe XXV, and $\sim$ 6.96 keV, corresponding to Fe XXVI, gives an acceptable fit to the data (χ^2/dof = 219/170). The equivalent widths of these emission lines are 23$\pm$10 and 25^{+12}_{-14} eV respectively. I then considered models in which the excess emission is produced by reflection of the power law off either a neutral or an ionised medium (pexrav and pexriv models in XSPEC respectively, Magdziarz & Zdziarski, 1995). When fitting the reflection models I fixed the power law fold energy at 100 keV, $\cos i$ = 0.45 and assumed solar abundances. The neutral reflector model (pexrav+gauss) gives an acceptable fit (χ^2/dof = 231/173), though not quite as good a fit as the 3-emission-line model. Using an ionised reflector, with its temperature fixed at $T = 30000$ K, the best-fitting ionisation parameter was consistent with zero and the other fitted parameters iterated to very similar values to the pexrav neutral reflector model. Therefore I will consider only neutral reflection from here onwards.

To assess whether both reflection and 6.7 and 6.96 keV iron emission are required I fitted a model with a neutral reflector plus 3 narrow emission lines. To maximise the degrees of freedom in the fit I fixed the width, σ, of all three emission lines to zero, and fixed their energies to those of Fe I, Fe XXV and Fe XXVI. The parameters of this model fit remain generally consistent with the PL+3-emission-line model and results in a reflection fraction of 0.4$\pm$0.4 (Table 4.1), i.e. when the emission lines are included the reflection fraction is consistent with zero. The 2 - 10 keV flux of each model is approximately 2.2×10^{-11} erg cm^{-2} s^{-1}, corresponding to a luminosity of 1.7×10^{42} erg s^{-1} (for $H_0 = 70$ km s^{-1} Mpc^{-1}).

4.2.2 The RGS data

The RGS spectrum of NGC 7213 is dominated by continuum emission, but shows emission lines, particularly from O VII and O VIII. No significant absorption lines

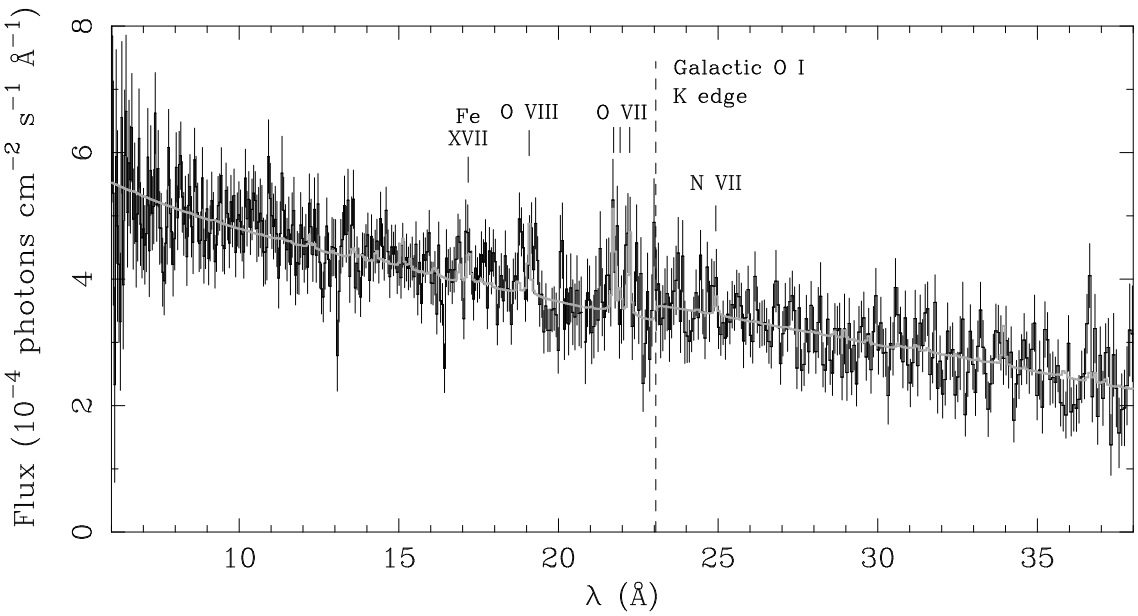

Figure 4.5: The RGS spectrum of NGC 7213 (datapoints) compared to a model consisting of a power law and 2 temperature thermal plasma (red line). The positions of prominent emission lines are marked as well as the O I K edge from the Galactic interstellar medium. Courtesy M. J. Page.

Table 4.2: Model fits to the RGS spectrum (M. J. Page).

Model	Γ	PL norm/10^{-3}	kT	MEKAL norm/10^{-3}	χ^2/dof
PL	$1.77^{+0.02}_{-0.02}$	$5.88^{+0.06}_{-0.06}$			586/498
PL+ MEKAL	$1.76^{+0.02}_{-0.02}$	$5.85^{+0.06}_{-0.06}$	$0.18^{+0.03}_{-0.01}$	$0.086^{+3.4}_{-2.6}$	554/496
PL+2×MEKAL	$1.76^{+0.02}_{-0.02}$	$5.80^{+0.07}_{-0.06}$	$0.18^{+0.02}_{-0.03}$, $0.56^{+0.16}_{-0.22}$	$0.086^{+3.4}_{-3.0}$, $0.039^{+2.1}_{-2.4}$	546/494

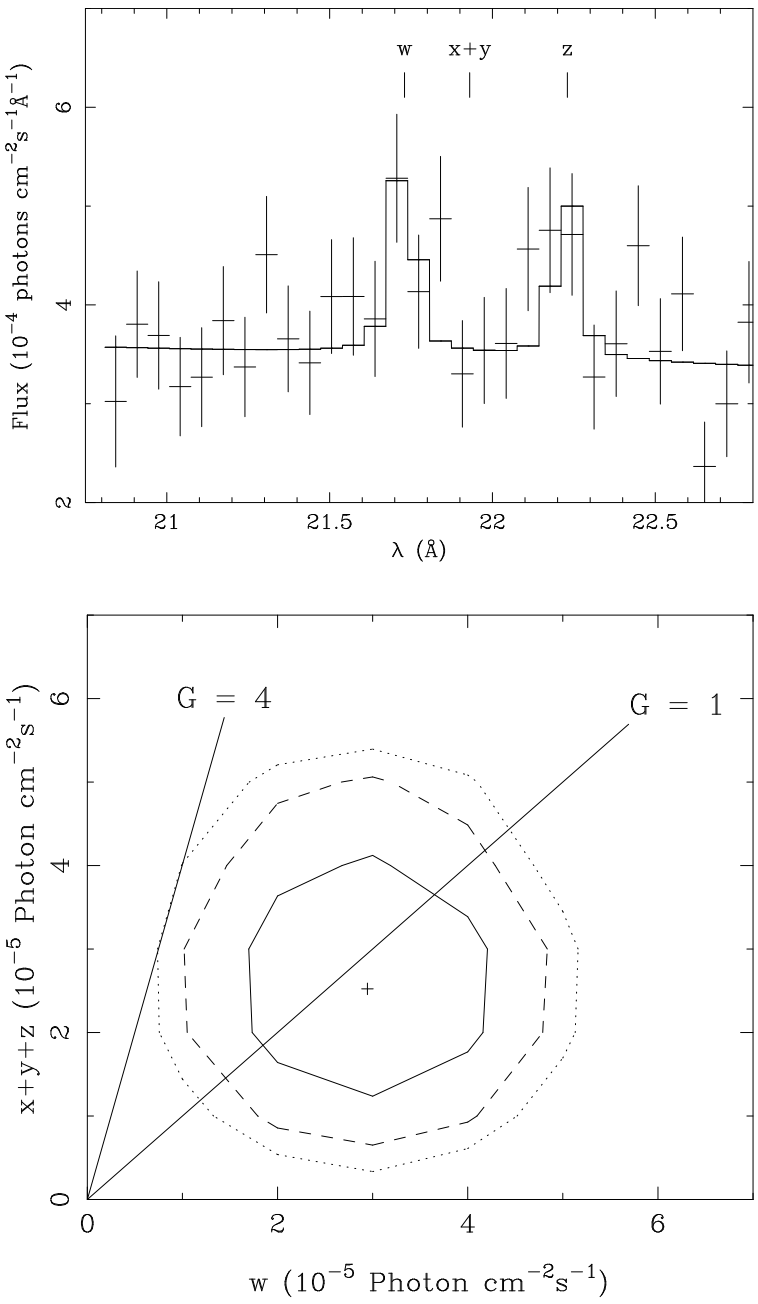

Figure 4.6: Top panel: close up of the He-like O VII triplet in the RGS spectrum with best fitting power law plus 3-Gaussian model. Bottom panel: confidence interval on the strength of the forbidden and intercombination lines (x+y+z) against the resonance line (w). The solid, dashed and dotted contours correspond to 68%, 90% and 95% respectively for two interesting parameters. The line $G = 1$ indicates the ratio expected for collisionally ionised plasma, while a photoionised plasma should lie to the left of the $G = 4$ line. Courtesy M. J. Page.

nor broad absorption features such as unresolved transition arrays (UTAs, Behar, Sako & Kahn, 2001) are observed. The line-like absorption features at 13.08 Å and 16.43 Å in Fig. 4.5 are low signal to noise data points coincident with chip-gaps in the first order spectra. The RGS spectrum has been modelled with a power law and Galactic absorption plus thermal plasma components (the MEKAL model in XSPEC). All the fitting results are given in Table 4.2. The best fitting model is that of a power law with index $\Gamma = 1.77 \pm 0.02$ (similar to that found using the EPIC data, see Tables 4.1 and 4.2) plus a single thermal plasma component at a temperature of $kT = 0.18^{+0.02}_{-0.01}$ keV. There is no significant blackbody-like soft excess emission above the power law. The best-fitting model is overlaid on the data in Fig. 4.5.

The emission lines could come from gas which is either photoionised or collisionally ionised, and the two cases can be discriminated by the 'G' ratio of the resonance (w) to intercombination (x+y) and forbidden (z) line strengths in the He-like triplet of O VII (Porquet & Dubau, 2000). The G ratio for NGC 7213 was measured from fits to the RGS spectrum in the 21 - 23 Å range with a power law and 3 emission lines, with energies fixed to the rest frame energies of the O VII triplet. The best fit is shown in the top panel of Fig. 4.6 and the bottom panel shows the 68, 90 and 95% confidence contours for w and x+y+z. $G \approx 1$ is expected for a collisionally ionised plasma, fully consistent with that observed in NGC 7213. Photoionisation dominated plasmas have $G \geq 4$, which is excluded at $> 95\%$ confidence here. $G < 4$ can be observed for a photoionised plasma which lies out of the line-of-sight, if the resonance line is enhanced by photoexcitation (Coupé et al., 2004). However, the $3d - 2p$ lines of Fe XVII at $\sim$15 Å should also be enhanced relative to the $3s - 2p$ lines at $\sim$17 Å, as is observed in NGC 1068 (Kinkhabwala et al., 2002) and Mrk 3 (Sako et al., 2000). This is not seen in NGC 7213, and so I can assume that the emission lines in the RGS spectrum are from collisionally ionised gas.

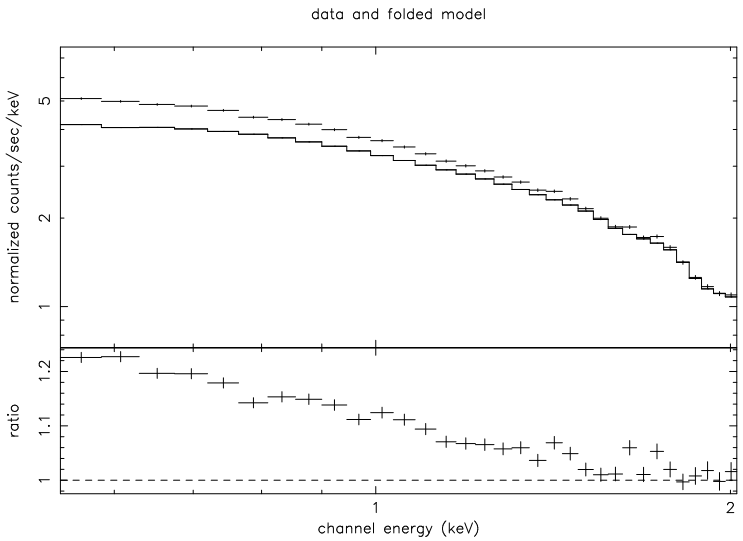

Figure 4.7: Upper panel: EPIC soft X-ray spectrum and best-fitting model to the RGS data. Lower panel: data to model ratio.

4.2.3 The EPIC soft X-ray data

Having found that a power law (consistent with the hard X-ray power law) plus mekal component is a good fit to the 0.5-2 keV RGS data, I fitted the same model to the 0.3-2 keV combined pn and MOS1 EPIC spectrum. The fit is poor (χ^2/dof = 8865/33) because the continuum slope is steeper than that of the model, with a data:model ratio of $\leq$1.3 (Fig. 4.7). Keeping the single MEKAL component as fitted to the RGS data I still need to increase the power law slope to 1.950$\pm$0.006 and normalisation to 6.56$\pm$0.02 $\times$ 10^{-3} photons cm^{-2} s^{-1} to obtain an acceptable fit to the 0.3-2 keV EPIC spectrum with χ^2/dof = 60/35. The continuum in this range is not a blackbody-like shape as is common for a soft X-ray excess, but can be adequately modelled by a single power law plus Galactic absorption. However, I hesitate to draw strong conclusions from this result since cross calibration of the three instruments is not yet accurately known. The MOS/pn cross correlation agrees to within 10% from energies of 0.4 keV upwards and EPIC and RGS appear to agree in normalisation to $\pm$20%, with the EPIC having a significantly steeper slope than the RGS in individual fits (Kirsch, 2003).

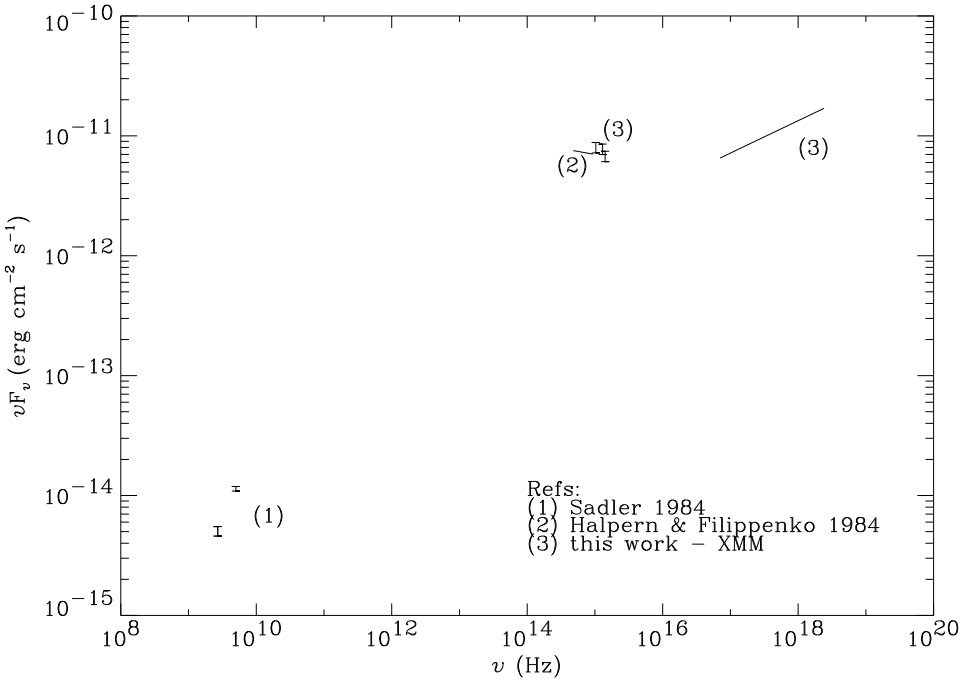

Figure 4.8: The AGN radio to X-ray continuum spectral energy distribution for NGC 7213. The optical extinction is assumed to be $A_v = 0.05$, taken from (2). Note the data are not simultaneous measurements.

So the soft X-ray spectrum of this AGN appears to show some curvature, gradually steepening towards lower energies in the EPIC spectrum, as noted by Bianchi et al. (2003). However, the difference between the RGS and EPIC soft X-ray spectra is consistent with the existing cross-calibration uncertainties, and there does not appear to be any sign of a blackbody soft excess component in the RGS or in the EPIC spectrum.

4.3 Discussion

The *XMM-Newton* spectra are dominated by continuum emission, which is well fitted with a $\Gamma \sim 1.8$ power law consistent with previous studies (Turner & Pounds, 1989, *EXOSAT*; Pounds et al., 1994, *Ginga* and *ROSAT*). In addition, a thermal

plasma with a temperature of $0.18^{+0.03}_{-0.01}$ keV contributes line emission in the soft X-rays, while at higher energy Kα lines are seen from cold iron, Fe XXV and Fe XXVI.

4.3.1 Comparison with Seyfert and LINER galaxies

The 2 - 10 keV spectrum of NGC 7213 closely resembles a typical Seyfert galaxy, as it is dominated by a $\Gamma = 1.7$ power law and a 6.4 keV Fe Kα emission line. The Fe Kα emission line is narrow ($\sigma < 0.066$), so it cannot originate in the inner parts of an accretion disc. I do not require a reflection component when fitting the combined MOS1 and pn spectrum, which is consistent with a broad-band study by Bianchi et al., (2003) in which a Compton reflection hump above 10 keV was not detected in the *BeppoSAX* data. Bianchi et al. (2003) concluded that, given the apparent absence of a reflection component, the neutral Fe Kα emission must arise from Compton thin material out of our line-of-sight, either in the form of a torus with a column density of $N_{\rm H} \sim 2 \times 10^{23}$ cm^{-2} or it is the broad-line region. The resolution of the pn camera does not allow the two to be distinguished. The 2 - 10 keV spectrum of NGC 7213 differs from that typically observed in Seyferts in that it contains significant emission lines from Fe XXV and Fe XXVI, whereas these lines are not normally observed in the classical luminous Seyfert galaxies (e.g. NGC 3783, Kaspi et al., 2002; NGC 5548, Pounds et al., 2003; NGC 7469, Blustin et al., 2003). In contrast, these lines appear to be strong in the nearby LINER M 81 (Page et al., 2004).

In the soft X-ray regime NGC 7213 departs further from a Seyfert-like spectrum since collisionally ionised plasmas at soft X-ray temperatures are not generally found in the spectra of Seyferts. Soft X-ray emitting and absorbing plasmas in Seyfert galaxies appear to be photoionised. This is true whether the ionised gas is seen in emission or absorption (e.g. IRAS 13349+2438, Sako et al., 2001; NGC 1068, Kinkhabwala et al., 2002; NGC 3783, Kaspi et al., 2002). However, in the RGS

spectrum of NGC 7213 I do not find any evidence for photoionised absorption. Therefore we are not viewing NGC 7213 through a warm absorber, and the emission lines are collisionally ionised rather than photoionised (Fig. 4.6).

Amongst AGN, collisionally ionised thermal plasma at soft X-ray temperatures, as observed in NGC 7213, may be a property specific to LINERs. In a study of 21 LINERs observed by *ASCA* most were well fitted with a hard X-ray power law ($\Gamma \sim 1.8$) plus a soft X-ray thermal plasma component with $kT < 1$ keV (Terashima et al., 2002). While this provides strong evidence for the presence of a soft X-ray emission line component in LINERs, the resolution of *ASCA* was not good enough to permit diagnostics which could distinguish between collisionally ionised and photoionised plasma. However, the very nearby LINER galaxy M 81, for which there is a long-duration RGS spectrum, does contain a significant component of soft X-ray collisionally-ionised thermal plasma (Page et al., 2003).

The *XMM-Newton* spectrum of NGC 7213 also deviates from that of a typical Seyfert in that it has little or no blackbody-like soft X-ray excess emission. This component is found in the X-ray spectra of most Seyferts (Turner & Pounds, 1989), the strongest being seen in the Narrow-line Seyfert 1 galaxies (NLS1s). The origin of the soft X-ray excess is unknown, but is often interpreted as the high energy tail of an accretion disc (Turner & Pounds, 1989), particularly in NLS1s (e.g. RE 1034+39, Pounds, Done & Osborne, 1995). Whatever the physical mechanism producing the soft excess, it is not operating in NGC 7213.

4.3.2 Evidence for an accretion disc

Many Seyfert galaxies show strong evidence in X-rays for an accretion disc surrounding the black hole. The main indicators are a soft excess, reflection, and broad Fe Kα line emission, all of which come from the inner parts of the accretion disc. None of these indicators are present in the *XMM-Newton* spectra of NGC 7213. Therefore it is likely that if there is an accretion disc in NGC 7213, the inner edge of the

disc is truncated at a larger radius than is typical in Seyfert galaxies. Evidence for such a disc must be sought at longer wavelengths where the thermal disc emission is expected to peak.

The UV bump

The UV bump in NGC 7213 is either absent or extremely weak compared to other Seyferts (Wu, Boggess & Gull, 1983). The optical continuum emission of NGC 7213 comprises both non thermal emission from the AGN and stellar radiation (Halpern & Filippenko, 1984, hereafter HF84). A decomposition of the spectrum, assuming a power law for the AGN contribution following $F \propto \nu^{-1.1}$, shows that more than 50% of the total continuum emission at 3300 Å can be non-stellar. The actual flux level is uncertain by $\pm 30\%$ and also depends on the visual extinction adopted. HF84 argue that the optical extinction is much higher than the Galactic value. However the *XMM-Newton* data show no evidence for any intrinsic absorption of the X-ray flux. Therefore I have adopted the AGN power law component of the HF84 optical spectrum decomposition, assuming only Galactic absorption. The nuclear spectral energy distribution of NGC 7213 is shown in Fig. 4.8. The ultraviolet data from the OM are in good agreement with an extrapolation of the optical power law to shorter wavelengths. There is no evidence for a significant optical/UV bump and consequently the AGN bolometric luminosity does not appear to be dominated by emission from an optically-thick, geometrically-thin accretion disc.

ADAF models and quiescent accretion discs

Assuming that NGC 7213 does contain an accretion disc, there are two possible explanations for the lack of UV emission. Either the disc does not extend close enough to the black hole to emit significantly in the optical/UV, or the disc extends close to the black hole but has such a low mass transfer rate that it contributes little to the overall emission.

Starting with the truncated inner-disc explanation, it is known that at low accretion rates, stable accretion flows can exist in which the inner parts of the disc take the form of an optically-thin, tenuous, hot corona. In this case the soft X-ray and UV signatures of thermal disc emission are weak or absent because the geometrically thin, optically thick part of the disc does not extend close enough to the black hole. Because the inner, hot corona is a much less efficient radiator than a thin disc, much of the energy is advected into the black hole rather than being radiated. There are a number of these type of models, stemming from the model known as an advection-dominated accretion flow (ADAF, Narayan & Yi, 1995). A truncated inner disc plus ADAF is the configuration proposed to explain the spectra of black hole X-ray binaries (Esin et al., 1998; Esin, McClintock & Narayan, 1997; Narayan, Garcia & McClintock, 1997). The quiescent phase of the soft X-ray transients V404 Cyg and A0620-00 can be explained with the ADAF model, where the inner radius of the accretion disc lies at $\sim 10^4$ Schwarzschild radii (Narayan, Barret & McClintock, 1997). To explain optical and UV observations of M 81, Quataert et al., (1999) invoke an ADAF within the truncation radius of the disc. An ADAF model has also been successfully applied to describe the multiwavelength emission from the Galactic Centre (Narayan et al., 1998).

The alternative to a truncated inner disc plus ADAF is a disc which extends to the inner regions but which is in a 'low state'; this can also account for the lack of disc emission from NGC7213. Thermal-viscous ionisation instabilities, which can develop in a partial ionisation zone of an AGN accretion disc, can cause the disc to oscillate between high (bright) states and low (faint) states (Siemiginowska, Czerny & Kostyunin, 1996). The disc spends most of the time in the low state with low luminosity, peaking in the IR and emitting negligible optical and UV radiation. This is analagous to the instability which drives outbursts in cataclysmic variables. However, although a low-state disc can account for the lack of primary disc emission, it ought to constitute an X-ray reflector subtending a substantial solid angle to the X-ray source. I do not detect any significant X-ray reflection from NGC 7213, and

therefore the low-state disc model is less consistent with the observational data than the ADAF model.

4.3.3 Accretion rate and black hole mass

The ADAF model, which could explain may of the observational properties of NGC 7213, is only appropriate at low accretion rates (a few percent of the Eddington rate or less, Narayan & Yi, 1995). The alternative of a 'low state' disc would also imply a significantly sub-Eddington accretion rate. To investigate the accretion rate in NGC 7213 I have estimated the bolometric luminosity of the active nucleus by integrating the radio to X-ray spectral energy distribution, using radio measurements from Sadler (1984), a power law component in the optical, deconvolved from the stellar contribution by HF84, and the *XMM-Newton* X-ray spectrum. The bolometric luminosity thus obtained is approximately $9{\times}10^{42}$ erg s^{-1}. Previous estimates of the bolometric luminosity are significantly higher than my determination: $L_{\rm Bol} = 10^{44.3}$ erg s^{-1} (Woo & Urry, 2002) and $L_{\rm Bol} = 10^{44.1}$ erg s^{-1} (Padovani & Rafanelli, 1988). However, these values include the host galaxy as well as the AGN, so overestimate the AGN luminosity by a considerable amount. The black hole mass has been estimated from the stellar velocity dispersion by Nelson & Whittle (1995), who obtained $M_{\rm BH} = 10^{8.0}\,{\rm M}_{\odot}$. Such a high black hole mass is consistent with the observed lack of significant X-ray variability during the 46 ks *XMM-Newton* observation. Combining the bolometric luminosity and mass estimates I find that the luminosity of NGC 7213 is approximately 7 $\times 10^{-4} L_{\rm Edd}$. Generally, Seyfert accretion rates lie in the range 0.001 - 1 $L_{\rm Edd}$ (Wandel, 1999). Padovani & Rafanelli (1988) found an average accretion rate of $\sim 0.2\dot{M}_{\rm Edd}$ for the 34 local Seyfert 1 galaxies within their sample of AGN. However, a much lower rate of ~ 0.005 $L_{\rm Edd}$ is inferred for local type 1 Seyfert galaxies from studies of their X-ray luminosity function (Page, 2001). In any case, my accretion rate estimate for NGC 7213 lies at or below the low end of the distribution of Seyfert accretion rates.

The low luminosity AGN which are found in LINER galaxies may be typified by lower accretion rates than Seyferts. M 81, the nearest known LINER, accretes at $<$ 0.001 times its Eddington rate (Ho, 1999), while an accretion rate of $10^{-4}\dot{M}_{\rm Edd}$ was determined for the LINER NGC 4203 (Shields et al., 2000).

4.3.4 Comparison of the X-ray spectrum with M 81

An interesting comparison can be made between X-ray spectra of NGC 7213 and M 81, since M 81 is the nearest LINER galaxy and has been studied in detail using *XMM-Newton* (Page et al., 2003; Page et al., 2004). The broad-band X-ray spectra of these two galaxies, at first glance, look remarkably similar, but whilst the continua are comparable I find substantial differences in the emission line parameters. The soft X-ray emission lines are less prominent in NGC 7213 than in M 81, and the emission from thermal plasma components in NGC 7213 comprises a much smaller fraction of the total 0.3 - 10 keV flux than in M 81 (0.3%, compared with 8.7% in M 81). These emission lines are not normally observed in Seyfert galaxies. On the other hand the Fe I Kα line at 6.4 keV is commonly found in Seyferts (Nandra et al., 1997), and the equivalent width of this line is about twice as large in NGC 7213 as it is in M 81. Therefore, although NGC 7213 contains the soft X-ray emission lines and Fe Kα lines of Fe XXV and Fe XXVI that are not usually observed in Seyfert galaxies but are seen in the LINER galaxy M 81, the relative weakness of these lines and the strength of Fe I Kα in NGC 7213 make the X-ray spectrum of NGC 7213 much more Seyfert-like than that of M 81. Therefore NGC 7213 appears to bridge the gap between 'normal' Seyfert galaxies and LINER galaxies such as M 81.

4.3.5 The Seyfert–LINER connection and beyond

It is likely then, that there is a continuous distribution of galaxy nuclei between the LINERs and 'normal' Seyfert nuclei, over which the X-ray spectral features characteristic of Seyferts such as the neutral Fe Kα line, become successively more

prominent, while the features characteristic of LINERs such as soft X-ray emission lines diminish in significance. Accretion rate onto the black hole with respect to the Eddington rate is likely to be the overriding factor, with LINER galaxies accreting at much lower rates than Seyfert galaxies (Ho, Filippenko & Sargent, 2003) and containing ADAFs. In fact, looking at the observational properties of the Galactic Centre I find that it may also fit into this continuous distribution, at the opposite end of the scale to the Seyferts. The Galactic Centre contains a low-mass black hole with an extremely low accretion rate ($< 1 \times 10^{-6}$ Eddington, Falcke & Biermann, 1999; Quataert, Narayan & Reid, 1999). The emission from this region comes predominantly from thermal plasmas with strong soft X-ray emission (Baganoff et al., 2003). At higher energies Fe Kα emission is observed (Tanaka et al., 2000), the strongest line being at 6.7 keV. Therefore, the Galactic Centre begins the sequence: its characteristics being a very low accretion rate, dominance of thermal plasma emission and strong highly ionised iron emission.

The lack of reflection in NGC 7213 may provide a clue to the explanation of the low accretion rates in LINER galaxies. Although there is a significant 6.4 keV line, the lack of reflection implies that this must arise in Compton-thin material. Thus the central region of NGC 7213 appears to be deficient in the dense, cool material that usually gives rise to reflection in Seyferts. In M 81, which has an even lower accretion rate than NGC 7213, the 6.4 keV line is only half as strong as it is in NGC 7213, implying that the central regions of M 81 are even more lacking in cool material than NGC 7213. That LINERs have gas-poor central regions relative to Seyferts has also been proposed by Ho, Filippenko & Sargent (2003) on the basis of their optical emission line properties. It therefore appears that the low accretion rates of LINER-AGN are a consequence of the shortage of material in their central regions. In this case LINERs are simply fuel-starved AGN, and could represent the weak, but not yet silent remnants that have evolved from a previous generation of Seyferts and QSOs.

4.4 Conclusions

I have presented an *XMM-Newton* observation of the LINER galaxy NGC 7213 obtaining both broad band and high resolution spectra. The spectrum shows a strong signature of a Seyfert 1 from the underlying power law and a neutral/low ionisation Fe Kα emission line. I also detect emission from Fe XXV and Fe XXVI Kα but no X-ray reflection. I do not find a blackbody-like soft X-ray excess component. I calculate an accretion rate for NGC 7213 of 7×10^{-4} times the Eddington limit from its published black hole mass and bolometric luminosity, though the evidence for an accretion disc in this system is sparse. In addition, a thermal plasma of temperature $0.18^{+0.03}_{-0.01}$ keV is required in the soft X-ray region where several low ionisation emission lines are detected. I suggest that this low ionisation thermal plasma may be a LINER characteristic.

The nuclear radiation at X-ray wavelengths is substantially more Seyfert-like than the AGN component in the nearby LINER galaxy M 81, meaning NGC 7213 has the properties of a galaxy somewhere in between a typical Seyfert 1 and a LINER galaxy. This supports the notion of continuity between the LINER and Seyfert classes, dictated by the luminosity of the central AGN and its mass accretion rate, both increasing from LINERs to Seyferts. In turn, the accretion rates appear to depend critically on the amount of material present in the central regions surrounding the AGN. This continuous distribution can be extended to include the Galactic Centre, which shares some properties with LINER galaxies.

Chapter 5

Conclusions

In this thesis I have investigated a number of the observational manifestations of accretion discs to provide further insight into the role of accretion in AGN.

I have made the first estimate of the alpha viscosity parameter for a complete sample of AGN, through studying their optical variability. Observational constraints on the viscosity parameter for AGN accretion discs are severely lacking, partly because the spectrum is not strongly affected by the viscosity, but also because the underlying viscosity mechanism is not known and only a parametrisation is possible. Based on the methods of Siemiginowska & Czerny (1989) I derive constraints on the viscosity parameter of $0.01 \leq \alpha \leq 0.03$, providing the tightest limits ever obtained from observations. This result is highly model-dependent and I have used simple accretion disc models, but is the first step in fulfilling the need for observational tests of model predictions for the viscosity parameter.

While the temporal variability of AGN can be used to probe the accretion disc viscosity, the disc spectrum provides information on the accretion rate, inclination and central black hole mass. The thermal spectrum of an AGN accretion disc typically peaks in the optical-UV. However, a steepening towards low energies in the soft X-ray band (the soft X-ray excess) is often observed, and is particularly steep in the narrow-line Seyfert 1 galaxies and a small number of Seyfert 1 galaxies. In Comptonised accretion discs electron scattering is important and means that

the inner disc is hot enough to radiate in X-rays and form a soft X-ray excess. In analysing the optical to X-ray spectral energy distribution of one such Seyfert 1 galaxy, RE J2248-511, I have found that Comptonised accretion discs (Czerny & Elvis, 1987) with very low inclination angles ($\cos i > 0.75$), and favouring high accretion rates ($\dot{M} > 0.4\dot{M}_{\rm Edd}$) and large black hole masses ($10^{7.5} \leq M/\,{\rm M}_{\odot} \leq 10^{8.5}$) are consistent with the SED. Such a disc is able to form the part of the soft X-ray excess below 0.3 keV present in the *ROSAT* observation. The black hole mass estimated from these disc models is in agreement with the independent estimate I made using the photoionisation method which depends, observationally, only on the velocity of the broad-line region. Therefore, I find that it is not necessary to have a small black hole mass ($M \leq$ few $\times\, 10^6\,{\rm M}_{\odot}$) in order to form a strong soft X-ray excess, as has been implied by studies of narrow-line Seyfert 1 galaxies (e.g. Pounds, Done & Osborne, 1995). Though this source has some observed properties characteristic of 'normal' Seyfert 1's while some of its properties are more typical of narrow-line Seyfert 1's, I suggest that we are looking at a normal Seyfert 1 galaxy whose accretion disc is simply closer to face-on than the average Seyfert 1 galaxy and is accreting at a reasonably high rate. The big blue bump in RE J2248-511 can be one single component of thermal emission from a Comptonised disc, spanning 3 decades in frequency. There is no significant variability in the optical flux on timescales of days, nor in the X-ray flux over 1 year. However, there is evidence for substantial changes in the soft X-ray spectral shape and flux on longer timescales, over which 3 different strengths of the soft X-ray excess are observed. State changes are clearly observed in accreting binary systems, associated with different rates of accretion and disc sizes, and the narrow-line Seyfert 1's have been compared to the 'soft' state of stellar mass black hole binary star systems. This cannot be the cause of the X-ray variability here, since I have established that the majority of the soft excess emission in RE J2248-511 does not originate in an accretion disc. Variability of the big blue bump can only be studied with further simultaneous optical and X-ray observations like those presented in this thesis.

Accretion rate is a fundamental parameter of AGN since all active galaxies are powered by accretion. But do less luminous AGN have lower accretion rates or are they more heavily obscured? From consideration of the spectral energy distribution of the low ionisation nuclear emission-line region (LINER) galaxy NGC 7213, I have shown that the low luminosity AGN in the nucleus of this galaxy does have a low accretion rate. Accretion rates of AGN within LINER galaxies are generally lower than those of Seyfert galaxies, and an even lower accretion rate has been measured in the Galactic Centre. I propose that LINER-AGN and the very weak AGN in our Galactic Centre are not intrinsically different from Seyferts. Instead, there is likely a sequence from the Galactic centre through LINERs to Seyferts based on accretion rate. The low accretion rates of the Galactic Centre and LINER-AGN are a result of a lack of material in the inner regions able to accrete via the disc. This sequence is evident from AGN optical line spectra (Ho, Filippenko & Sargent, 2003), but I have shown that this can also be seen in their X-ray spectra in several ways. The relative amount of collisionally ionised gas detected in soft X-rays decreases between the LINER-AGN and Seyferts, whilst the strength of the neutral Fe Kα emission line with respect to ionised iron emission decreases. The accretion rate is controlled by the AGN local environment, which in LINERs is gas-poor compared with Seyfert nuclei.

The results of this thesis would fit in with the notion of a core structure for all AGN. Chapter 4 has shown that the Galactic Centre AGN, LINER-AGN and Seyferts may all be part of a continuous sequence determined by the accretion rate, which is regulated, in turn, by the nuclear environment. Similar black hole masses (within a decade) for 42 Palomar-Green Sample AGN are inferred from comparison of their optical lightcurves with numerical simulations in Chapter 2. The fact that a number of AGN appear to cross the current boundaries of two or more classifications, as discussed for the Seyfert galaxy RE J2248-511 in Chapter 3, suggests that some form of unified model based on observational bias may be reasonable.

This thesis has provided an observational study of central engines in AGN, con-

centrating on continuum emission at optical and X-ray wavelengths. The main aim throughout has been to look at the role of accretion discs and their parameters in a wide range of AGN types. I have addressed this by taking a multiwavelength approach, using several methods to estimate accretion disc parameters and thereby investigate the link between various types of AGN.

5.1 Future directions

The method used here to estimate the viscosity parameter for a sample of AGN could, in principle, also be used on the optical data of Galactic binary systems. In the case of cataclysmic variables (CVs) the large amplitude outbursts are modelled by thermal-viscous instabilities due to hydrogen ionisation and the viscosity parameter can be measured within the full instability cycle. In AGN we are not able to see the hydrogen ionisation instability variations because they are on too long a timescale and the observed variability in AGN must be caused by instabilities in the central regions, which are radiation-pressure dominated. So it would be the shorter variations - quasi-periodic oscillations or flickering for example - which might be the corresponding optical fluctuations. Making sure the right comparison timescales and disc regions are used will be crucial in this study. However, Galactic binary systems are much better understood than AGN, since observations of these relatively close-by sources generally provide more information. Estimating the value of the α-parameter for CVs may prove to be something of a test for this method and its assumptions.

The multiwavelength analyses of RE J2248-511 have shown that the optical and soft X-ray continua are varying in slope in a similar fashion. Without simultaneous data it is impossible to see if these changes are coincident in time. However, an optical spectrum taken with a blue grating and concurrent with the October 2001 *XMM-Newton* observation is now available. The relationship between the X-ray and optical emitting components could also be further investigated using simulations. Software such as the CLOUDY photoionisation simulation package (Ferland et al., 1998) can be used to simulate the optical broad-line spectra with various ionising continua.

Variability in the X-ray spectra of narrow-line Seyfert 1 galaxies has led to an analogy between these AGN and Galactic black hole binary systems. It may also be possible to investigate the relationship between AGN and stellar mass black

holes further through their jets. Black hole X-ray binaries display two distinct steady states, the so-called 'low/hard' and 'high/soft' states, plus some 'intermediate' states. The radio, and therefore jet, properties are intimately linked to these X-ray states, reflecting a coupling between accretion and outflow. Jets are observed in many AGN of various types. Now that a connection has been established between the Seyferts, the LINERs and possibly even the Galactic Centre which may take the form of an sequence in accretion rate, jets in AGN could be examined in this context. Some work on this has already begun, with a radio imaging survey of low luminosity AGN (Nagar et al., 2002). The main physical difference between the black hole X-ray binaries states is disc size and accretion rate, with softest X-ray spectra in the 'high/soft' state corresponding to optically thin discs extending probably to the innermost stable circular orbit. 'Harder' X-ray spectra seem to correspond to the formation of steady jets and transitions from hard to soft states may cause major ejection events (see e.g. Fender, 2003 for a review). Comparing X-ray binaries and AGN it seems that the same states may apply (e.g. Maccarone, Gallo & Fender, 2003) in which case low luminosity AGN including many of the Seyferts may correspond to the 'low/hard' state, NLS1s to the 'high/soft' state and the brightest quasars to sources in outburst which may be making (repeated) hard $\rightarrow$ soft transitions.

Acknowledgments

First and foremost, I owe my thanks to Liz Puchnarewicz, my supervisor, soft excess AGN expert, IDL guru, and web mistress (!), for giving me the opportunity to do a PhD and believing in me from the very beginning. Liz, you will be missed!

I would like to say a *huge* thank you to Mat Page and Roberto Soria for always making time for discussions, and for contributing to this work. Special thanks go to Aneta Siemiginowska for her support during my visits to CfA, to Encarni Romero-Colmenero for guiding me through my first observing run and to my new boss Ralph Wijers for giving me the chance to continue in even higher energy astrophysics. I would also like to thank Kinwah Wu, Phil Uttley, Alex Blustin, Steven Fuerst, Alice Breeveld, Graziella Branduardi-Raymont, Rob Fender, Tracey Poole, Cynthia James, Silvia Zane and Keith Mason for useful discussions and contributions to this work.

On a more personal note, thanks to my Mum, Dad and Marcus for their tremendous support, encouraging me all the way! Thanks go to all my friends at the lab, especially Tracey and Chris, for making my time at MSSL a very memorable one. And lastly, hartelijk bedankt to Klaas for being absolutely fantastic in those final few months.

This work is based on observations obtained with *XMM-Newton*, an ESA science mission with instruments and contributions directly funded by ESA Member States and the USA (NASA). This thesis makes use of data products from the Two Micron All Sky Survey, which is a joint project of the University of Massachusetts and the Infrared Processing and Analysis Center/California Institute of Technol-

ogy, funded by NASA and the NSF. I thank the staff (particularly F. van Wyck) at the South African Astronomical Observatory for assistance with observing in Sutherland. XSPEC is distributed and maintained under the aegis of the GSFC HEASARC. IRAF is distributed by the National Optical Astronomy Observatories, which are operated by AURA, Inc., under cooperative agreement with the National Science Foundation. I acknowledge the data analysis facility DIPSO provided by the Starlink Project which is run by CCLRC on behalf of PPARC. I have used the Interactive Data Language programming language developed by Research Systems Incorporated (RSI Inc., Boulder Colorado). This research has also made use of the NASA/IPAC Extragalactic Database which is operated by the Jet Propulsion Laboratory, California Institute of Technology, under contract with the NASA.
This Ph.D. thesis was financially supported by a PPARC studentship.

Bibliography

Antonucci R., 1993, Ann. Rev. Astro. Astrophys., 31 , 473

Armitage P.J., 1998, ApJ, 501, L189

Aschenbach B., Citterio O., Ellwood J., 1987, 'The High-Throughput Spectroscopic Mission, Report of the Telescope Working Group', ESA SP-1084

Baganoff F.K. et al., 2003, ApJ, 591, 891

Bahcall J.N., Kirhakos S., Saxe, D.H., Schneider, D.P., 1997, ApJ, 479, 642

Balbus S.A., Hawley J.F., 1991, ApJ, 376, 214

Balbus S.A., Hawley J.F., 1998, *Revs. Mod. Phys.*, 70, 1

Balbus S., Papaloizou J., 1999, ApJ, 521, 650

Baldwin J.A., Phillips M.M., Terlevich R., 1981, PASP, 93, 5

Behar E., Sako M., Kahn S.M., 2001, ApJ, 563, 497

Belloni T., Méndez M., King A.R., van der Klis M., van Paradijs J., 1997, ApJ 488, L109

Berriman G., Schmidt G.D., West S.C., Stockman H.S., 1990, ApJS, 74, 869

Bianchi S., Matt G., Balestra I., Perola G.C., 2003, A&A, 407, L21

Biretta J.A., Stern C.P., Harris D.E., 1991, AJ, 101, 1632

Blustin A.J., Branduardi-Raymont G., Behar E., Kaastra J.S., Kriss G.A., Page M.J., Kahn S.M., Sako M.,Steenbrugge K.C., 2003, A&A, 403, 481

Boller Th., Brandt W.N., Fink H., 1996, A&A, 305, 53

Boller Th., Fabian A.C., Sunyaev R., Trümper J., Vaughan S., Ballantyne D.R., Brandt W.N., Keil R., Iwasawa K., 2002, MNRAS, 329, L1

Borozdin K., Revnivtsev M., Trudolyubov S., Shrader C., Titarchuk L., 1999, ApJ, 517, 367

Brandt W.N., Fabian A.C., Nandra K., Reynolds C.S., Brinkmann W., 1994, MNRAS, 271, 958

Brandt W.N., Mathur S., Elvis M., 1997, MNRAS, 285, L25

Brandenburg A., Nordlund Å., Stein R.F., Torkelsson U., 1995, ApJ, 446, 874

Breeveld A.A., Puchnarewicz E.M., Otani C., 2001, MNRAS, 325, 772

Bregman J.N., 1990, A&ARev., 2, 125

Burderi, L., King, A., Szuszkiewicz, E., 1998, ApJ, 509, 85

Carter B.S., 1990, MNRAS, 242, 1

Coupé S., Godet O., Dumont A.-M., Collin S., 2004, A&A414, 979

Czerny B., Elvis M., 1987, ApJ, 321, 305

den Herder J.W. et al., 2001, A&A, 365, L7

Dickey J.M., Lockman F.J., 1990, ARA&A, 28, 215

Dopita M.A., Sutherland R.S., 1996, ApJS, 102, 161

Dubus G., Hameury J.-M., Lasota J.-P., 2001, A&A373, 251

Ehle M. et al., 2003, *XMM-Newton* Users' Handbook Issue 2.1

Elvis M., Wilkes B.J., McDowell J.C., Green R.F., Bechtold J., Willner S.P., Oey M.S., Polomski E., Cutri R., 1994, ApJS, 95, 1

Esin A.A., McClintock J.E., Narayan R., 1997, ApJ, 489, 865

Esin A.A., Narayan R., Cui W., Grove E.J., Zhang S-N., 1998, ApJ, 505, 854

Falcke H., Biermann P.L., 1999, A&A, 342, 49

Fender R., 2003, 'Compact Stellar X-Ray Sources', Eds. W.H.G. Lewin and M. van der Klis, Cambridge University Press, in press, astro-ph/0303339

Ferland G.J., Netzer H., 1983, ApJ, 264, 105

Ferland G.J., Korista K.T., Verner D.A., Ferguson J.W., Kingdon J.B., Verner E.M., 1998, PASP, 110, 761

Filippenko A.V., Halpern J.P., 1984, ApJ, 285, 458

Frank J., King A., Raine D., 1992, 'Accretion Power in Astrophysics', Cambridge University Press

George I.M., Fabian A.C., 1991, MNRAS, 249, 352

George I.M., Turner T.J., Netzer H., Nandra K., Mushotzky R.F., Yaqoob T., 1998, ApJS, 114, 73

Giveon U., Maoz D., Kaspi S., Netzer H., Smith P., 1999, MNRAS, 306, 637

Gondoin, P., 2000, *XMM-Newton* Science Analysis System Users' Guide V1.0

Grupe D., Beuermann K., Thomas H.-C., Mannheim K., Fink H.H., 1998, A&A, 330, 25

Grupe D., Beuermann K., Mannheim K., Thomas H.-C., 1999, A&A, 350, 805

Guainazzi M. et al., 1998, A&A, 339, 327

Haardt F., Maraschi L., 1993, ApJ, 413, 507

Halpern J.P., Filippenko A.V., 1984, ApJ, 285, 475

Halpern J.P., Marshall H.L., 1996, ApJ, 464, 760

Halpern J.P., Steiner J.E., 1983, ApJ, 269, L37

Hatziminaoglou E., Siemiginowska A., Elvis M., 2001, ApJ, 547, 90

Hawley J.F., Balbus S.A., 1995, PASA 12, 159

Hawley J.F., Gammie C.F., Balbus S.A., 1995, ApJ, 440,742

Heckman T.M., 1980, A&A, 87, 152

Ho L.C., Filippenko A.V., Sargent W.L.W., 1997, ApJ, 487, 568

Ho L.C., Filippenko A.V., Sargent W.L.W., 2003, ApJ, 583, 159

Ho L.C., 1999, ApJ, 516, 672

Ho L.C. et al., 2001, ApJ, 549, L51

Jansen F. et al., 2001, A&A, 365, L1

Kaspi S., Smith P.S., Netzer H., Maoz D., Jannuzi B.T., Giveon U., 2000, ApJ, 533, 631

Kaspi S. et al., 2002, ApJ, 554, 216

Kellermann K.I., Sramek R., Schmidt M., Shaffer D.B., Green R., 1989, ApJ, 98, 1195

Kinkhabwala, A. et al., 2002, ApJ, 575, 732

Kirsch M., 2003, XMM-SOC-CAL-TN-0018

Komossa S., Breitschwerdt D., 2000, A&SS, 272, 299

Kurpiewski A., Kuraszkiewicz J., Czerny B., 1997, MNRAS, 285, 725

Lampton, M., Margon, B., Bowyer, S., 1976, ApJ, 208, 177

Laor A., Fiore F., Elvis M., Wilkes B.J., McDowell J.C., 1997, ApJ, 477, 93

Laor A., Netzer H., 1989, MNRAS, 238, 897

Leighly K.M., Mushotzky R.F., Yaqoob T., Kunieda H., Edelson R., 1996, ApJ, 469, 147

Lightman A.P, Eardley D.M., 1974, ApJ, 187, L1

Maccarone T.J., Gallo E., Fender R., 2003, MNRAS 345, L19

Magdziarz P., Zdziarski A.A., 1995, MNRAS, 273, 837

Malkan M.A., Sargent W.L.W., 1982, ApJ, 254, 22

Marshall F.E., Boldt E.A., Holt S.S., Mushotzky R.F., Pravdo S.H., Rothschild R.E., Serlemitsos P.J., 1978, BAAS 10, 433

Mason K.O. et al., 1995, MNRAS, 274, 1194

Mason K.O. et al., 2001, A&A, 365, L36

Matsumoto R., Shibata K., 1997, in 'Accretion Phenomena and Related Outflows', Ed. Wickramsinghe D., Ferrario L. & Bicknell G., ASP San Francisco, 766

Matt G., Fabian A.C., Ross R.R., 1993, MNRAS, 262, 179

Menou K., Hameury J.-M., Lasota J.-P., Narayan R., 2000, MNRAS 314, 498

Menou K., Quataert E., 2001, ApJ, 552, 204

Miller J.S., 1989, in 'BL Lac Objects', Ed. Maraschi L., Maccacaro T., Ulrich M.-H., Springer-Verlag Berlin, 395

Mushotzky R.F., 1984, AdSpR, 3, 157

Mushotzky R.F., Done C., Pounds K.A., 1993, ARA&A, 81, 717

Nagar N.M., Falcke H., Wilson A.S., Ulvestad J.S., 2002, A&A, 392, 53

Nandra K., George I.M., Mushotzky R.F., Turner T.J., Yaqoob, T., 1997, ApJ, 488, L91

Narayan R., Barret D., McClintock J.E., 1997, ApJ, 482, 448

Narayan R., Garcia M.R., McClintock J.E., 1997, ApJ, 478, L79

Narayan R., Mahadevan R., Grindlay J.E., Popham R.G., Gammie C., 1998, ApJ, 492, 554

Narayan R., Yi I., 1995, ApJ, 452, 710

Nelson C.H., Whittle M., 1995, ApJS, 99, 67

Neugebauer G., Green R.F., Matthews K., Schmidt M., Soifer B.T., Bennett J., 1987, ApJS, 63, 615

O'Brien P., Gondhalekar P., Wilson R., 1988, MNRAS, 233, 801

Otani C., Kii T., Reynolds C.S., Fabian A.C., Iwasawa K., Hayashida K., Inoue H., Kunieda H., Makino F., Matsuoka M., Tanaka Y., 1996, PASJ, 48, 211

Osterbrock D.E., Pogge R.W., 1985, ApJ, 297, 166

Padovani P., Rafanelli P., 1988, A&A, 205, 53

Page M.J., 2001, MNRAS, 328, 925

Page M.J., Breeveld A.A., Soria R., Wu K., Branduardi-Raymont G., Mason K.O., Starling R.L.C., Zane S., 2003, A&A, 400, 145

Page M.J., Davis, Salvi N.J., 2003, MNRAS, 343, 1241

Page K.L., Pounds K.A., Reeves J.N., O'Brien P.T., 2001, MNRAS, 330, L1

Page M.J., Soria R., Zane S., Wu K., Starling R.L.C., 2004, A&A, submitted

Penston M.V., Cannon R.D., 1970, R. Obs. Bull., 159, 84

Peterson B.M., Wandel A., 2000, ApJ, 540, L13

Phillips M.M., 1979, ApJ, 227, L121

Pica A.J., Smith A.G., Webb. J.R., Leacock R.J., Clements S., Gombola P.P., 1988, AJ, 96, 1215

Porquet D., Dubau J., 2000, A&AS, 143, 495

Pounds K.A., Done C., Osborne J.P., 1995, MNRAS, 277, L5

Pounds K.A., Reeves J.N., Page K.L., O'Brien P.T., 2004, ApJ 605, 670

Pounds K.A., Reeves J.N., Page K.L., Edelson R., Matt G., Perola G.C., 2003, MNRAS, 341, 953

Pounds K.A. et al., 1993, MNRAS, 260, 77

Pounds K.A., Nandra K., Fink H.H., Makino F., 1994, MNRAS, 267, 193

Puchnarewicz E.M., Mason K.O., Cordova F.A., Kartje J., Branduardi-Raymont G., Mittaz J.P.D., Murdin P.G., Allington-Smith J., 1992, MNRAS, 256, 589

Puchnarewicz E.M., Branduardi-Raymont G., Mason K.O., Sekiguchi K., 1995, MNRAS, 276, 1281

Puchnarewicz E.M., Mason K.O., Romero-Colmenero E., Carrera F.J., Hasinger G., McMahon R., Mittaz J.P.D., Page M.J., Carballo R., 1996, MNRAS, 281, 1243

Quataert E., di Matteo T., Narayan R., Ho L.C., 1999, ApJ, 525, L89

Quataert E., Narayan R., Reis M.J., 1999, ApJ, 517, L101

Reynolds C.S., Fabian A.C., Nandra K., Inoue H., Kunieda H., Iwasawa K, 1995, MNRAS, 277, 901

Risaliti, G., Gilli, R., Maiolino, R., Salvati, M., 2000, A&A, 357, 13

Ross R.R., Fabian A.C., Ballantyne D.R., 2002, MNRAS, 336, 315

Ross R.R., Fabian A.C., Mineshige S., 1992, MNRAS, 258, 189

Sadler E.M., 1984, AJ, 89, 53

Sako M., Kahn S.M., Paerels F., Liedahl D.A., 2000, ApJ, 543, L115

Sako M. et al., 2001, A&A, 365, L168

Schlegel D.J., Finkbeiner D.P., Davis M., 1988, ApJ, 500, 525

Schmidt M., Green R., 1983, ApJ, 269, 352

Seaton M.J. et al., 1979, MNRAS, 187, 73

Seyfert C.K., 1943, ApJ, 97, 28

Shakura N., Sunyaev R., 1973, A&A, 24, 337

Shields J.C., Rix H.-W., McIntosh D.H., Ho L.C., Rudnick G., Filippenko A.V., Sargent W.L.W., Sarzi M., 2000, ApJ, 534, L27

Siebert, J., Komossa, S. and Brinkmann, W., 1999, A&A, 351, 893

Siemiginowska A., Czerny B., 1989, MNRAS, 239, 289

Siemiginowska A., Czerny B., Kostyunin V., 1996, ApJ, 458, 491

Siemiginowska A., Elvis M., 1997, ApJ, 482, L9

Soria R., Puchnarewicz E.M., 2002, MNRAS, 329, 456

Spergel D.N. et al., 2003, ApJS, 148, 175

Stark A.A., Bally J., Knapp G.R., Krahnert A.C., Penzias A.A., Wilson R.W., 1985, BAAS, 17, 613

Starling R.L.C., Page M.J., Branduardi-Raymont G., Breeveld A.A., Soria R., Wu K., 2004, MNRAS, submitted

Starling R.L.C., Puchnarewicz E.M., Romero-Colmenero E., Mason K.O., 2002, '34th COSPAR Scientific Assembly, The Second World Space Congress, held 10-19 October, 2002 in Houston, TX, USA', 1944

Starling R.L.C., Siemiginowska A., Uttley P., Soria R., 2004, MNRAS, 347, 67

Strittmatter P.A., Serkowski K., Carswell R., Stein W.A., Merrill K.M., Burbidge E.M., 1972, ApJ, 175, L7

Strüder L. et al., 2001, A&A, 365, L18

Tanaka Y., Koyama K., Maeda Y., Sonobe T., 2000, PASJ, 52, L25

Terashima Y., Iyomoto N., Ho L.C., Ptak A.F., 2002, ApJS, 139, 1

Timmer J., König M., 1995, A&A, 300, 707

Titarchuk L., 1994, ApJ, 434, 313

Turner M.J.L. et al., 2001, A&A, 365, L18

Turner T.J., Pounds K.A., 1989, MNRAS, 240, 833

Turner T.J. et al., 1999, ApJ, 510, 178

Uttley P. Edelson R., M^{c}Hardy I.M., Peterson B.M., Markowitz A., 2003, ApJ, 584, L53

Uttley P., M^{c}Hardy I.M., Papadakis I.E., 2002, MNRAS, 332, 231

Walter R., Fink H.H., 1993, A&A, 274, 105

Wandel A., 1997, ApJ, 490, L131

Wandel A., 1999, ApJ, 527, 657

Wandel A., Boller Th., 1998, A&A, 331, 884

Wang T., Otani C., Cappi M., Leighly K.M., Brinkmann W., Matsuoka M., 1998, MNRAS, 293, 397

Wang T., Lu Y., 2001, A&A, 377, 52

Webb W., Malkan M., 2000, ApJ, 540, 652

Weedman D.W., 1998, 'Quasar astronomy', Cambridge Astrophysics Series, Cambridge University Press

Wilms J., Reynolds C.S., Begelman M.C., Reeves J., Molendi S., Staubert R., Kendziorra E., 2001, MNRAS, 328, L27

Winkler H., 1997, MNRAS, 292, 273

Woo J.-H., Urry M.C., 2002, ApJ, 579, 530

Wu C.-C., Boggess A., Gull T.R., 1983, ApJ, 266, 28

Appendix: acronyms

ADAF	advection dominated accretion flow
AGN	Active Galactic Nuclei
ASCA	Advanced Satellite for Cosmology and Astrophysics
BB	blackbody
BBB	big blue bump
BLR	broad-line region
BLRG	broad-line radio galaxy
CCD	charge-coupled device
CfA	Center for Astrophysics
CV	cataclysmic variable
dof	degrees of freedom
EPIC	European Photon Imaging Camera
EUV	extreme ultraviolet
FWHM	full width at half maximum
GBH(C)	Galactic black hole (candidate)
GIS	Gas Imaging Spectrometer
GTP	guaranteed time programme
HEAO	High Energy Astrophysical Observatory
HR	hardness ratio
HST	Hubble Space Telescope
IR	infrared
IRAF	Image Reduction and Analysis Facility
IRAS	Infrared Astronomical Satellite
IUE	International Ultraviolet Explorer
LINER	low ionisation nuclear emission-line region
LWR	Long Wavelength Redundant
MOS	metal oxide semiconductor
MHD	magnetohydrodynamic
MSSL	Mullard Space Science Laboratory

NASA	National Aeronautics and Space Administration
NED	NASA/IPAC Extragalactic Database
NLR	narrow-line region
NLRG	narrow-line radio galaxy
NLS1	narrow-line Seyfert 1
OM	Optical Monitor
OVV	optically violent variable
PDS	Phoswich Detector System
PG	Palomar-Green
PL	power law
PSPC	Position Sensitive Proportional Counter
QE	quantum efficiency
QPO	quasi-periodic oscillation
QSO	quasi-stellar object
RGS	Reflection Grating Spectrometer
RQ	radio-quiet
RL	radio-loud
SAAO	South African Astronomical Observatory
SAS	Science Analysis System
SED	spectral energy distribution
SIS	Solid-state Imaging Spectrometer
SWP	Short Wavelength Prime
UCL	University College London
UK	United Kingdom
UTA	unresolved transition array
UV	ultraviolet
WFC	Wide Field Camera
WMAP	Wilkinson Microwave Anisotropy Probe
XMM	X-ray Multi-mirror Mission